Impact on
Sand and Water

The research described in this thesis is part of the research program of the “Stichting voor Fundamenteel Onderzoek der Materie” (FOM), which is financially supported by the “Nederlandse Organisatie voor Wetenschappelijk Onderzoek” (NWO). It was carried out at the Physics of Fluids research group of the faculty of Science and Technology of the University of Twente.

Nederlandse titel:
Inslag op Zand en Water.

Publisher:
Raymond Bergmann, Physics of Fluids, University of Twente,
P.O Box 217, 7500 AE Enschede, The Netherlands
http://pof.tnw.utwente.nl/

Cover design: Raymond Bergmann
Cover illustrations: controlled water impact see Chapter 6,
sand impact see Chapter 2.
Print: Gildeprint B.V., Enschede

ISBN 978-90-365-2478-0

IMPACT ON SAND AND WATER

PROEFSCHRIFT

ter verkrijging van
de graad van doctor aan de Universiteit Twente,
op gezag van de rector magnificus,
prof. dr. W. H. M. Zijm,
volgens besluit van het College voor Promoties
in het openbaar te verdedigen
op donderdag 15 maart 2007 om 15.00 uur

door

Raymundus Petrus Henricus Maria Bergmann
(Raymond)

geboren op 15 januari 1979

te Amsterdam

Dit proefschrift is goedgekeurd door de promotor:
prof. dr. rer. nat. D. Lohse

en de assistent-promotor:
dr. D. van der Meer

Contents

Chapter 1

Introduction

1.1 Jets

1.1.1 Jets in nature and industry

Scientific interest in free surface jets started at the beginning of the twentieth century when A.M. Worthington published his famous work “A study of splashes” [1]. His photographs of fluid impacts (see Fig. 1.1) revealed a wealth of phenomena of unanticipated complexity that continue to pose intriguing questions to today. In this thesis we will aim to answer some of these questions.

The impact and jetting phenomena observed by Worthington are ubiquitous in nature: One of the most familiar examples for us living in the wet Northern European climate are raindrops falling into a puddle on a rainy day. If examined closely (Fig. 1.2), a jet can be seen to erupt just after a raindrop has impacted the surface of the puddle. Just before the eruption of the jet a small bubble is enclosed [3], and as a matter of fact it is not the impact of the drop itself, but the oscillations of this small bubble that produces the sound so characteristic for rain. On large scale it is the raindrops falling on the world oceans, that by the same process entrain vast quantities of air and turn our seas into a major sink for carbon dioxide from the atmosphere. On even larger scale, the planetary impact of a large meteorite is governed by the same mechanisms and principles that govern the impact of a simple drop of rain.
Many more examples of impact and jetting phenomena can be found in Nature, but also in technical applications jetting has gained much impact leading to many, nowadays standard, applications. Think only of inkjet printers, in which droplets of ink are produced at high frequencies in

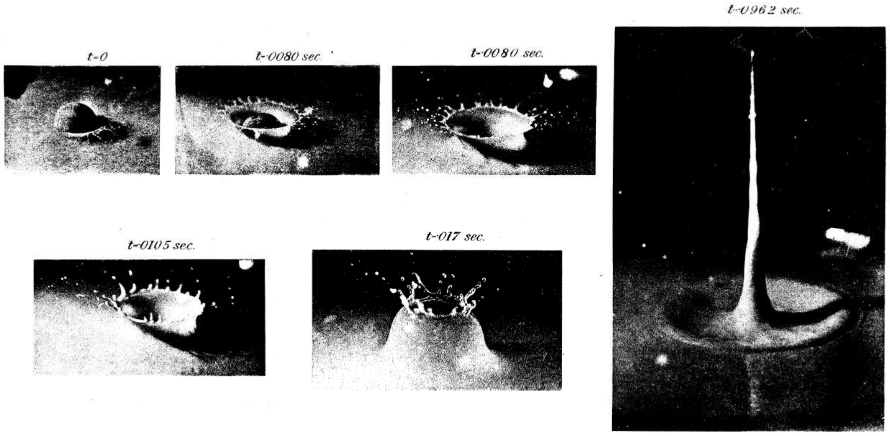

Figure 1.1: Photographs made by A.M. Worthington *et al* [2] in 1897 of the impact of a metal sphere into milk.

an extremely reproducible manner by a jetting procedure (see Fig. 1.3). And then in a more industrial setting, there are the strong jets used for water jet cutting. Droplet impact and the subsequent void collapse are also a major source of noisy underwater sound [3] and a thorough understanding is therefore crucial in sonar applications, which rely on the precise recording of echoes and are greatly hampered by other sources of sound. High speed water impacts and underwater cavity formation are moreover of obvious relevance to military operations [4], where one has to think of missiles and torpedoes entering the sea. In the context of industrial applications, the detailed understanding of drop impact and void formation is essential in pyrometallurgy [5, 6] and for the food industry.

In the near future it could even be small jets which intravenously inject drugs into single cells. When a bubble collapses near a solid boundary, a strong jet can be observed directed towards the boundary. As with all jets, the focussing of momentum in the jet is tremendous, making it capable of puncturing the membrane of a cell. If bubbles are introduced into the bloodstream, they can be made to collapse by an externally applied sound field. If a drug would be simultaneous introduced, the bubbles which collapse close to a cell, will puncture the cells membrane with a jet containing the drug. As the sound field can be focussed, such a method would be localized and very useful in cancer treatments.

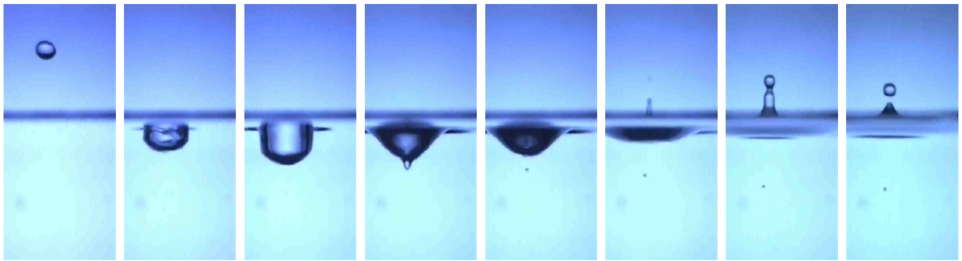

Figure 1.2: The impact of a 6 mm droplet of water on a water surface. Courtesy of S.M. van der Meer and T.H. van den Berg.

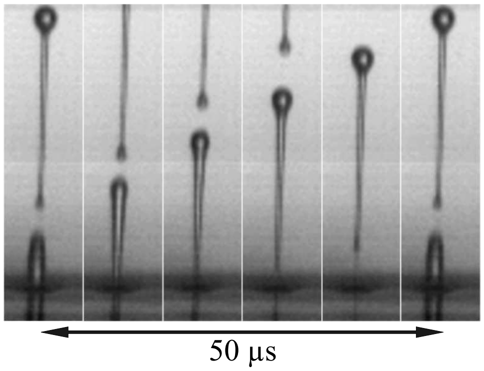

Figure 1.3: The jetting of ink droplets at high frequencies in an extremely reproducible manner by an ink jet printer. Courtesy of J. de Jong.

1.1.2 The mechanism of jet formation

All the aforementioned jets in nature and industry emerge when a relatively large amount of kinetic energy is imparted onto a small mass of liquid near a free surface. The mechanisms which focus energy onto the small mass of liquid occur in great variety. For instance in the case of the jet produced by the printhead of an inkjet printer, a pressure wave in an open-ended channel is focussed on the free surface at the nozzle. This mechanism creates a jet which eventually pinches off [7–9] (cf. Figs. 1.3).

A different driving and focusing mechanism causes jetting in a glass of champagne. Here, jetting occurs when carbon dioxide bubbles from the bulk reach the surface and "pop". When such a bubble of gas reaches the free surface, the liquid film on top of the bubble drains until it ruptures and quickly retracts. This leaves an unstable cavity at the surface in which the surface tension stresses focus on the base. These stresses are released in the eruption of a liquid jet. Thus in the case of a glass of champagne, the shape of the free surface provides the focussing for the jetting driven by surface tension [10, 11]. Many more jet producing mechanisms are known, like the jets produced by armor piercing weapons [12], for which the focussing is purely geometrical and the driving is provided by an explosive chemical reaction, or the jetting of bubbles collapsing near a boundary [13] with the possible medical application mentioned before and which are due to the asymmetry in the pressure driven collapse of the bubble.

On larger scales, where the influence of surface tension can be neglected, a typical example of momentum focusing is the previously discussed raindrop jet (Fig. 1.2). The impact of a droplet or object onto a fluid surface causes a cavity to form, but in contrast to the champagne bubble, surface tension is now irrelevant and the cavity collapses purely under the influence of hydrostatic pressure. As the sides of the cavity collapse and eventually collide upon each other, the moving fluid is released up and down forming two vertical jets [1, 14–16]. Surprisingly, a similar void collapse can even be observed in aerated sand [17], when a steel ball impacts a bed of sand. After the "hydrostatic" void collapse a jet of sand shoots up- and downward [17, 18].

It is this type of jet formation processes that will be studied in this thesis. The jet formation after the impact of an object on water or sand is one of the most spectacular examples of "free surface" flow and unravelling the underlying mechanisms will shed light on all aforementioned jetting phenomena, albeit in industry or nature.

1.2 Impact on water and sand

There are some apparent difficulties with the study of the impact of an object on a free surface and the subsequent jetting. To name the most challenging ones: (i) The impact event has a very short duration ($\approx$ 100 ms). (ii) Throwing an object into a fluid is in general quite an errorprone experiment: all but one of the systems parameters (the Froude number) are response parameters and (iii) one has to take special precautions to warrant reproducible results, especially for the impact experiments in sand. We dealt with those problems in the following way.

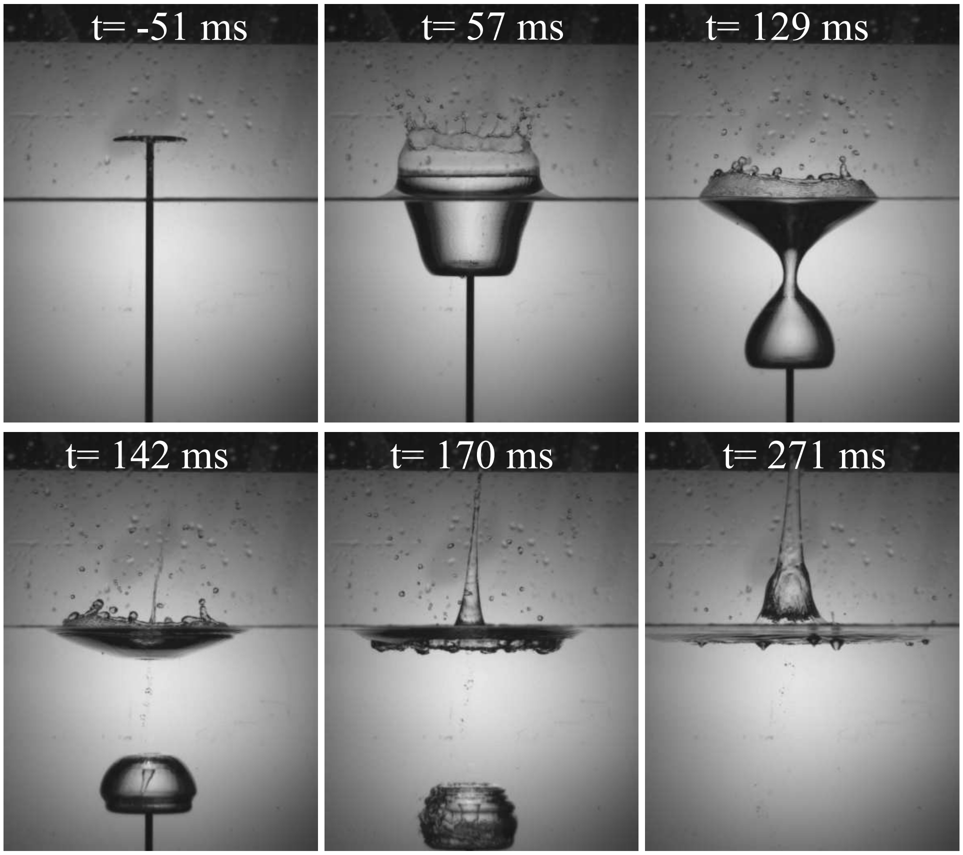

Figure 1.4: The controlled impact of a disk with a diameter of 60 mm onto the water surface with a constant velocity of 1 m/s.

The short duration of the event is what made the initial study by Worthington [1] a true technological feat. A typical experiment on the scale performed by Worthington lasted less then 0.5 seconds, therefore Worthington had to piece together the series of events by single photographs of repeated fluid impacts. However, the advent of the high speed camera has made it possible to make a continuous record of one impact event. This experimental tool is readily used throughout the thesis to study the impact in detail and make a more quantitative comparison with proposed theoretical descriptions and numerical experiments. In this work we make use of cameras operating from a 1000 frames per second up to 50000 frames per second.

The difficulties with the reproducibility and controllability of the impact experiment is different for water impact and for sand. In the case of the impact of a solid body on a water surface, one has to deal not only with the body acting on the water, but also with the fluid acting on the body itself. Due to this interaction, the path of the object is thus dependent on shape, orientation, weight and impact velocity of the object. These dependencies of the path make a systematic study of the cavity dynamics hard, as the cavity is directly influenced by the changing path. To circumvent this problem, an experimental setup will be presented in which one has *full control* over the impacting object by attaching it to an external motor. In this way, the response velocity of the impacting body inside the liquid is effectively eliminated, as it now becomes a control parameter of the system. As an example, Fig. 1.4 shows a high speed recording of the controlled impact of a disk at constant velocity.

For impacts on sand, it is not so much the controllability of the path of the impacting body which makes the experiments hard to interpret, but rather the poorly defined initial state of the granular material. It is therefore hard to achieve quantitatively reproducible results, presumably due to the random nature of the force-chain-networks in the granular material [19–21]. In order to prepare a well-defined initial state for our experiments, we decompactify and homogenize the fine sand by blowing air through it via a perforated bottom plate. The air is slowly turned off before the experiments and the grains are left to settle in an extremely loose packing (41% volume fraction) with the force-chains either broken or substantially weakened. With this procedure the reproducibility of our sand experiments is greatly improved.

The second challenge presented by impact experiments on sand is the difficulty to look into the sand during the experiment. There are some cutting edge technologies available today, but they all have significant disadvantages for the experiments at hand: They are either much too slow (MRI or X–ray tomography [22–24]), lack accuracy (imaging using radiation from β^+-d-decay [25]), or ask for a significant reduction of the size of the experiment (high speed X–ray imaging [26]). The approach taken in this thesis is to observe the events above the sand (e.g., the trajectory of the object inside the sand could be measured by imaging a tail which was attached to the object) and relate these direct observations to the mechanism of cavity collapse within the sand. This connection is made by comparing them to the events and theoretical descriptions for a cavity collapse in water and molecular dynamics simulations.

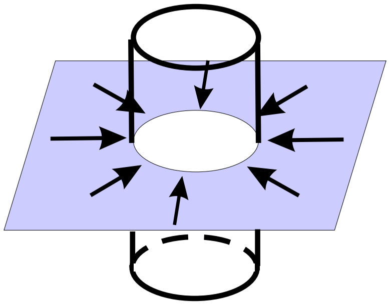

Figure 1.5: Schematic representation of the model for the cavity collapse. The flow surrounding the cavity (black arrows) is taken to be purely radial, it is confined to the horizontal plane (blue plane).

1.3 Model of cavity collapse

The full analytical modelling of a cylindrical symmetric collapse of the transient cavity presents the difficulty of a coupling between the free surface and the flow surrounding the cavity. To tackle this difficulty we propose the useful simplification of dividing the problem up into a set of quasi two–dimensional problems as sketched in Fig. 1.5. If the axial component of the flow is small compared to the horizontal flow components, we can take the flow to be confined to the horizontal plane. In this way an equation for the collapse of a two–dimensional bubble will suffice to describe the cavity dynamics at an arbitrary depth.

To derive such an equation we will closely follow a derivation given in [27] and [28]. The argument starts by writing the Euler equation in cylindrical coordinates. This means that we assume the flow to be quasi two dimensional at any depth along the cavity (cf. Fig. 1.5). The azimuthal components can be ignored due to radial symmetry, leaving us with the following equation,

$$\frac{\partial v_r}{\partial t} + v_r \frac{\partial v_r}{\partial r} = -\frac{1}{\rho}\frac{\partial p}{\partial r}\,, \tag{1.1}$$

where ρ denotes the density of the liquid. Here, the radial velocity component v_r and the pressure p are assumed to be a function of the radial coordinate r only. The continuity equation and the boundary conditions on the surface of the void lead to a second equation

$$r v_r(r,t) = h(t)\dot{h}(t)\,, \tag{1.2}$$

Here, $h(t)$ is the radius of the cavity and derivative $\dot{h}(t)$ the velocity of the cavity wall. Substituting Eq. (1.2) into Eq. (1.1) gives,

$$\frac{\partial}{\partial t}\left(\frac{h\dot{h}}{r}\right)+\frac{\partial}{\partial r}\left(\frac{1}{2}v_r^2+\frac{p}{\rho}\right)=0. \tag{1.3}$$

We can integrate this equation over r from the cavity wall h to a reference point h_∞, where the flow is taken to be quiescent. h_∞ is expected to be of the order of a typical length scale of the system, such as the depth of the cavity. Thus, strictly speaking, h_∞ is a function of time and of the impact parameters. We ignore this dependence here. Then the integration yields a Rayleigh-like equation for the void radius at a fixed depth z,

$$\left[\frac{d(h\dot{h})}{dt}\right]\log\frac{h}{h_\infty}+\frac{1}{2}\dot{h}^2=-gz\,. \tag{1.4}$$

Here, we have used the fact that the pressure driving the collapse of the cavity is provided by the hydrostatic pressure $p=-\rho gz$, where z denotes the depth below the fluid surface. Thus, in Eq. (1.4) it is assumed that the system is composed of non-interacting horizontal layers of fluid, with a negligible vertical velocity component.

1.4 Guide through the chapters

The prime objective of this thesis is to study the dynamics of the "free surface" for sand and fluids after the impact of a solid body. In both cases, it is the hydrostatically driven collapse of the free surface which gives rise to the focussing of the flow and the subsequent singularity from which the upwards jet and downwards jet erupt.

In Chapter 2, we show that the impact of a steel ball on very loose and fine sand bears a striking resemblance to the impact of an object on a liquid. To investigate the mechanism of jet creation in the sand, we employ molecular dynamics simulations, quasi two dimensional experiments, and a continuum description based on the Euler equation to describe the void dynamics [17].

The preparation of the sand, to obtain a well defined initial state for the experiments, greatly reduces the yield stress of the sand and puts our experiments in the same spot in parameter space as large meteorite impacts and give them possible relevance in a geophysical context.

This procedure to prepare the sand, weakens the force chains in the sand to such a degree that the sand can no longer support any weight. This extremely low yield stress state of the sand, or ”dry quick sand” as we name it, is discussed in Chapter 3. The dry quick sand is probed by investigating an object penetrating the sand. Surprisingly, the observed phenomena are accurately captured by a simple Coulumb friction model [29].

In Chapter 4 we will address the influence of the ambient air on the experiment. It is found that when the ambient pressure is reduced below a certain threshold, also the height of the sand jet is considerably reduced. We find that surprisingly this reduction is not due to an alteration of the jet formation mechanism, but it is due to the way the sphere penetrates into the sand. The altered path of the ball changes the depth at which the singularity of the hydrostatic collapse (Chapter 4) occurs and a shallower singularity creates a smaller jet [30].

In Chapter 5, we change from sand to water impacts. We impact a disk on a water surface and investigate the final stages of the hydrostatically driven collapse of the free surface. Where pinch-offs of, e.g., liquid drops are known to exhibit universal behavior close to singularity, in our experiment the inertial collapse of the gas filled neck is found to strongly depend on the initial conditions set by the impacting disk [15].

The initial conditions for the collapsing neck are set by the shape of the cavity. This cavity shape is examined in great detail in Chapter 6. Using the same theoretical approach as Chapter 2, many aspects of the free surface dynamics are captured, increasingly so, if the cavity shape becomes more cylindrical. This Chapter 6 concludes our discussion of jets produced by the hydrodynamic collapse of the surface void created by the impact of an object on sand and liquid [31].

We also investigated the cavity collapse after the submerging of a cylinder, which turned out to be remarkably different from the disk impact. For the cylinder capillary effects are found to have a lasting influence on the cavity development and to strongly influence the depth of the cavity closure. This influence of capillary effects is absent for the impact of a disk. This study will however not be presented as part of this thesis, but will be reported separately [32].

In Chapter 7 we will discuss the formation of a jet of a different type, namely when water rushes upwards to fill an initially empty vertical tube partially immersed in a bath of fluid, under specific conditions a jet is seen to perturb from the water surface. In this chapter, we see that this jet also arises from a focussing of the flow, like the jet in water and sand after the impact of an object, however in this case the flow focussing is provided by the geometry of the tube [33].

The work presented in this thesis is a close combination of laboratory experiments, numerical calculations (molecular dynamics simulations for the sand and boundary integral simulations for the fluids), and theoretical analysis. As seen again and again, all three are found to agree very well, shedding their light on the process of jet creation in both water and sand.

References

[1] A.M. Worthington, *A study of splashes* (Longman and Green, London, 1908).

[2] A.M. Worthington and R.S. Cole, *Impact with a liquid surface, studied by the aid of instantaneous photography*, Phil. Trans. R. Soc. Lond. A **189**, 137 (1897).

[3] A. Prosperetti, L.A. Crum, and H.C. Pumphrey, *Underwater noise of rain*, J. Geophys. Res. **94**, 3255 (1989).

[4] M. Lee, R.G. Longoria, and D.E. Wilson, *Cavity dynamics in high-speed water entry*, Phys. Fluids **9**, 540 (1997).

[5] J.-L. Liow, D. Morton, A. Guerra, and N. Gray, in *Howard Worner Inr. Symp. on injection in pyrometallurgy*, edited by M. Nilmani and T. Lehner (Pennsylvania, 1996).

[6] D. Morton, J.-L. Liow, and M. Rudman, *An investigation of the flow regimes resulting from splashing drops*, Phys. Fluids **12**, 747 (2000).

[7] H.P. Le, *Progress and trends in ink-jet printing technology*, J. Imag. Sci. Tech **42**, 49 (1998).

[8] A.U. Chen and O.A. Basaran, *A new method for significantly reducing drop radius without reducing nozzle radius in drop-on-demand drop production*, Phys. Fluids **14**, L1 (2002).

[9] J. de Jong, G. de Bruin, H. Reinten, M. van den Berg, H. Wijshoff, M. Versluis, and D. Lohse, *Air entrapment in piezo-driven inkjet printheads*, J. Acoust. Soc. Am. **120**, 1257 (2006).

[10] J.M. Boulton-Stone and J.R. Blake, *Gas bubbles bursting at a free surface*, J. Fluid Mech. **254**, 437 (1993).

[11] G. Liger-Belair, H. Lemaresquier, B. Robillard, B. Duteurtre, and P. Jeandet, *The secrets of fizz in champagne wines: A phenomenological study*, Am. J. Enology and Viticulture **52**, 88 (2001).

[12] G. Birkhoff, D.P. MacDougall, E.M. Pugh, and G. Taylor, *Explosives with lined cavities*, J. Appl. Phys. **19**, 563 (1948).

[13] C.D. Ohl and R. Ikink, *Shock-wave-induced jetting of micron-size bubbles*, Phys. Rev. Lett. **90**, 2145021 (2003).

[14] B.W. Zeff, B. Kleber, J. Fineberg, and D.P. Lathrop, *Singularity dynamics in curvature collapse and jet eruption on a fluid surface*, Nature **403**, 401 (2000).

[15] R. Bergmann, D. van der Meer, M. Stijnman, M. Sandtke, A. Prosperetti, and D. Lohse, *Giant bubble pinch-off*, Phys. Rev. Lett. **96**, 154505 (2006).

[16] V. Ducleaux, F. Caillé, C. Duez, C. Ybert, L. Bocquet, and C. Clanet, *Dynamics of transient cavities*, submitted to Phys. Fluids (2006).

[17] D. Lohse, R. Bergmann, R. Mikkelsen, C. Zeilstra, D. van der Meer, M. Versluis, K. van der Weele, M. van der Hoef, and H. Kuipers, *Impact on soft sand: Void collapse and jet formation*, Phys. Rev. Lett. **93**, 1980031 (2004).

[18] S.T. Thoroddsen and A.Q. Shen, *Granular jets*, Phys. Fluids **13**, 4 (2001).

[19] C.-h. Liu, S.R. Nagel, D.A. Schecter, S.N. Coppersmith, S. Majumdar, O. Narayan, and T.A. Witten, *Force fluctuations in bead packs*, Science **269**, 513 (1995).

[20] H.M. Jaeger, S.R. Nagel, and R.P. Behringer, *Granular solids, liquids, and gases*, Rev. Mod. Phys. **68**, 1259 (1996).

[21] L.P. Kadanoff, *Built upon sand: Theoretical ideas inspired by granular flows*, Rev. Mod. Phys. **71**, 435 (1999).

[22] M. Nakagawa, S.A. Altobelli, E. Caprihan, A.and Fukushima, and E.-K. Jeong, *Non-invasive measurements of granular flows by magnetic resonance imaging*, Exp. Fluids **16**, 54 (1993).

[23] K.M. Hill, A. Caprihan, and J. Kakalios, *Bulk segregation in rotated granular material measured by magnetic resonance imaging*, Phys. Rev. Lett. **78**, 50 (1997).

[24] D.M. Mueth, G.F. Debregeas, G.S. Karczmar, P.J. Eng, S.R. Nagel, and H.M. Jaeger, *Signatures of granular microstructure in dense shear flows*, Nature **406**, 385 (2000).

[25] R.D. Wildman, J.M. Huntley, and D.J. Parker, *Granular temperature profiles in three-dimensional vibrofluidized granular beds*, Phys. Rev. E **63**, 061311 (2001).

[26] J.R. Royer, E.I. Corwin, A. Flior, M.-L. Cordero, M.L. Rivers, P.J. Eng, and H.M. Jaeger, *Formation of granular jets observed by high-speed x-ray radiography*, Nat. Phys. **1**, 164 (2005).

[27] H.N. Oguz and A. Prosperetti, *Dynamics of bubble growth and detachment from a needle*, J. Fluid Mech. **257**, 111 (1993).

[28] A. Prosperetti, *Bubbles*, Phys. Fluids **16**, 1852 (2004).

[29] D. Lohse, R. Rauhe, R. Bergmann, and D. van der Meer, *Granular physics: Creating a dry variety of quicksand*, Nature **432**, 689 (2004).

[30] G. Caballero, R. Bergmann, D. van der Meer, A. Prosperetti, and D. Lohse, *The role of air in granular jet formation*, submitted to Phys. Rev. Lett. (2006).

[31] R. Bergmann, S. Gekle, A. van der Bos, D. van der Meer, and D. Lohse, *The controlled impact of a disk on a water surface: Cavity dynamics*, to be submitted to J. Fluid Mech. (2006).

[32] S. Gekle, A. van der Bos, R. Bergmann, D. van der Meer, and D. Lohse, *Non-continuous froude number scaling for the closure depth of a cylindrical cavity*, submitted to Phys. Rev. Lett. (2006).

[33] R. Bergmann, S. Gekle, A. van der Bos, D. van der Meer, and D. Lohse, *The tubular jet*, to be submitted to J. Fluid Mech. (2006).

Chapter 2

Impact on soft sand: Void collapse and jet formation [‡]

Very fine sand is prepared in a well defined and fully decompactified state by letting gas bubble through it. After turning off the gas stream, a steel ball is dropped on the sand. The series of events in the experiments and corresponding discrete particle simulations is as follows: On impact of the ball, sand is blown away in all directions ("splash") and an impact crater forms. When this cavity collapses, a granular jet emerges and is driven straight into the air. A second jet goes downwards into the air bubble entrained during the process, thus pushing surface material deep into the ground. The air bubble rises slowly towards the surface, causing a granular eruption. In addition to the experiments and the discrete particle simulations we present a simple continuum theory to account for the void collapse leading to the formation of the upward and downward jets.

2.1 Experiment

According to Shoemaker, the "impact of solid bodies is the most fundamental process that has taken place on the terrestrial planets" [1], as they shape the surfaces of all solar system bodies. A lot of information

---

[‡] Published as: Detlef Lohse, Raymond Bergmann, Rene Mikkelsen, Christiaan Zeilstra, Devaraj van der Meer, Michel Versluis, Ko van der Weele, Martin van der Hoef, and Hans Kuipers, *Impact on soft sand: Void collapse and jet formation*, Phys. Rev. Lett. **93**, 198003 (2004).
The experiments and void collapse analysis described in this chapter are to be considered part of this thesis. The particle simulations were performed by Christiaan Zeilstra.

on this process has been extracted from remote observations of impact craters on planetary surfaces. However, the nature of the geophysical impact events is that they are non-reproducible. Moreover, their scale is enormous and direct observations are not possible. On the other hand, S. Thoroddsen and A. Shen did small scale experiments by letting a lead sphere fall on monodisperse spherical glass beads [2]. They found a jet emerging from the impact site. Similar jets are long known when a ball or a fluid droplet impacts on a liquid surface [3–7]. We did similar experiments as in [2], but now on extremely fine sand (average grain-size of about 40 μm; grains are non-spherical) [8]. We found it hard to achieve quantitatively reproducible results, presumably due to the random nature of the force-chain-networks in the granular material [9–12]. Therefore, in order to prepare a well-defined initial state, we decompactify and homogenize the fine sand by blowing air through it via a perforated bottom plate. The height of the sand bed above the bottom plate is typically 25-40 cm. The air is slowly turned off before the experiments and the grains are left to settle in an extremely loose packing (41% volume fraction) with the force-chains either broken or substantially weakened. We call this a "fluid-like" state. Impact events on this well-prepared fine sand will be gravity-dominated. We let a steel ball (radius $R_0 = 1.25$ cm) fall from various heights (up to 1.5 m) onto the sand and observe the dynamics of the sand with a digital high-speed camera (up to 2000 frames per second).

The series of *visible* events is as follows (see figure 2.1): First, the ball vanishes in the sand and a crown-like *splash* is created. Inhomogeneities develop in the crown, due to the inelastic particle-particle interaction (figure 2.1, frames 3-5). Then, after a while, a *jet* shoots out of the sand at the position of impact. In all our experiments the jet height exceeds the release height of the ball, see figure 2.4a. While the upper part of the jet is still going upwards, in the lower parts the inelastic particle-particle collisions lead to density inhomogeneities in the jet (figure 2.1, frames 7-8). These inhomogeneities resemble those of the surface tension driven Rayleigh-instability of a water jet, even though there is no surface tension in granular matter. Finally, after about half a second, a *granular eruption* is seen at the position of impact, resembling a volcano (figure 2.1, frames 8-9). The collapsing jet first leaves a *central peak* in the crater[*], but the granular eruption violently erases this peak.

---

[*] Similar peaks are observed in many craters of the terrestrial planets [13, 14].

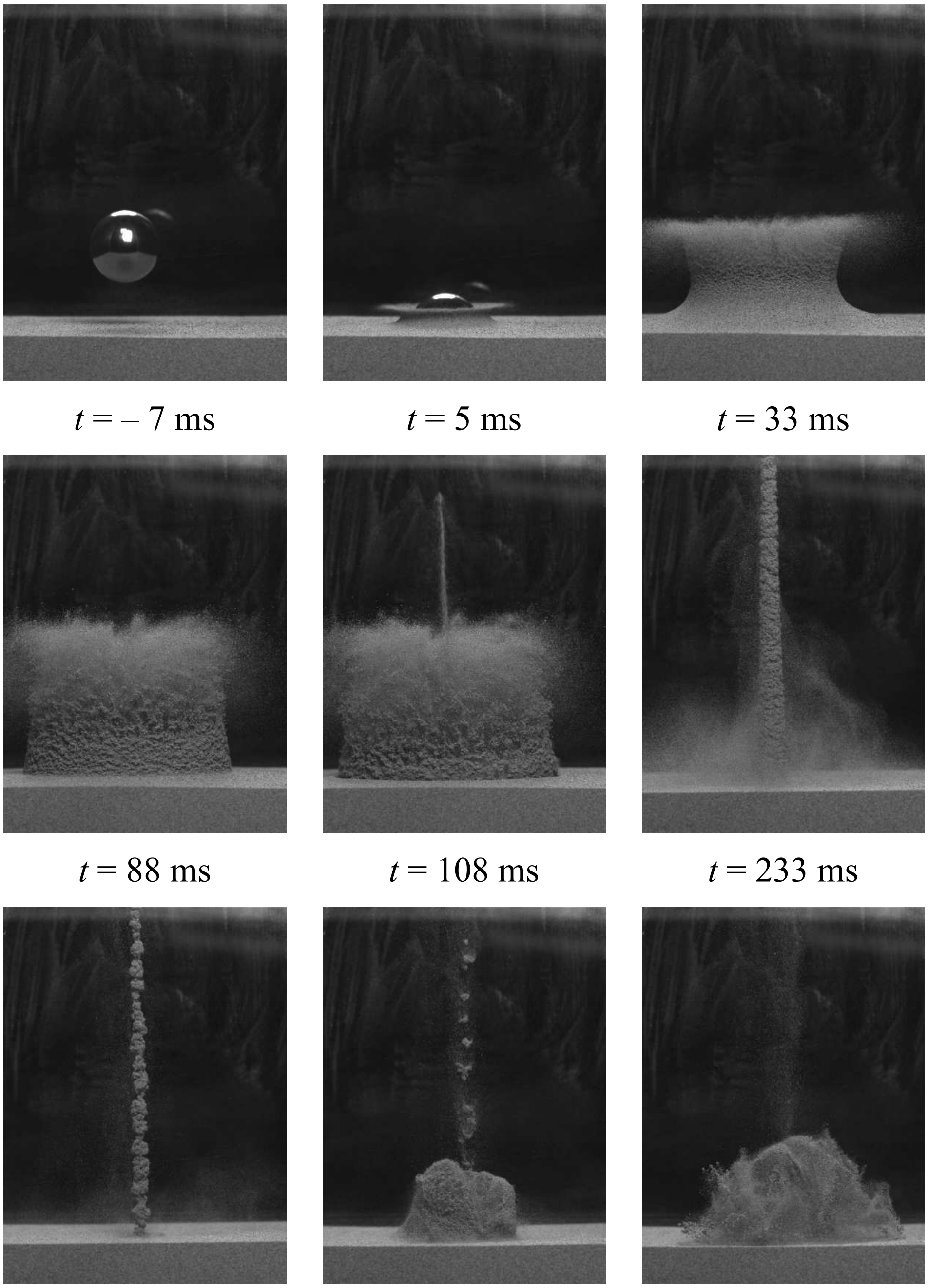

t = – 7 ms
t = 5 ms
t = 33 ms
t = 88 ms
t = 108 ms
t = 233 ms
t = 358 ms
t = 503 ms
t = 583 ms

Figure 2.1: Jet formation after the impact ($v_0 = 2.43$ m/s) of a steel ball of $R_0 = 1.25$ cm on loose very fine sand. The jet in this experiment exceeds the release height of the ball. Frames 2-4: splash; frames 5-6: a jet emerges; frame 7: clustering within the jet; frames 8-9: granular eruption at the surface.

2.2 Void collapse and jet formation

How does the jet form? To find out what is going on *below the surface* of the sand, we (i) performed direct numerical simulations, (ii) redid the experiments in two dimensions, meaning that we replaced the ball by a cylinder (with axis parallel to the surface and orthogonal to the side plates) which we let fall into a bed of sand between two transparent plates, and (iii) employed the analogy to jet formation in fluids [3–7, 15].

(i) In the discrete particle simulations, the sand particles are modeled as spheres which interact via inelastic "soft-sphere" collision rules. The interaction of the particles with the surrounding air is included via empirical drag force relations [16]. Since the maximum number of particles that can be simulated is presently of the order of one million, we can perform only quasi-two-dimensional simulations, where the thickness of the sand bed between the parallel plates is eight grains[†]. Altogether, the calculation includes N= 1.3 million homogeneous beads of density 1000 kg/m^3 and diameter 500 μm (i.e., approximately a factor 10 larger than in experiment) in a container of 24 cm × 0.4 cm ground area and a sand bed height of about 17 cm. The beads are pre-fluidized with air, just as in the experiments, and then a 1.5cm diameter ball of density 3500 kg/m^3 is dropped onto the beads with an impact velocity of 2 m/s. The series of events can be seen in figure 2.2, revealing the jet formation process invisible in figure 2.1: The impacting ball creates a void which is then pressed together through the "hydrostatic" pressure from the side which nonlinearly increases with depth [17]. At small depth the ball passes early, meaning an early start of the void collapse, which however is weak due to the small "hydrostatic" pressure. Conversely, at larger depth the collapse of the void begins later, but is stronger due to the larger "hydrostatic" pressure. Somewhere in the middle the collapse is finished first, and the void walls hit each other. It is this singularity which leads to the formation of *two* jets: One upwards and one downwards into an air bubble which was entrained in the sand by the void collapse. The falling jet often leaves a central peak in the crater (which in our 3D experiments with the fine, decompactified sand is subsequently erased again by the granular eruption). Note that the jet in the discrete particle simulations is much less pronounced than in experiment. First, because the beads in the simulations are much larger than the sand grains in the experiment, i.e. the sand bed is less fluid-like and allows for less fine structure. Second, the singularity due to the focussing along the axis of

---

[†] The 3D simulations we did are too strongly affected by finite size effects. Nevertheless, also for these simulations a jet emerges.

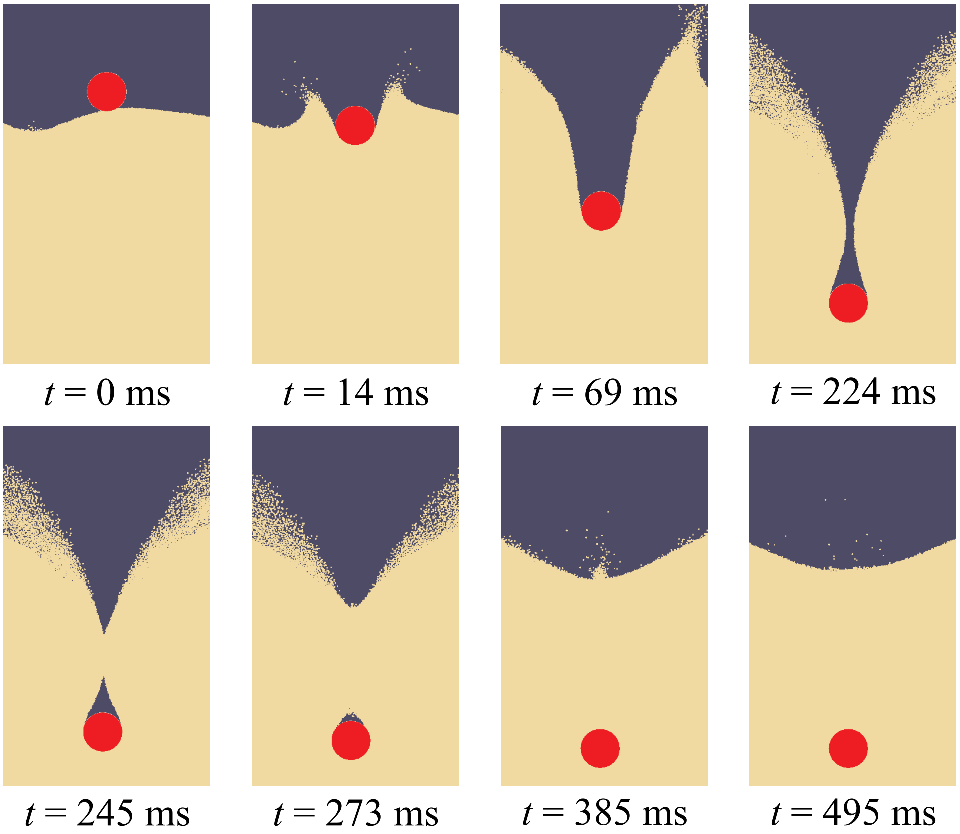
$t = 0$ ms
$t = 14$ ms
$t = 69$ ms
$t = 224$ ms
$t = 245$ ms
$t = 273$ ms
$t = 385$ ms
$t = 495$ ms

Figure 2.2: Cut through the quasi-2D discrete particle simulation. Frames 1-3: the impact of the disk on the particles; Frames 4-6: the collapse of the void; Frame 7: the upward jet (which is less pronounced than in the 3D experiments).

symmetry is weaker in 2D and quasi-2D experiments or simulations than in 3D, and the jet takes the form of a sheet. – We will present a quantitative comparison of experimental and numerical impact events on 500 μm beads elsewhere.

(ii) We performed such 2D jet formation experiments, by letting a cylinder fall into decompactified sand between two transparent plates, and observing the jet formation process from the side [8]. These experiments confirm the above sketched series of events. Again, the jet is less pronounced than in the 3D experiments. The entrained air bubble slowly rises in these

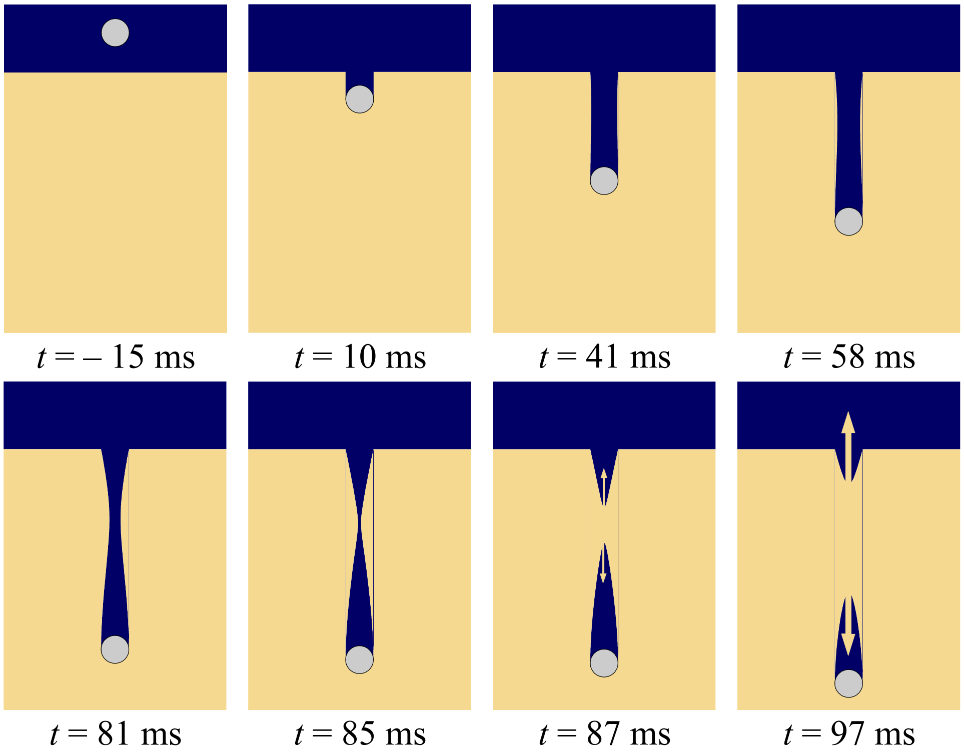

Figure 2.3: Cross-section of the 3D-void collapse following from our Rayleigh-type model, for the same impact velocity and ball radius as in figure 1. The void is pressed together by the "hydrostatic" pressure from the side, leading to a singularity and an upward and downward jet.

experiments, finally leading to a granular eruption at the surface, just as observed in 3D.

(iii) The same series of events is also found after an analogous impact of a steel ball or a falling disk on water [3–7, 15, 18]. We will employ this analogy in order to set up a "minimal" continuum mechanical model, in order to work out the essentials of the void collapse.

First, the delay curve $z(t)$ of the ball in the sand can be obtained from a simple force balance model involving drag, gravity, and added mass. It describes the experimental results obtained for a falling ball equipped with a thin stiff tail, which allows for easy depth measurements [19]. The delay curve $z(t)$ of the ball is inverted to obtain $t_{pass}(z)$, the time when the ball

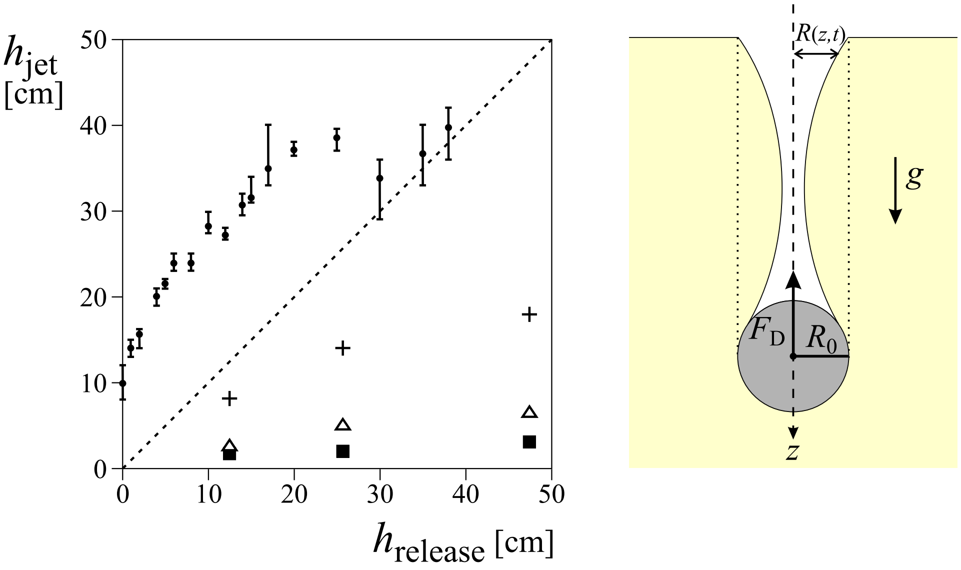

Figure 2.4: (a) Jet height as a function of release height of the ball in our experiments (solid bullets with error bars) and in those of ref. [2] (for spheres in a granulat of different diameter: $d_s = 0.08$ mm (pluses), $d_s = 0.118$ mm (triangles), $d_s = 0.176$ mm (solid squares)). The jets of ref. [2] never reach the release height, because the granulate is less fine and much less decompactified. In our experiments jets are produced even at zero impact height [19] and there is no scaling relation as in ref. [2]. (b) Sketch of the void collapse. When the accelerated sand grains from the sidewalls of the cylindrical cavity collide on the axis of the cavity, two jets are formed: One downward into the entrained air bubble formed above the sphere, and one upward straight into the air.

passes the layer of sand at depth z. This sets the initial conditions for the two-dimensional collapse of the void at this depth, namely $R(z, t_{pass}) = R_0$ and $\dot{R}(z, t_{pass}) = 0$. Here, $R(z,t)$ is the time and depth dependent radius of the void, see figure 2.4b.

Next, the collapse of the void formed by the ball has to be described. It is driven by the ("hydrostatic") sand pressure $p(z)$ at depth z. For small z the pressure simply is $p(z) = \rho_s g z$, for larger z it saturates [17]. Here, ρ_s is the sand density, assumed to be constant. If we neglect the dissipative processes both between the different layers of sand and between the sand grains in one layer, the dynamics for fixed depth z is determined by the

Euler equation,

$$\rho_s(\partial_t v(r,t) + v(r,t)\partial_r v(r,t)) = -\partial_r p(r,t). \tag{2.1}$$

Here, $v(r,t)$ is the velocity field in the sand. With continuity $\partial_r(rv(r,t)) = 0$, and with the boundary conditions $v(R(t),t) = \dot{R}(t)$ at the void's wall and $v(R_\infty, t) = 0$ far away from the void, one obtains a Rayleigh-type [20, 21] ordinary differential equation for each $R(z,t)$, namely (cf. Section 1.3)

$$(R\ddot{R} + \dot{R}^2)\log\frac{R}{R_\infty} + \frac{1}{2}\dot{R}^2 = \frac{1}{\rho_s}p(z) = gz. \tag{2.2}$$

The radius R_∞ is of the order of the system size, but the results only weakly (logarithmically) depend on this parameter. The dynamics following from this Rayleigh-type model is shown in figure 2.3, resembling the void collapse in the discrete particle simulations figure 2.2, in the 2D experiments [8], in experimental work on the void collapse in transparent fluids [3–7, 15], in boundary integral simulations of the complete hydrodynamical equations [18], and therefore presumably also in the 3D experiments in sand shown in figure 2.1. Just before and at the singularity ($R(t) = 0$ and diverging velocity), the dynamics is determined by $R\ddot{R} + \dot{R}^2 = 0$, which has the solution $R(t) \sim (t_s - t)^{1/2}$, where t_s is the time of the singularity. The velocity therefore has a square-root divergence $\dot{R}(t) \sim (t_s - t)^{-1/2}$.

Having shown that the void collapse is driven by "hydrostatic" pressure, we now can deduce scaling arguments [22], for the limiting case of large impact velocity v_0, which is the relevant one in the geophysical context. The time up to void collapse in depth z is the sum of the time z/v_0 it takes the ball to get there and the collapse time itself, which scales as $\sim R_0/\sqrt{gz}$. The depth z_c where the walls of the void first touch (i.e., the position of the singularity) can be obtained from minimizing this sum with respect to z, resulting in $z_c/R_0 \sim Fr^{1/3}$, where $Fr = v_0^2/(gR_0)$ is the Froude number. From this one obtains that the time of the collapse t_c scales as $t_c \sim (R_0/v_0)Fr^{1/3} \sim \sqrt{R_0/g}Fr^{-1/6}$ [22]. For large v_0 these scaling laws are consistent both with our continuum model.

We now discuss the role of the ambient air and the ambient pressure for the evolution of the jet: (i) For (3D) experiments with very high impact velocities we observed that after the splash the crown goes *inwards* rather than outwards, due to the pressure reduction behind the fast projectile (Bernoulli's law). The crown in fact can fully close and the jet then hits the closed crown, leading to an explosion-like collision which spreads material all over the place. (ii) In impact experiments on very fine and loose sand but with strongly reduced ambient pressure the jet in fact is *less* pronounced than with ambient pressure [23]. For larger particles (500 μm) we redid above discrete particle simulations, but now reduced the air pressure to zero (vacuum) after fluidization. These simulations give very similar results for the jet formation compared to experiments and simulations under the same conditions at atmospheric pressure. More research on the role of air in loose fine granular material clearly is required.

2.3 Conclusion

We conclude the chapter with speculations on possible implications of our findings on the impact mechanism within the geophysical context [13, 24–28]. In general, impacts can be described using two dimensionless parameters: the Froude number ($\mathrm{Fr} = V^2/gR$) and the (inverse) Newton number ($\mathrm{Nt}^{-1} = \rho V^2/Y$, where ρ, V, and R are the density, velocity, and radius of the impactor respectively and Y is the yield stress of the target [27]. Although the *absolute* energy scales in our experiment are of course very different as compared to geophysical events, the *relative* scales are comparable: very large-scale planetary impacts ($Y \approx 10$ kbar, $R \approx 100$ km, and $V \approx 10$ km/s) and our experiments ($Y \approx 10$ Pa, $R \approx 1$ cm, and $V \approx 3$ m/s) both lead to Froude and Newton numbers of the same order: $Fr \approx 10^2$ and $Nt^{-1} \approx 10^3$. At this point we would like to caution the reader to directly translate or upscale the results of our laboratory experiments to the geophysical scales as in addition to the aforementioned difference in absolute energy scales, lack of reproducibility of the details typify geophysical events. Nonetheless, we believe that the following speculations may stimulate discussions in a geophysical context: (i) After the impact of a solid body on a planet, it may be the upward jet and *not* the splash which is the dominant source of planetary material transferred into space [25]. Similarly, an oblique jet resulting from an oblique impact (not shown here; in that case the jet goes *backwards* !) allows for an enhanced sidewards transport of material, as compared to the splash. (ii) The collapsing jet may contribute to the central peak often found in impact craters [13, 14]. (iii) The downward jet will considerably change the layering of the sediments underneath a crater, as it provides a mechanism how surface material can be transported deep into the ground. In addition, a granular eruption will rearrange the sediment. Our suggested mechanism may shed new light on the sediment layering data found underneath the Chicxulub crater, which is a source of major controversy [29–32].

References

[1] E.M. Shoemaker, *Why study impact craters*, in *Impact and Explosion Cratering*, edited by D. J. Roddy, R. O. Pepin, and R. B. Meril, 1–10 (Pergamon Press, New York, 1977).

[2] S.T. Thoroddsen and A.Q. Shen, *Granular jets*, Phys. Fluids **13**, 4 (2001).

[3] A.M. Worthington, *A study of splashes* (Longman and Green, London, 1908).

[4] H.N. Oguz and A. Prosperetti, *Bubble entrainment by the impact of drops on liquid surfaces*, J. Fluid Mech. **219**, 143 (1990).

[5] A. Prosperetti and H. Oguz, *The impact of drops on liquid surfaces and the underwater noise of rain*, Ann. Rev. Fluid Mech. **25**, 577 (1993).

[6] J.E. Hogrefe, N.L. Peffley, C.L. Goodridge, W.T. Shi, H.G.E. Hentschel, and D.P. Lathrop, *Power-law singularities in gravity-capillary waves*, Physica D **123**, 183 (1998).

[7] D. Lohse, *Bubble puzzles*, Phys. Today **56**, 36 (2003).

[8] R. Mikkelsen, , M. Versluis, G. W. Bruggert, E. Koene, D. van der Meer, K. van der Weele, and D. Lohse, *Granular eruptions: Void collapse and jet formation*, Phys. Fluids **14**, S14 (2002).

[9] C.-h. Liu, S.R. Nagel, D.A. Schecter, S.N. Coppersmith, S. Majumdar, O. Narayan, and T.A. Witten, *Force fluctuations in bead packs*, Science **269**, 513 (1995).

[10] H.M. Jaeger, S.R. Nagel, and R.P. Behringer, *Granular solids, liquids, and gases*, Rev. Mod. Phys. **68**, 1259 (1996).

[11] L.P. Kadanoff, *Built upon sand: Theoretical ideas inspired by granular flows*, Rev. Mod. Phys. **71**, 435 (1999).

[12] C.S. O'Hern, S.A. Langer, A.J. Liu, and S.R. Nagel, *Force distributions near jamming and glass transitions*, Phys. Rev. Lett. **86**, 111 (2001).

[13] P.H. Schultz, *Atmospheric effects on ejecta emplacement and crater formation on venus from magellan*, J. Geophys. Res. **97**, 16183 (1992).

[14] A.M. Walsh, K.E. Holloway, P. Habdas, and J.R. De Bruyn, *Morphology and scaling of impact craters in granular media*, Phys. Rev. Lett. **91**, 1043011 (2003).

[15] J.W. Glasheen and T.A. McMahon, *Vertical water entry of disks at low froude numbers*, Phys. Fluids **8**, 2078 (1996).

[16] J. Li and J.A.M. Kuipers, *Gas-particle interactions in dense gas-fluidized beds*, Chem. Eng. Sci. **58**, 711 (2003).

[17] J. Duran, *Sands, powders, and grains* (Springer, New York, 1999), first ed.

[18] S. Gaudet, *Numerical simulation of circular disks entering the free surface of a fluid*, Phys. Fluids **10**, 2489 (1998).

[19] D. Lohse, R. Rauhe, R. Bergmann, and D. van der Meer, *Granular physics: Creating a dry variety of quicksand*, Nature **432**, 689 (2004).

[20] Lord Rayleigh, *On the pressure developed in a liquid during the collapse of a spherical cavity*, Philos. Mag. **34**, 94 (1917).

[21] H.N. Oguz and A. Prosperetti, *Dynamics of bubble growth and detachment from a needle*, J. Fluid Mech. **257**, 111 (1993).

[22] H.N. Oguz, A. Prosperetti, and A.R. Kolaini, *Air entrapment by a falling water mass*, J. Fluid Mech. **294**, 181 (1995).

[23] J.R. Royer, E.I. Corwin, A. Flior, M.-L. Cordero, M.L. Rivers, P.J. Eng, and H.M. Jaeger, *Formation of granular jets observed by high-speed x-ray radiography*, Nat. Phys. **1**, 164 (2005).

[24] D.J. Roddy, R.O. Pepin, and R.B. Meril (Eds.), *Impact and Explosion Cratering* (Pergamon Press, New York, 1978).

[25] J.D. O'Keefe and T.J. Ahrens, *Meteorite impact ejecta: Dependence of mass and energy lost on planetary escape velocity*, Science **3.198**, 1249 (1977).

[26] H.J. Melosh, *Impact Cratering: A Geologic Process* (Oxford University Press, Oxford, 1989).

[27] K.A. Holsapple, *The scaling of impact processes in planetary sciences*, Ann. Rev. Earth Planet. Sci. **21**, 333 (1993).

[28] E. Pierazzo and H.J. Melosh, *Understanding oblique impacts from experiments observations, and modeling*, Ann. Rev. Earth Planet. Sci. **28**, 141 (2000).

[29] G. Keller, J.G. Lopez-Oliva, W. Stinnesbeck, and T. Adatte, *Age, stratigraphy, and deposition of near-k/t siliciclastic deposits in Mexico: Relation to bolide impact?*, Geol. Soc. Am. Bull. **109**, 410 (1997).

[30] J. Smit, *The global stratigraphy of the cretaceous-tertiary boundary impact ejecta*, Ann. Rev. Earth Planet. Sci. **27**, 75 (1999).

[31] L.E. Marin, V.L. Sharpton, J.U. Fucugauchi, J. Smit, P. Sikora, C. Carney, and M. Rebolledo-Vieyra, *Stratigraphy at ground zero: A contemporary evaluation of well data in the Chicxulub impact basin*, Int. Geol. Rev. **43**, 1145 (2001).

[32] G. Keller, W. Stinnesbeck, T. Adatte, B. Holland, D. Stuben, M. Harting, C. de Leon, and J. dela Cruz, *Spherule deposits in cretaceous-tertiary boundary sediments in Belize and Guatemala*, J. Geol. Soc **160**, 783 (2003).

Chapter 3

Creating a dry variety of quicksand [‡]

Sand can normally support a weight by relying on internal force chains [1–3]. Here we weaken this force-chain structure in very fine sand by allowing air to flow through it: we find that the sand can then no longer support weight, even when the air is turned off and the bed has settled a ball sinks into the sand to a depth of about five diameters. The final depth of the ball scales linearly with its mass and, above a threshold mass, a jet is formed that shoots sand violently into the air.

3.1 Experiment

We allowed air to flow through very fine sand (typical grain diameter was about 40 μm), which was sitting in a container with a perforated base. The air stream was turned off before the start of the experiment and the sand allowed to settle (Section 3.3). The packing fraction of this sand was only 41%, compared with 55-60% for untreated sand. We call this fragile state of sand 'dry quicksand' (not to be confused with normal quicksand, which is a mixture of sand, clay and water).

A ping-pong ball of radius $R = 2.0$ cm, partly filled with bronze grains, was suspended above the treated sand so that it was just touching the surface. To release the ball without introducing any vibration, the thin rope supporting the ball was burned causing the ball to sink instantaneously

---

[‡] Published as: Detlef Lohse, Remco Rauhé, Raymond Bergmann, Devaraj van der Meer, *Creating a dry variety of quicksand*, Nature **432**, 689 (2004), including Supplementary Material.

into the sand (Fig. 3.1). Objects often make a splash when they hit sand [4, 5]; in this case there was no splash, as expected, but a straight jet of sand shot violently into the air after about 100 ms [4, 5]. The singularity leading to this jet formation has already been described in Chapter 2.

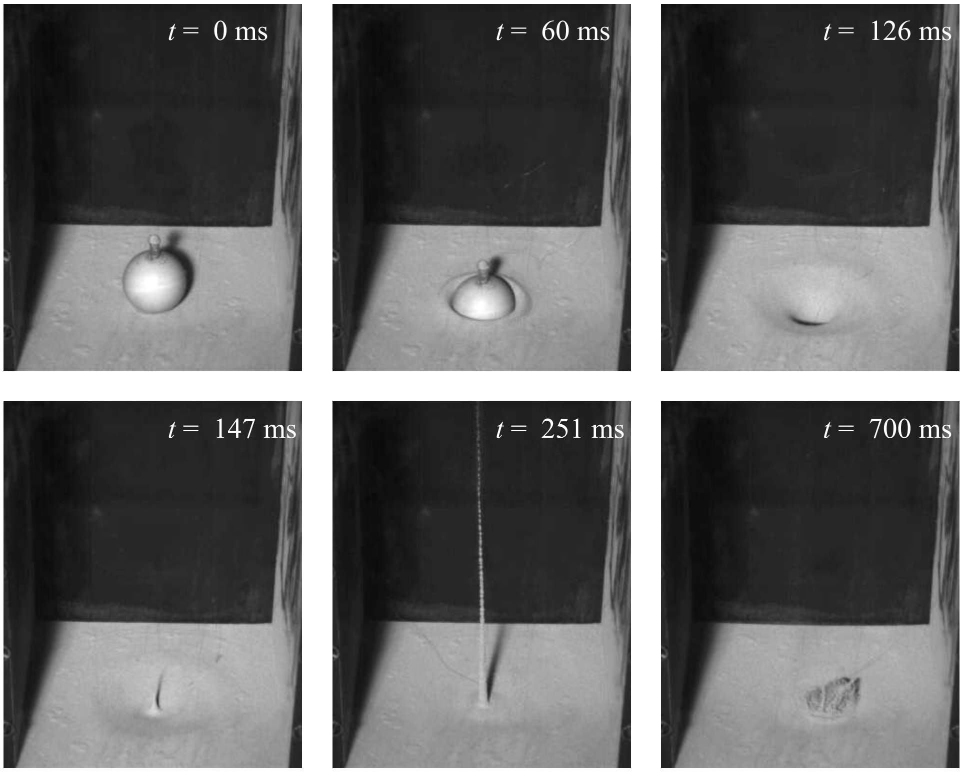

Figure 3.1: Snapshots of the sinking-ball experiment. At time $t = 0$ ms, the ball (mass $m = 133$ g) is released and immediately starts to sink into the sand; at $t \approx 130$ ms, a sand jet emerges, which reaches its final height at $t \approx 180$ ms. After about 600 ms, the trapped air bubble reaches the surface.

In experiments using a ball that has a stiff, almost mass-less tail, which allows for tracking of the sinking depth as a function of time, we find that the ball reaches a final depth of $z_{final} = 22.4$ cm (Fig. 3.2). This corresponds to more than five times its diameter. We investigated how this phenomenon is affected by the mass of the ball and found that the final depth reached by the ball increases linearly with its mass: that is, $z_{final} \propto m$. A visible jet only develops beyond a threshold mass of $m_{thres} = 28.5$ g (Fig. 3.2).

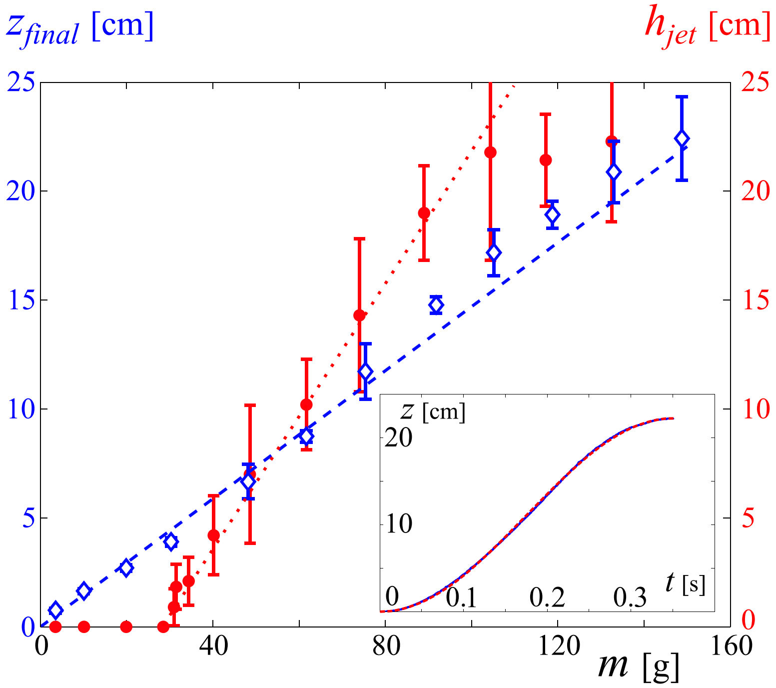

Figure 3.2: The jet height, h_{jet} (red circles), and the final depth of the ball, z_{final} (blue diamonds), as functions of the ball mass, m. Blue dashed line, linear fit with slope $2g/\kappa$; red dotted line, fit $h_{jet} \propto (m - m_{thres})^{1.0}$. The ball is released from rest from the surface of the sand (Fig. 3.1). Inset, depth of the ball, z, as function of time, t, for a ball of mass 148 g (experiment: blue curve; model: red curve).

3.2 A Coulomb drag model

We developed a simple force model to describe the dynamics of the ball in the sand and the parameter dependence of the final depth. The ball is accelerated by gravity and at the same time experiences a drag force, F_D, from the sand grains. For simplicity, we assume a Coulomb drag due to the normal forces from the side, which increases linearly with the depth z (ref. [6]); pressure saturation due to sidewall support (Rayleigh-Janssen law) occurs only at much greater depth. We therefore have $F_D = -\kappa z$, where κ is a constant; note that F_D does not depend on velocity. The equation of motion is thus

$$(m + m_A)\ddot{z} = mg - \kappa z \,, \tag{3.1}$$

where m_A is the 'added mass', meaning the mass of sand that is accelerated along with the moving ball. Equation (3.1) has to be supplemented by the initial conditions $z(0) = 0$ and $\dot{z}(0) = 0$. Integration of equation (3.1) immediately gives the final depth, $z_{final} = 2mg/\kappa$; that is, depth depends linearly on the mass. This agrees with the experimental findings shown in Fig. 3.2, from which we can read off $\kappa = (13.3 \pm 0.5)$ N/m. The full solution of equation (3.1) is

$$z(t) = \frac{1}{2} z_{final}(1 - \cos(\omega t)) \,, \tag{3.2}$$

for $0 \leq t \leq \pi/\omega$, where $\omega = \sqrt{\kappa/(m + m_A)}$. Equation (3.2) describes the dynamics extremely well (Fig. 3.2, inset). From the fitted ω, we obtain m_A as zero, within measurement precision.

In nature, dry quicksands may evolve from the sedimentation of very fine sand after it has been blown into the air and, if large enough, might be a threat to humans. Indeed, reports that travellers and whole vehicles have been swallowed instantly [7, 8] may even turn out to be credible in the light of our results.

3.3 Some further experimental details

The experiments described in the previous sections are performed in a 50 cm high container with a perforated bottom of 15.1×15.3 cm^2. The box is about half filled with very fine sand with an average diameter of 40 μm through which we then let air flow. Before the experiments we turn off the air stream and let the sand settle. The bed prepared in this way has a density of 897 kg/m^3, determined by measuring its total mass and the filling height after decompactification. With a quartz density (SiO_2) of 2200 kg/m^3 this corresponds to a packing density of only 41%.

A hollow ('ping-pong') ball of radius $R = 2.0$ cm, of which the mass can be varied by filling in bronze particles through a small hole on the top, is suspended above and just touching the surface of the sand. Either the position of ball is measured as a function of time (using a light but stiff rod attached to the top), or the emergence of the jet is imaged. For this we use a high speed camera at frame-rates of 1000 Hz and 2000 Hz.

When passing the surface the jet of figure 3.1 has $v = 3$ m/s tip velocity and eventually reaches a height of $h_{jet} = 25$ cm. A striking observation of figure 3.2 seems to be that the height of the jet is of the same order as the penetration depth of the sphere. This however turns out to be circumstantial: The jet height depends not only on the degree of decompactification and the impact velocity, but also on the size ratio of the impactor and the sand grains and even on the ambient gas pressure [4, 5, 9, 10].

We have performed experiments with differently shaped objects and with impact velocities larger than zero. In experiments with a disk released at the surface we found good agreement with our model, provided that we include a non-zero added mass in Eq. (3.1). In impact experiments with increasing impact velocity we find that the quality of the fit of our simple model to the experimental data deteriorates more and more. These experiments will be discussed elsewhere.

In the experiments reported in the present chapter we find the drag to be independent of velocity. This is consistent with Wieghardt [11], who reported an approximately constant drag for velocities up to 1 m/s. Indeed, also the velocities in the sinking experiments described in this chapter never exceed $g\sqrt{m/\kappa} \approx 1.0$ m/s [cf. Eq. (3.2)]. Also Chehata *et al.* [12] found a velocity-independent drag in vertical chute flow in the same low velocity regime.

3.4 Extension of the model

As indicated, the experiments were carried out starting from a situation with the ball positioned on top of the bed. In the model we approximate this initial condition with z=0 at t=0, neglecting the finite radius of the ball. One may argue that an initially half-immersed ball would be a more appropriate initial condition for our model.

However, from an experimental point of view, a ball only touching the bed of sand is very much to be favored since the ball can be positioned *after* the fluidization procedure, leaving the bed completely undisturbed. A half-immersed ball can only be realized by either pushing the ball into the bed (thus compactifying the region directly below the sphere) or by fluidizing while the ball has already been put into its position. This will cause stagnation and deflection of the air flow around the sphere and create uncontrollable inhomogeneities in the bed.

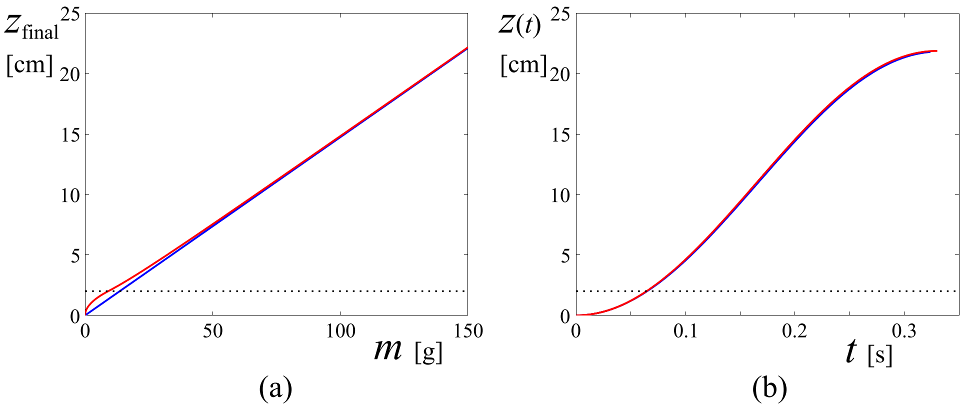

Figure 3.3: Comparison of the approximate model presented in the paper (blue curves) and the refined model (red curves) for $\kappa = 13.3$ N/m and sphere radius $R = 0.02$ m. (a) The final depth z_{final} reached by the sphere as a function of mass m. (b) Trajectory of a ball of mass $m = 148$ g. Note that the two curves practically coincide. The horizontal dotted line corresponds to the radius of the ball.

From a theoretical point of view, we can easily implement the finite radius correction into our model. We assume that between $z = 0$ and $z = R$ the drag force is reduced as compared to the approximate model, reflecting that in the beginning of the trajectory the ball is only partly immersed. E.g., we assume that only the immersed surface area of the sphere experiences the Coulomb drag force, leading to

$$F_D = \begin{cases} -\kappa z^2/R & \text{for } z < R \\ -\kappa z & \text{for } z \geq R \end{cases} \tag{3.3}$$

Using the appropriate boundary conditions $[z(0) = 0, \dot{z}(0) = 0]$, the equation of motion $m\ddot{z} = F_D + mg$ can be integrated with respect to the spatial coordinate. The final depth the ball reaches is determined by the condition $\dot{z}(z_{final}) = 0$ or

$$mgz_{final} = -\int_0^{z_{final}} F_D \, dz, \tag{3.4}$$

which is readily evaluated using eq. (3.3). In figure 3.3a the mass-dependence of z_{final} for the approximate and the refined model is compared. For small masses, i.e., those that lead to a final depth of the order of the ball radius

R, seizable differences are expected and found, but for larger masses the two models quickly converge to the proportionality law presented in Section 3.2.

In figure 3.3b the refined equations of motion are integrated over time for the same mass used for the plot in the inset of figure 3.2. The two models give practically indistinguishable results. Physically, the reason for this is that for larger masses the initial force acting on the particle is dominated by gravity; therefore variations of the precise form of the drag force during the very first stage of the movement do not significantly alter the trajectory followed by the sphere.

References

[1] C.-h. Liu, S.R. Nagel, D.A. Schecter, S.N. Coppersmith, S. Majumdar, O. Narayan, and T.A. Witten, *Force fluctuations in bead packs*, Science **269**, 513 (1995).

[2] H.M. Jaeger, S.R. Nagel, and R.P. Behringer, *The physics of granular materials*, Phys. Today **49**, 32 (1996).

[3] J.H. Snoeijer, T.J.H. Vlugt, M. van Hecke, and W. van Saarloos, *Force network ensemble: A new approach to static granular matter*, Phys. Rev. Lett. **92**, 543021 (2004).

[4] S.T. Thoroddsen and A.Q. Shen, *Granular jets*, Phys. Fluids **13**, 4 (2001).

[5] D. Lohse, R. Bergmann, R. Mikkelsen, C. Zeilstra, D. van der Meer, M. Versluis, K. van der Weele, M. van der Hoef, and H. Kuipers, *Impact on soft sand: Void collapse and jet formation*, Phys. Rev. Lett. **93**, 1980031 (2004).

[6] M.B. Stone, D.P. Bernstein, and R.l Barry, *Stress propagation: Getting to the bottom of a granular medium.*, Nature **427**, 503 (2004).

[7] T. E. Lawrence ("Lawrence of Arabia"), *Seven pillars of wisdom* (Doubleday, Anchor Books, New York, 1926).

[8] R.A. Bagnold, *The physics of blown sand and desert dunes* (Methuen and Co, London, 1941).

[9] A.M. Walsh, K.E. Holloway, P. Habdas, and J.R. De Bruyn, *Morphology and scaling of impact craters in granular media*, Phys. Rev. Lett. **91**, 1043011 (2003).

[10] J.R. Royer, E.I. Corwin, A. Flior, M.-L. Cordero, M.L. Rivers, P.J. Eng, and H.M. Jaeger, *Formation of granular jets observed by high-speed x-ray radiography*, Nat. Phys. **1**, 164 (2005).

[11] K. Wieghardt, *Experiments in granular flow.*, Ann. Rev. Fluid Mech. **7**, 89 (1975).

[12] D. Chehata, R. Zenit, and C.R. Wassgren, *Dense granular flow around an immersed cylinder*, Phys. Fluids **15**, 1622 (2003).

Chapter 4

The role of air in granular jet formation[‡]

A steel ball impacting on a bed of very loose, fine sand results in a surprisingly vigorous jet which shoots out from the surface of the sand [1]. When the ambient pressure is reduced, the jet is found to be less vigorous [2]. We find that the ambient pressure also affects the penetration depth of the ball and show that it is this change in penetration which determines the height of the jet. The observations are explained combining a Coulomb drag force model with a Rayleigh-type equation for the collapse of the void created by the ball. The origin of the deeper penetration under normal ambient pressure is found to lie in the extra sand fluidization caused by the air flow induced by the falling steel ball.

4.1 Introduction

When an object impacts on a bed of fine, loose grains, it is quickly engulfed and a surprisingly vigorous jet shoots out from the surface of the sand [1–5], similar to what happens in a liquid [6–10]. The understanding of this phenomenon comprises two different aspects: One is the dynamics of the object while moving through the granular material [5, 11–19]; the other is the mechanism by which the jet is formed when the void created by the object collapses under the action of gravity [1, 2, 4].

[‡] See also: Gabriel Caballero, Raymond Bergmann, Devaraj van der Meer, Andrea Prosperetti, and Detlef Lohse, *The role of air in granular jet formation*, submitted to Phys. Rev. Lett.

Royer *et al.* [2] found a granular jet created at reduced ambient pressure to be smaller than at atmospheric pressure, highlighting the relevant role that interstitial air plays in systems with very small grains ($< 100\mu$m) [20–24]. They also observed that at intermediate pressures, the shape of the jet consisted of a small thin structure on top of a much thicker one. By studying the effect of the pressure on the maximum height reached by the thin and the thick part of the jet, combined with high speed X-ray radiography, they concluded that the thin jet was caused solely by the collapse of the cavity while the thick jet was driven by a pressurized air pocket trapped in the sand.

In this chapter we present experiments where we found that the pressure-dependent reduction of the jet size goes hand in hand with a reduction of the final depth reached by the ball. We propose that it is this change in penetration depth which alters the size of the jet. Moreover, we show that the reduction of the jet size with the pressure is consistent with a mechanism of formation of the jet governed by the gravitational collapse of the void as proposed in [1]. Finally, we discuss experiments which suggest that the flow of air around the moving ball is responsible for the influence that the ambient pressure has on the drag force that the ball experiences inside the sand.

4.2 Impact experiment at reduced ambient pressure

For the experiments presented here we adapted the setup used in [1, 5] to allow for the evacuation of air. It consists of a deep bed (between 25 and 40 cm) of non-spherical sand grains with a mean size of about 40 μm. The cross section of the granular bed is a square of 14 cm per side. Before each impact experiment, air was blown through the bed from the bottom in order to decompactify and homogenize the sand. Then the air supply was slowly cut off and the bed was allowed to gently settle into a static, loose (41% volume fraction), weakened state. The container was subsequently sealed off and the air was slowly pumped out simultaneously from above and below the bed, lowering the pressure in the container at a rate of 5 mbar per second. We verified that there was no difference in measurements done when the evacuation of air was done at slower rates. When the desired pressure was attained, the valves were closed and a steel ball of diameter $D = 1.6$ cm was released from different heights.

A high speed camera filming from one side through the transparent walls of the container allowed to measure the maximum height h reached by the tip of the jet. The complete trajectory $z(t)$ of the ball inside the sand, from the moment of impact until its final depth z_{final}, was measured by attaching a thin thread with markers to the ball, which was kept tense during the process by running it through a small fastener. Because of the friction in this fastener, the measured effective acceleration of the falling ball before impact was about 10% smaller than gravity. In the following, each experimental point plotted is the average of three independent realizations, and the error bar is the corresponding standard deviation.

The maximum height of the jet h and the final penetration depth of the ball z_{final} are plotted as a function of the ambient pressure p in Fig. 4.1(a) and (b). In these plots four different impact velocities v_o were used, which are expressed in terms of the Froude number, defined as $\mathrm{Fr} \equiv 2v_o^2/gD$, where g is the acceleration of gravity. Both h and z_{final} are found to first increase with increasing pressure, astonishingly revealing a strong influence of the ambient pressure on the friction the ball experiences inside the sand. For pressures higher than $p \approx 400$ mbar the jet height saturates, quite unlike the penetration depth which has a more monotonic behavior. By plotting the jet height versus the final depth [Fig. 4.1(c)] two distinct regimes are revealed: (i) for low pressures, h increases more or less linearly with z_{final}, and (ii) for higher p the jet height saturates to a (Froude-dependent) constant value, whereas the penetration depth continues to increase.

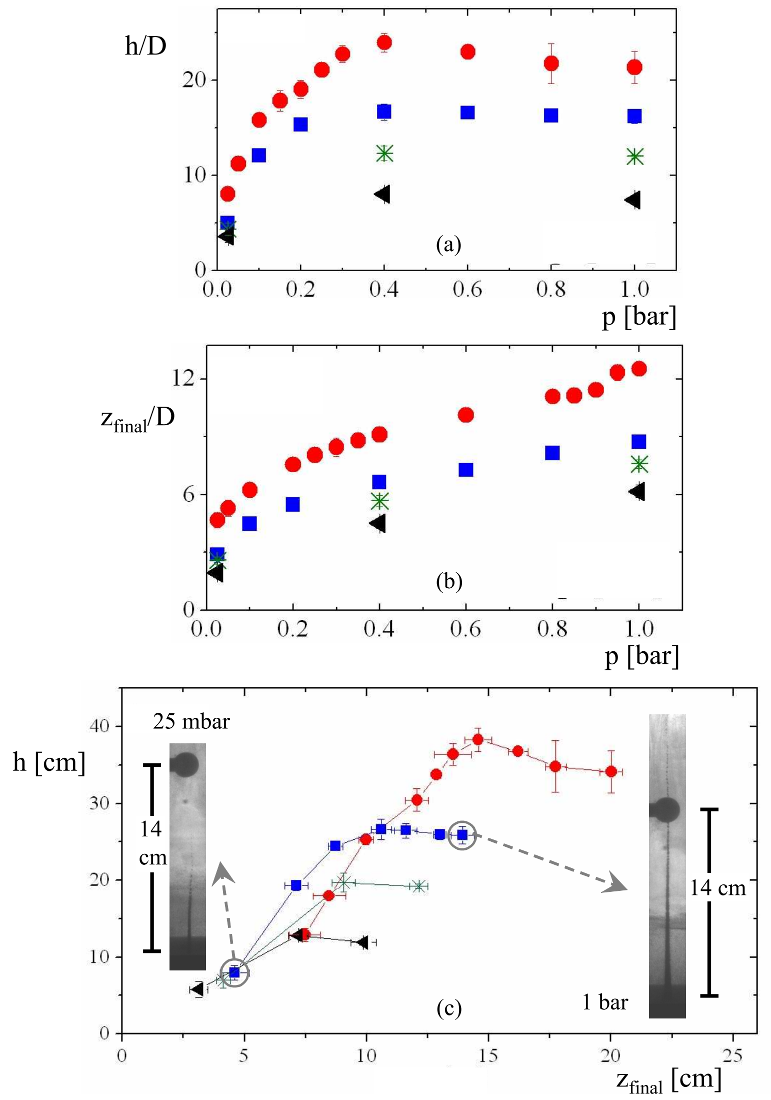

Figure 4.1: (a) Maximum height of the jet h, and (b) final depth of the ball z_{final}, as a function of the ambient pressure p for different Froude numbers: Fr = 7(◀), 18(⋆), 35(■), and 132(●). $D = 1.6$ cm is the diameter of the impacting ball. (c) Maximum height h of the jet versus the penetration depth z_{final} of the ball. Two regimes are clearly distinguishable: The first at low ambient pressure, where the jet height h increases linearly with the penetration depth z_{final}, independent of the Froude number, and the second at high pressures, where the jet height h saturates to a value independent of pressure and penetration depth. The lines in this plot are guides to the eye.

4.3 Trajectory of the ball

In order to explain the above observations we now turn to the complete trajectories $z(t)$ of the ball at four different pressures depicted in Fig. 4.2(a). The vertical dotted line marks the closure time t_c of the cavity at $p = 600$ mbar, which we were able to measure by a top-view, high-speed recording of the impact and cavity collapse*. The tangents of the trajectories at the moment of impact ($t = 0$) are identical, which reflects the fact that the impact velocity of the ball was the same in all the four experiments ($\mathrm{Fr} = 35$), but for $t > 0$ they start to diverge. A suitable measure for this divergence is the location z_i of the ball at $t = t_c$, which can be determined from the trajectories [Fig. 4.2(b)]. Clearly, for higher pressures ($p \gtrsim 400$ mbar) the values of z_i differ very little, reflecting the fact that trajectories are almost identical up to the time when the cavity closes. Therefore we infer that the cavity dynamics, the closure depth, and consequently also the jet formation process are the same. This explains why the jet height becomes constant for higher pressures: The impact velocity v_0 determines the jet height in this first regime†.

On the other hand at low pressures ($p < 400$ mbar), the trajectories deviate substantially during the interval $0 \leq t \leq t_c$ and therefore eventually z_{final} becomes the determining factor for the closure depth and consequently also for the jet height. So in this second regime the jet height h will become independent of the impact velocity and will be a function of z_{final} only, completely in agreement with our observations in Fig. 4.1(c).

4.4 Model of void creation and collapse

To describe the creation and subsequent collapse of the impact cavity we combine the drag force model for the impacting ball of [5] and the collapse model introduced in [1]. The drag force model of [5] is based on a drag force of the Coulomb form $F_d = -\kappa z$ (cf. Chapter 3), where z is the depth of the ball and κ is a constant. This leads to the equation of motion $m\ddot{z} = mg - \kappa z$,

---

* For $\mathrm{Fr} = 35$ we find a plateau at $t_c = 52$ ms at $p = 600$ mbar, which at lower pressures goes down to 42 ms with a similar trend as the closure depth in Fig 4.2(b). At $p = 1$ bar, the splash that is being dragged into the cavity obscures the observation of the cavity closure.

† The fact that the entrained air bubble will be dragged along with the ball at higher pressures, together with the relatively large pressure drop in the wake of the ball, could explain the slight decrease of the jet height for $p \gtrsim 400$ mbar as observed in Fig. 4.1(a) and (c).

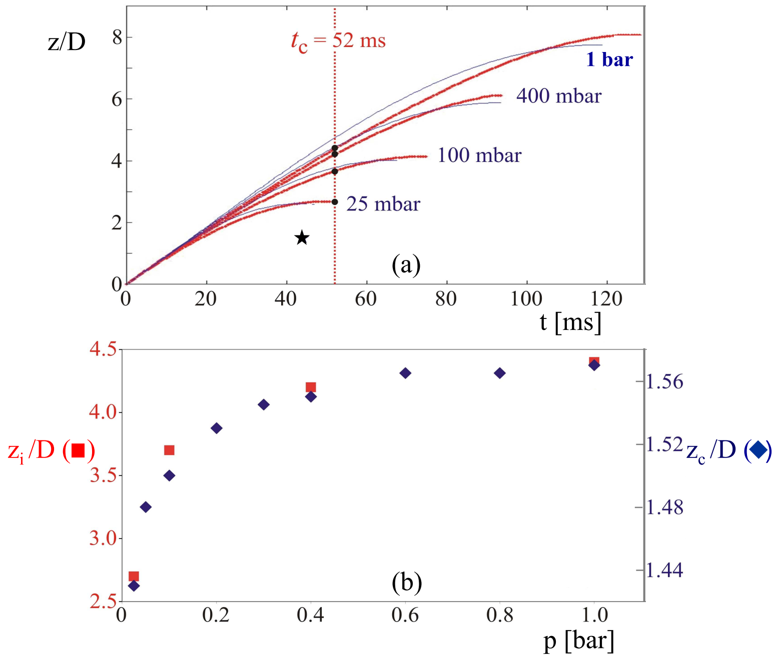

Figure 4.2: (a) Experimental (thick lines) trajectories of the ball in the sand compared to the prediction of the drag force model (thin lines) for four different pressures at Fr = 35. The vertical dotted line indicates the measured closure time t_c of the cavity. The black dots mark the location z_i of the ball at the time of closure. The blue star indicates the calculated closure time t_c and closure depth z_c using the model, the closure time is found to hardly depend upon the pressure. (b) Location of the ball at closure z_i from the top Figure (red squares, left axis) and the closure depth z_c obtained from the model (blue diamonds, right axis), both as a function of pressure. In order to permit a comparison between the two quantities, we plotted them on different vertical scales.

with intial conditions $z(0) = 0$ and $\dot{z}(0) = v_0$, which is readily solved to obtain the trajectory of the ball in the sand

$$z(t) = \frac{gm}{\kappa}\left[\sqrt{\frac{\mathrm{Fr}D\kappa}{2gm}}\sin\left(\sqrt{\frac{\kappa}{m}}t\right) - \cos\left(\sqrt{\frac{\kappa}{m}}t\right) + 1\right], \qquad (4.1)$$

for $0 \leq t \leq t_{stop}$, where t_{stop} is defined by the condition $\dot{z}(t_{stop}) = 0$. Inserting t_{stop} into the above equation gives the final depth the ball reaches as $z_{final} = (gm/\kappa)[1 + (1 + \kappa D\mathrm{Fr}/2gm)]$. In [5] it was shown that this model leads to an accurate description of the trajectory of the ball in our loose, fine sand at atmospheric pressure and zero impact velocity.

To evaluate how the model performs under $v_0 > 0$ and at lower ambient pressures, in Fig. 4.3(a) we compare the measured z_{final} as a function of the Froude number to the prediction of the model at three different pressures. The solid lines in Fig. 4.3(a) are the best fits of the equation for z_{final} to the experimental data, where the only free parameter is the drag force coefficient κ. The agreement between the model and the experiments is very good for low and intermediate Froude numbers, but they differ when Fr $\gtrsim$ 80. A plausible explanation of such behavior is that some velocity-dependent term needs to be included in the drag force on the ball [12–19], whose relative weight would increase with Fr. Since the introduction of such a velocity-dependent term in the drag force would introduce an additional fitting parameter, we chose not to consider such an extension here. From the fitting procedure leading to Fig. 4.3(a) we obtain the dependence of κ on the ambient pressure plotted in Fig. 4.3(b), which suggests a power-law relation of the form $\kappa \propto p^{-1/2}$. It is this empirical relation that we used to calculate the trajectories which are compared to the experimental ones in Fig. 4.2(a).

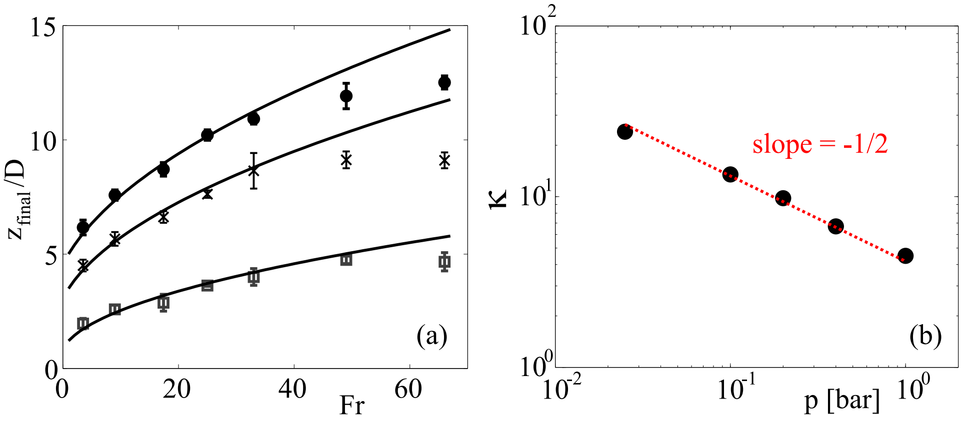

Figure 4.3: (a) Final depth as a function of the Froude number at different pressures p = 1(●), 0.4($\star$), and 0.025(□) bar. The lines are fits using the prediction of z_{final} by the force model, where the drag force coefficient κ is the only free parameter. The model describes the experimental data for low Froude numbers well. The values of κ that result from the fits are plotted in (b), suggesting a relation of the form $\kappa \propto p^{-1/2}$.

Now that we know the trajectory of the ball in the sand at different pressures, we can estimate the time t_c and depth z_c at which the void created by the ball first closes during its collapse, by proceeding in the same way as in [1]: The cavity is assumed to be cylindrical upon creation and starts to collapse radially immediately after the ball passes. Thus, the total time needed for the cavity to close at depth z is found by adding the time $t_{pass}(z)$ the ball needs to reach this depth (which follows directly from the calculated trajectory of the ball) and the time $t_{coll}(z)$ needed for the subsequent collapse at depth z. This last quantity follows from the two-dimensional Rayleigh equation introduced in [1], which can conveniently be rewritten in non-dimensional form by introducing $\hat{R} = 2R/D$ and $\hat{t} = t\,2\sqrt{gz}/D$

$$(\hat{R}\ddot{\hat{R}} + \dot{\hat{R}}^2)\log\frac{\hat{R}}{\hat{R}_\infty} + \frac{1}{2}\dot{\hat{R}}^2 = 1, \tag{4.2}$$

with initial conditions $\hat{R}(0) = 1$ and $\dot{\hat{R}}(0) = 0$. Note that the resulting non-dimensional initial value problem is independent of depth due to the assumption that the cavity is cylindrical upon creation, i.e., $\dot{R} = 0$. This is not the case if there would be some initial expansion of the cavity, corresponding to a nonzero initial velocity as a initial condition to Eq.(4.2).

By solving Eq.(4.2) we find a unique solution $\hat{R}(\hat{t})$, which becomes zero at $\hat{t} = \hat{t}_{coll}$, and which only depends on the value of $\hat{R}_\infty$. The z-dependence of dimensional collapse time t_{coll} now follows from $t_{coll} = \hat{t}_{coll}D/(2\sqrt{gz})$. If we equate R_∞ with half the container size, we find $\hat{t}_{coll} = 0.78$. The depth z_c and time t_c at which the cavity will collapse is now found by determining the minimum of this total time $t_{total}(z) = t_{pass}(z)+t_{coll}(z)$ with respect to z.

The resulting closure time t_c turns out to hardly depend on pressure, and is plotted as a single point (blue star) in Fig. 4.2(a). The calculated closure depth z_c however does depend on p and is compared to the experimentally determined location z_i of the ball at closure time in Fig. 4.2(b). Note that, although plotted with different vertical scales, the experimental quantity z_i and the calculated closure depth z_c show a remarkably similar trend: Both quantities are more or less constant for high pressures and show a sharp decrease below $p \approx 400$ mbar.

Moreover, this trend is the same as was observed for the jet height h in experiment, which can be explained by taking another look at the Rayleigh equation Eq. (4.2): By eliminating $\hat{t}$ between $\hat{R}(\hat{t})$ and $\dot{\hat{R}}(\hat{t})$ we find $\dot{\hat{R}}(\hat{R})$. From this we find the dimensional velocity to obey $\dot{R} = \sqrt{gz}\,f(R/R_0)$, where $f(x) \equiv \dot{\hat{R}}(x)$ is a function which only depends on R_∞. Since the initial jet diameter will be determined by geometrical and rheological considerations only, it can be set proportional to the grain diameter d (with a proportionality constant of order 10) with which we fix $f(R/R_0)$ and can estimate the pressure build-up at the collapse depth just before the jet comes out using Bernoulli's equation: $p \propto gz_c$. Since this pressure is then released into the jet, we can now estimate the jet height $h \propto v_{jet}^2 \propto p$. We thus find that in the model $h \propto z_c$ explaining not only the fact that h and z_c follow the same trend but also the observation of Fig 4.1(c) that when z_{final} determines the closure depth rather than Fr we find a linear relation between z_{final} and h.

We conclude that all the experimental observations are consistent with a gravitational collapse model of the cavity that is created upon impact. The ambient air would only indirectly affect the jet formation by influencing the drag force on the ball by the sand.

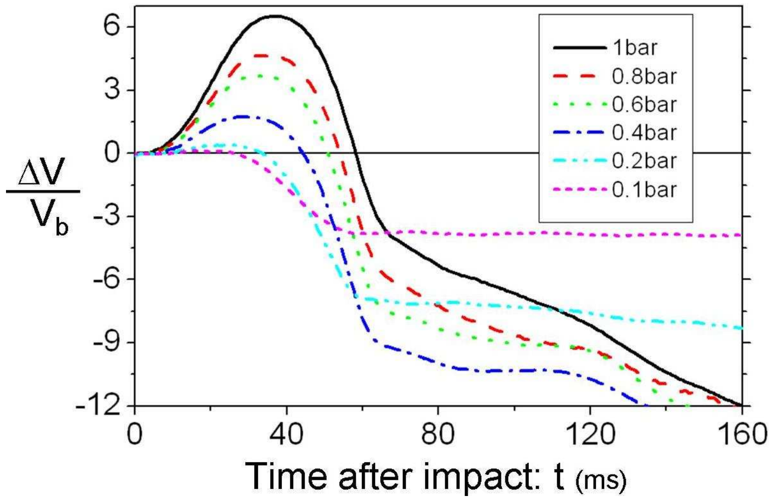

Figure 4.4: Behavior in time of the volume occupied by the sand bed after the impact of the ball for Fr = 132 and different pressures. $\Delta V = V(t) - V(t = 0)$, where $V(t)$ is the total volume occupied by the sand bed and $t = 0$ is the moment of impact. $V_b = (\pi/6)D^3$ is the volume of the impacting ball with $D = 1.6cm$. Each curve is the average of three independent experiments. The bed expands more at higher pressure, which is in accordance with our hypothesis of the fluidization of the bed due to the flow of interstitial air.

4.5 The origin of the increased drag at reduced pressure

But, how does the ambient pressure modify the rheological properties of the sand? We believe that the flow of interstitial air that the ball creates while moving through the sand further fluidizes the sand[‡], effectively reducing the drag on the ball. When the pressure is reduced there is less interstitial air, and the fluidization would be less important.

In order to test this idea we studied the change in the total volume occupied by the sand bed after the impact of the ball by imaging with a fast video camera (at 1500 frames per second) one of the lateral, transparent walls of the container at the level of the bed surface. The product of the cross section of the container and the total height of the bed measured with the camera gave us an estimation of the total volume $V(t)$ occupied by the sand bed at time t. Figure 4.4 shows $\Delta V = V(t) - V(t = 0)$ for a Froude number of 132 and at different pressures, where $t = 0$ is the moment of impact. It can be seen that the bed expands more at higher pressure, which is in accordance with our hypothesis of the fluidization of the bed due to the flow of interstitial air.

Moreover, if one compares the (lower Fr) trajectories of Fig. 4.2(a) with the timescale of the rising in Fig. 4.4, one finds that at least for pressures above 400 mbar, the trajectories are almost identical while the expansion of the bed in this pressure range shows large differences. It can therefore be excluded that the observed differences in bed height can be attributed to the displacement of grains needed by the ball to create the cavity and the expansion of the bed must therefore indeed be due to the levitation of sand by the interstitial air flow.

4.6 Conclusion

In conclusion, we found that ambient air does not play a direct role in the formation of a granular jet in loose, fine sand. Instead, we have shown that the jet is less vigorous at reduced pressures because the ball penetrates

---

[‡] The idea that the evacuation procedure would somehow cause an irreversible change in the microstructure of the sand bed was discarded by a simple experiment: First the ambient pressure was reduced to a level of several tens of millibars and subsequently air was slowly let in until the system reached atmospheric pressure again. Conducting the impact experiment following this procedure gives exactly the same result as without.

less deep into the sand and consequently the collapse of the void is less violent. The effect of the ambient pressure on the intensity of the jet is indeed closely related to the "dynamic coupling between gas and granulate motion" [2]. Our experiments show that the origin hereof is that also the trajectory of the ball is strongly influenced by the ambient pressure, presumably because the air flow around the moving ball partially levitates the grains and effectively reduces the drag force on the ball.

Finally, in our experiments with a $D = 1.6$ cm ball we do not observe the thick jet reported by Royer *et al.* [2]. Changing the ball diameter to 2.5 cm does however produce both the thick and thin jet for high Fr numbers. We therefore speculate whether the thick jet may be due to boundary effects.

References

[1] D. Lohse, R. Bergmann, R. Mikkelsen, C. Zeilstra, D. van der Meer, M. Versluis, K. van der Weele, M. van der Hoef, and H. Kuipers, *Impact on soft sand: Void collapse and jet formation*, Phys. Rev. Lett. **93**, 1980031 (2004).

[2] J.R. Royer, E.I. Corwin, A. Flior, M.-L. Cordero, M.L. Rivers, P.J. Eng, and H.M. Jaeger, *Formation of granular jets observed by high-speed x-ray radiography*, Nat. Phys. **1**, 164 (2005).

[3] S.T. Thoroddsen and A.Q. Shen, *Granular jets*, Phys. Fluids **13**, 4 (2001).

[4] R. Mikkelsen, , M. Versluis, G. W. Bruggert, E. Koene, D. van der Meer, K. van der Weele, and D. Lohse, *Granular eruptions: Void collapse and jet formation*, Phys. Fluids **14**, S14 (2002).

[5] D. Lohse, R. Rauhe, R. Bergmann, and D. van der Meer, *Creating a dry variety of quicksand*, Nature **432**, 689 (2004).

[6] A.M. Worthington, *A study of splashes* (Longman and Green, London, 1908).

[7] H.N. Oguz and A. Prosperetti, *Bubble entrainment by the impact of drops on liquid surfaces*, J. Fluid Mech. **219**, 143 (1990).

[8] A. Prosperetti and H. Oguz, *The impact of drops on liquid surfaces and the underwater noise of rain*, Ann. Rev. Fluid Mech. **25**, 577 (1993).

[9] J.E. Hogrefe, N.L. Peffley, C.L. Goodridge, W.T. Shi, H.G.E. Hentschel, and D.P. Lathrop, *Power-law singularities in gravity-capillary waves*, Physica D **123**, 183 (1998).

[10] R. Bergmann, D. van der Meer, M. Stijnman, M. Sandtke, A. Prosperetti, and D. Lohse, *Giant bubble pinch-off*, Phys. Rev. Lett. **96**, 154505 (2006).

[11] H.J. Melosh, *Impact Cratering: A Geologic Process* (Oxford University Press, Oxford, 1989).

[12] M. Forrestal and V. Luk, *Penetration into soil targets*, Int. J. Impact Eng. **12**, 427 (1992).

[13] J. S. Uehara, M. A. Ambrosio, R. P. Ojha, and D. J. Durian, *Lowspeed impact craters in loose granular media*, Phys. Rev. Lett. **90**, 194301 (2003).

[14] A.M. Walsh, K.E. Holloway, P. Habdas, and J.R. De Bruyn, *Morphology and scaling of impact craters in granular media*, Phys. Rev. Lett. **91**, 1043011 (2003).

[15] M.B. Stone, D.P. Bernstein, and R.l Barry, *Stress propagation: Getting to the bottom of a granular medium.*, Nature **427**, 503 (2004).

[16] M.P. Ciamarra, A.H. Lara, A.T. Lee, D.I. Goldman, I. Vishik, and H.L. Swinney, *Dynamics of drag and force distributions for projectile impact in a granular medium*, Phys. Rev. Lett. **92**, 1 (2004).

[17] M. A. Ambroso, C. R. Santore, A. R. Abate, and D. J. Durian, *Penetration depth for shallow impact cratering*, Phys. Rev. E **71**, 051305 (2005).

[18] M. Hou, Z. Peng, R. Liu, K. Lu, and C. K. Chan, *Dynamics of a projectile penetrating in granular systems*, Phys. Rev. E **72**, 062301 (2005).

[19] L. S. Tsimring and D. Volfson, *Modeling of impact cratering in granular media*, in *Powders and Grains 2005*, edited by Garcia-Rojo, Herrmann, and McNamara, 1215 (Taylor and Francis Group, London, 2005).

[20] M. Faraday, *On a peculiar class of acoustical figures; and on certain forms assumed by groups of particles upon vibrating elastic surfaces*, Philos. Trans. R. Soc. **121**, 299 (1831).

[21] H. K. Pak, E. Van Doorn, and R. P. Behringer, *Effects of ambient gases on granular materials under vertical vibration*, Phys. Rev. Lett. **74**, 4643 (1995).

[22] N. Burtally, P. J. King, and Michael R. Swift, *Spontaneous air-driven separation in vertically vibrated fine granular mixtures*, Science **295**, 1877 (2002).

[23] X. Yan, Q. Shi, M. Hou, K. Lu, and C. K. Chan, *Effects of air on the segregation of particles in a shaken granular bed*, Phys. Rev. Lett. **91**, 014302 (2003).

[24] M. E. Moebius, X. Cheng, G. S. Karczmar, S. R. Nagel, and H. M. Jaeger, *Intruders in the dust: Air-driven granular size separation*, Phys. Rev. Lett. **93**, 198001 (2004).

Chapter 5

Giant bubble pinch-off[‡]

Self-similarity has been the paradigmatic picture for the pinch-off of a drop. Here we will show through high-speed imaging and boundary integral simulations that the inverse problem, the pinch-off of an air bubble in water, is not self-similar in a strict sense: A disk is quickly pulled through a water surface, leading to a giant, cylindrical void which after collapse creates an upward and a downward jet. Only in the limiting case of large Froude number the purely inertial scaling $h(-\log h)^{1/4} \propto \tau^{1/2}$ *[1] for the neck radius* h *becomes visible. For any finite Froude number the collapse is slower, and a second length-scale, the curvature of the void, comes into play. Both length-scales are found to exhibit power-law scaling in time, but with different exponents depending on the Froude number, signaling the non-universality of the bubble pinch-off.*

5.1 Introduction

The pinch-off of a liquid drop is a prime example of a hydrodynamic singularity and has been studied extensively in recent years [2–5]. It has become paradigmatic for self–similar behavior in fluid dynamics: After appropriate rescaling, the shapes of the pinching neck at different times can be superimposed onto a single shape [6–9]. With the exception of some pioneering work [10, 11], the *inverse* problem of the collapse of a gas–filled neck surrounded by a liquid has not attracted much attention until very recently, with the analysis of the pinch-off of a bubble rising from a needle and the break–up of a gas bubble in a straining flow [1, 12–14]. The

---

[‡] Published as: Raymond Bergmann, Devaraj van der Meer, Mark Stijnman, Marijn Sandtke, Andrea Prosperetti, and Detlef Lohse, *Giant bubble pinch-off*, Phys. Rev. Lett. **96**, 154505 (2006).

time–evolution of these collapsing gas–filled necks is found to follow a power law. If the dynamics near the singularity are solely governed by liquid inertia, then the radius of the neck h expressed in the time τ remaining until collapse scales as $h \propto \tau^{1/2}$ [10, 11, 14], or, with a logarithmic correction, as $h(-\log h)^{1/4} \propto \tau^{1/2}$ [1]. Deviations from this exponent of 1/2 are reported to occur only due to the inclusion of other effects. The collapse may be slowed down by viscosity ($h \propto \tau$ [13, 14]) or surface tension ($h \propto \tau^{2/3}$ [12]), or accelerated by the inertia of the gas flowing inside the neck, leading to $h \propto \tau^{1/3}$ [1].

In this chapter we focus on another example of this "inverse pinch-off", namely the violent collapse of the void created at a fluid surface by the impact of an object. Here we find exponents which deviate substantially from 1/2, even though the dynamics are shown to be purely governed by liquid inertia, without significant contributions from the effects mentioned above. The self-similar behavior $h(-\log h)^{1/4} \propto \tau^{1/2}$ appears to hold only in the asymptotic regime of very high impact velocities.

5.2 Experiment

In our experiment, a linear motor is used to drag metal disks with radii h_{disk} between 10 and 40 mm through an air/water interface with a well-controlled, constant velocity V between 0.5 and 3 m/s (see Fig. 5.1a). A rod running through a seal in the bottom of a large water tank connects the disk with the linear motor. This arrangement generates giant voids in a very controlled fashion. The advantage of this setup is that the velocity is a *control parameter* and not the response of the object to the fluid forces upon impact. Secondly, due to the large scale of the experiment, viscosity and surface tension play a negligible role[†]. Therefore the only important dimensionless parameter is the Froude number $\mathrm{Fr} = V^2/(h_{disk}g)$, the ratio of kinetic to gravitational energy, which ranges from 0.6 to 90. The large scale of the experiment is also advantageous for the observation of details during the impact and collapse process, which is imaged with digital high-speed cameras with frame rates up to $100,000$ frames per second.

[†] Viscosity and surface tension effects are quantified by the magnitude of the Reynolds (Re) and Weber (We) numbers, which are considerable ($> 10^2$) during the pinch-off process. This holds when they are defined globally, i.e., with respect to the impact velocity and the disk radius ($\mathrm{Re} = h_{disk}V/\nu$ and $\mathrm{We} = h_{disk}V^2\rho/\sigma$), but also when they are defined locally using the neck radius and velocity at a specific time ($\mathrm{Re} = h\dot{h}/\nu$ and $\mathrm{We} = h\dot{h}^2\rho/\sigma$).

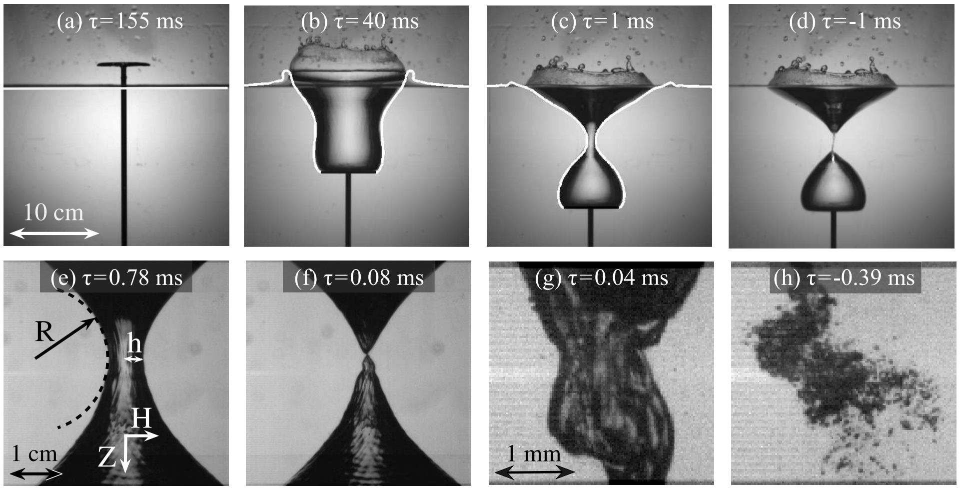

Figure 5.1: Snapshots of the formation and collapse of a surface void for the plunger experiment: A linear motor pulls down a disk of radius $h_{disk} = 30$ mm through the water surface at a constant velocity $V = 1.0$ m/s (Fr = 3.4). (a-d) Collapse of the void imaged at a 1000 frames per second (fps). The white lines (overlay) are the void profiles obtained from boundary integral simulations with the same initial condition, and without the use of any free parameter. (e-f) Details of the collapse imaged at 12800 fps. (g-h) Details of the collapse imaged at 48000 fps. Note that the field of view decreases with increasing frame rate. In the very last stages of the collapse (f-g) there is a Kevin-Helmholtz instability that complicates the determination of the time of collapse. Immediately after the collapse air is entrapped, both in the form of a large bubble above disk (d) and as a cloud of microbubbles at the collapse point (h).

A typical series of events is seen in Fig. 5.1a-d. The impact of the disk creates an axisymmetric void which first expands until the hydrostatic pressure drives the walls inward. The inward moving walls collide and cause a pinch-off at some depth below the undisturbed free surface. The energy focusing of this violent collapse creates a strong pressure spike on the axis of symmetry which releases itself in a downward and an upward jet [15, 16]. The latter reaches heights exceeding 1.5 m for the higher impact speeds in this experiment. It is this dominating role of inertia that makes our system different from other pinch-off processes in the literature. At higher recording speeds the pinch-off can be investigated in more detail as in Fig. 5.1e-h. There is a clear loss of both azimuthal and axial symmetry in Figs. 5.1f and 5.1g, which can be attributed to a combination of the same convergence effect that causes an instability in a collapsing bubble [17–19], and a Kelvin-Helmholtz instability due to the rapid air flow in the neck.

The latter increases with increasing Froude number and limits the range of our experiments. Another factor which limits the Froude number range is the so-called surface seal, in which the void closes at the water surface as the crown-like splash is entrained by the air flowing into the expanding void [20, 21]. This process, which occurs at large Froude numbers, changes the pinch-off considerably since in this case the gas pressure inside the void differs appreciably from that of the ambient air.

In view of these experimental limitations, we performed numerical simulations using a boundary integral method based on potential theory *without* ambient gas[*]. There is an excellent agreement between the numerical calculations and the experiments, as seen in Fig. 5.1a-c. Here, the numerical void profiles (the solid white lines) coincide very well with the experimental profiles in the pinch-off region without the use of any adjustable parameter, either in space or in time.

5.3 Time evolution of the neck radius

To further quantify the pinch-off process, we now turn to the time evolution of the neck radius $h(\tau)$, measured at the depth at which the void eventually closes. Because both length and time scales become very small close to collapse, it is not feasible to experimentally observe the collapse with only one high-speed camera recording[†]. Due to the reproducibility of the experiment, we overcame this difficulty by matching several data sets imaged at different frame rates, increasingly magnifying the region around the pinch-off. Figure 5.2a contains a doubly logarithmic plot of $h(\tau)$ for both the high-speed imaged experiments and the numerical calculations, again showing excellent agreement for different Froude numbers. There is a clear power-law behavior. Compensating the data with $\tau^{1/2}$ (Fig. 5.2b) and subsequently plotting the corresponding power-law exponent α_h as a function of Fr (Fig. 5.2d) reveal large deviations from the suggested 1/2 power law. Can these be explained by a logarithmic correction as proposed in [1]?

---

[*] The ambient air will be included in a forthcoming publication, also using the boundary integral method.

[†] We image the pinch-off process over four orders of magnitude in time and two in space. As the field of view of the camera corresponds to 10^3 pixels, this would leave only 10 pixels for the last stage of the collapse. The whole sequence should then be imaged at a frame rate corresponding to the smallest timescale (10μs), i.e., 100 kHz requiring at least 10 GB of fast storage capacity, greatly exceeding the physical capabilities of our cameras.

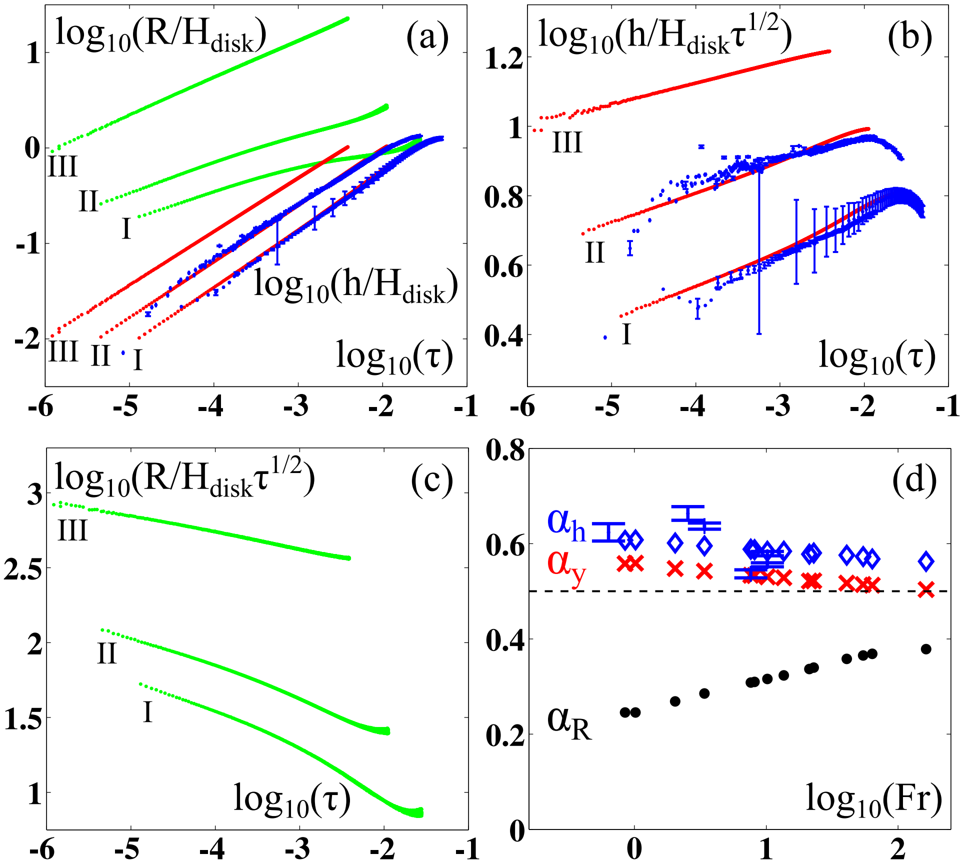

Figure 5.2: (a) The radius of the void at the depth of closure h (lower three curves) and the radius of curvature of the void profile R (upper three curves) as a function of the time τ remaining until collapse in a doubly logarithmic plot, for Fr = 3.4 (I), Fr = 10.2 (II), and Fr = 163 (III). Both h and R are well described by power laws for up to four orders of magnitude in τ. Experiment (blue dots) and numerical simulations (red dots) agree very well for Fr = 3.4 and 10.2. For Fr = 163 only numerical data are presented, because here experiments are hindered by the surface seal (see text). The error bars, indicating the error in the experimental data, are usually small, but occasionally become large for frames very close to the collapse time. (b) Doubly logarithmic plot of the void radius h compensated with $\tau^{1/2}$ to better show the deviations from the expected power-law behavior. (c) Doubly logarithmic plot of the radius of curvature R compensated with $\tau^{1/2}$ for the numerical simulations of (a-b). (d) Power-law exponents α_h for the radius of the void at closure depth $h(\tau)$, α_y for the radius of the void including the logarithmic correction $y(\tau) = h(-\log h)^{1/4}$, and α_R for the radius of curvature R, all as a function of the Froude number.

Let us first establish the origin of this logarithmic correction in our system. Near the neck, the flow induced by the collapsing void looks very much like that of a collapsing cylinder, while it must look like that of a sink, plus its image in the free surface (i.e., a dipole) in the far region. In the language of singular perturbations, the former would be the inner region and the latter the outer region; a complete descriptions would require the matching of these two regions. If we disregard the outer region, we can use a two-dimensional version of the Rayleigh-equation, which describes the collapse of an infinite cylindrical cavity under uniform pressure [11, 16, 22]

$$\left[\frac{d(h\dot{h})}{d\tau}\right]\log\frac{h}{h_\infty}+\frac{1}{2}\,\dot{h}^2=gZ \quad . \tag{5.1}$$

The pressure difference driving the collapse has been equated to $\rho g Z$, where Z denotes the depth below the fluid surface, which implies that the system is composed of non-interacting horizontal layers of fluid, with a negligible vertical velocity component[‡]. Although the quantity h_∞ must in principle be determined by the matching process alluded to before, it is expected to be of the order of a typical length scale of the process, such as the cavity depth. Thus, strictly speaking, h_∞ is a function of time and of the Froude number. However, near pinch-off, the time scale for the neck motion is much faster than that for the evolution of the other parts of the cavity so that h_∞ may be considered only a function of Fr. After an initial expansion of the void, the collapse starts from rest at a maximal radius h_{max} (of the order of h_{disk}). Using this as an initial condition, and treating h_∞ as a constant, the energy integral of Eq. (5.1) can be readily found:

$$\left(\frac{d\tilde{h}}{d\tilde{\tau}}\right)^2=\frac{1}{\log(\tilde{h}/\tilde{h}_\infty)}\left[1-(1/\tilde{h})^2\right] \quad , \tag{5.2}$$

where we have introduced the non-dimensional variables $\tilde{h}\equiv h/h_{max}$, $\tilde{h}_\infty\equiv h_\infty/h_{max}$, and $\tilde{\tau}\equiv\tau\sqrt{gZ/h_{max}^2}$. Close to pinch-off, $\tilde{h}^2\ll 1$, such that $\tilde{h}^{-2}-1\approx\tilde{h}^{-2}$. With this approximation, we can integrate Eq. (5.2) once more to arrive at

$$2\,\tilde{\tau}=\tilde{h}^2\sqrt{\log(\tilde{h}_\infty/\tilde{h})}+\sqrt{\frac{\pi}{2}}\,\tilde{h}_\infty^2\,\mathrm{erfc}\left(\sqrt{2\log(\tilde{h}_\infty/\tilde{h})}\,\right). \tag{5.3}$$

For small $\tilde{h}$ the term with the complementary error function is always small compared to the first one and their ratio vanishes for $\tilde{h}\downarrow 0$. Neglecting this

---

[‡] A similar equation is used in [1], without the term h_∞ and also without the hydrostatic driving pressure gZ.

term we find two asymptotic regimes

$$\tilde{h}\left(\log(\tilde{h}_\infty)\right)^{1/4} = \sqrt{2}\,\tilde{\tau}^{1/2} \quad \text{for } \tilde{h} \gg 1/\tilde{h}_\infty \text{ , and} \tag{5.4}$$

$$\tilde{h}\left(-\log(\tilde{h})\right)^{1/4} = \sqrt{2}\,\tilde{\tau}^{1/2} \quad \text{for } \tilde{h} \ll 1/\tilde{h}_\infty \text{ .} \tag{5.5}$$

From Eqs. (5.4) and (5.5) we conclude that the scaling depends crucially on the value of h_∞: Initially, for the intermediate regime $h \gg h_{max}^2/h_\infty$, we expect to find a strict power law $h \propto \tau^{1/2}$, since $\log(\tilde{h}_\infty)$ is constant. For times closer to the pinch-off, when $h \ll h_{max}^2/h_\infty$, logarithmic corrections play a role, and the power law should be modified into Eq. (5.5).

As $h_\infty \approx h_{max}$ in our experiments, the latter inequality can be read as $h \ll h_{max}$, which is satisfied in most of the region where $h(\tau)$ asymptotically behaves as a power law (cf. Fig. 5.2a-b). We conclude that in our system the logarithmic correction cannot be neglected. If we plot the quantity $y = h(-\log h)^{1/4}$ vs. time, we again observe a power law $y \propto \tau^{\alpha_y}$, but with a slightly different exponent α_y than the one found for h. In Fig. 5.2d we compare α_h and α_y as functions of the Froude number. As discussed before, α_h is substantially larger than 1/2, but even if the logarithmic term is included we continue to find a slower collapse for low Froude numbers. Although the logarithmic correction does bring the result closer to the suggested value 1/2, it cannot account for all of the observed deviations.

Clearly, the observed anomalous power law behavior of the neck radius must reflect itself in the time-evolution of the free-surface profiles of the collapsing void. If the process were self-similar, the free-surface profiles at different times τ would superpose when scaled by any characteristic length, e.g., the neck radius h. Actually, it is found that the depth of minimum radius increases somewhat as the collapse progresses and it is therefore necessary to translate the profiles in the vertical direction so as to match the position of the minimum radius point before attempting this operation. Even if this is done, however, the results fail to collapse onto a single shape when using a single length-scale. The rescaled profiles become more and more elongated as the pinch-off is approached which proves that the collapsing void is *not* self-similar in a strict sense.

5.4 Time evolution of the void profile near pinch off

The free-surface shapes near the minimum point should thus not only be characterized by $h(\tau)$, but also by a second length-scale, the radius of curvature $R(\tau)$ in the vertical plane (see Fig. 5.1e). The spatial resolution of the high-speed camera images limits the accuracy with which R can be extracted from the experimental observations, but this quantity is easily determined from the numerical calculations (see Fig. 5.2a,c). When the radial dimensions (H, cf. Fig. 5.1e) are scaled by h and vertical ones (Z) by $\sqrt{hR}$, the profiles do collapse onto a single curve. This, however, may only signal that their shape is very close to parabolic[§]. The time-evolution of this radius of curvature is also found to follow a power law, $R = R_0 \tau^{\alpha_R}$, the exponent α_R of which increases with the Froude number as can be seen in Fig. 5.2d[¶].

The essence of the time-evolution of the void profile and the departure from self-similarity in the strict sense is captured in the aspect ratio h/R of the collapsing void, $h(\tau)/R(\tau) = (h_0/R_0)\, \tau^{(\alpha_h - \alpha_R)}$, in which the prefactor h_0/R_0 and the exponent $(\alpha_h - \alpha_R)$ both are found to depend on the Froude number. It is seen in Fig. 5.2d that $\alpha_h - \alpha_R > 0$ for any finite Froude number, causing the ratio $h(\tau)/R(\tau)$ to vanish in the limit $\tau \to 0$. This means that in this limit $R(\tau)$ becomes large with respect to the neck radius, elongating the profiles more and more towards the cylindrical shape close to the pinch-off, thereby justifying the assumptions made in the derivation of Eq. (5.1) in the limit $\tau \to 0$. A numerical fit gives $(\alpha_h - \alpha_R) \propto \mathrm{Fr}^{-0.14}$, which indicates that h and R have the same time dependence as $Fr \to \infty$ and, therefore, that self-similarity is recovered in this limit. A second numerical fit shows that $h_0/R_0 \propto \mathrm{Fr}^{-0.60}$, which tends to zero as $\mathrm{Fr} \to \infty$. This feature expresses the experimental observation that the initial elongation of the neck is larger for large Froude number, which effectively increases the time-interval for which the assumption of pure radial flow is valid [cf. Eq. (5.1)].

[§] At the minimum $1/R(\tau) = d^2H/dZ^2|_{Z=Z_{min}}$ and the shape of the interface can be taken to be locally parabolic, which implies $H = (\delta Z)^2/R(\tau) + h(\tau)$ with $\delta Z = Z - Z_{min}$. The scaling of the radial direction H with $h(\tau)$ then leads to the scaling $\sqrt{h(\tau)R(\tau)}$ for the axial direction Z. The aspect ratio of the void is then given by $H/Z = (h(\tau)/R(\tau))^{1/2}$.

[¶] The fact that both h and R are described by power laws suggests that we may be dealing with self-similarity of the second kind, in which the radial and axial coordinates are rescaled by different power laws of time [23]. At present there is however insufficient experimental and theoretical ground to substantiate such a claim.

5.5 Conclusion

In conclusion, our experiments on the collapse of a giant surface void are in excellent agreement with boundary integral calculations without the use of any adjustable parameter. Even when we exclude the effects of air, viscosity, and surface tension, the collapse is found to be not self-similar in a strict sense, but governed by power laws with non-universal, Froude-dependent exponents. Very near to pinch-off the void profile approaches the cylindrical shape, a regime that is approached earlier as the Froude number is larger. Self-similarity is recovered only in the limit of infinite Froude number, where the influence of gravity becomes negligible and the collapse is truly inertially driven.

References

[1] J.M. Gordillo, A. Sevilla, J. Rodriguez-Rodriguez, and C. Martinez-Bazan, *Axisymmetric bubble pinch-off at high Reynolds numbers*, Phys. Rev. Lett. **95**, 194501 (2005).

[2] A.L. Bertozzi, M.P. Brenner, T.F. Dupont, and L.P. Kadanoff, *Trends and Perspectives in Applied Mathematics*, vol. 100 (Springer, New York, 1993).

[3] M.P. Brenner, X.D. Shi, and S.R. Nagel, *Iterated instabilities during droplet fission*, Phys. Rev. Lett. **73**, 3391 (1994).

[4] H.A. Stone, *Dynamics of drop deformation and breakup in viscous fluids*, Ann. Rev. Fluid Mech. **26**, 65 (1994).

[5] P. Doshi, I. Cohen, W.W. Zhang, M. Siegel, P. Howell, O.A. Basaran, and S.R. Nagel, *Persistence of memory in drop breakup: The breakdown of universality*, Science **302**, 1185 (2003).

[6] J. Eggers, *Nonlinear dynamics and breakup of free-surface flows*, Rev. Mod. Phys. **69**, 865 (1997).

[7] R.F. Day, E.J. Hinch, and J.R. Lister, *Self-similar capillary pinchoff of an inviscid fluid*, Phys. Rev. Lett. **80**, 704 (1998).

[8] W.W. Zhang and J.R. Lister, *Similarity solutions for capillary pinch-off in fluids of differing viscosity*, Phys. Rev. Lett. **83**, 1151 (1999).

[9] I. Cohen, M.P. Brenner, J. Eggers, and S.R. Nagel, *Two fluid drop snap-off problem: experiments and theory*, Phys. Rev. Lett. **83**, 1147 (1999).

[10] M.S. Longuet-Higgins, B.R. Kerman, and K. Lunde, *The release of air bubbles from an underwater nozzle*, J. Fluid Mech. **230**, 365 (1991).

[11] H.N. Oguz and A. Prosperetti, *Dynamics of bubble growth and detachment from a needle*, J. Fluid Mech. **257**, 111 (1993).

[12] D. Leppinen and J.R. Lister, *Capillary pinch-off in inviscid fluids*, Phys. Fluids **15**, 568 (2003).

[13] R. Suryo, P. Doshi, and O.A. Basaran, *Non-self-similar, linear dynamics during pinch-off of a hollow annular jet*, Phys. Fluids **16**, 4177 (2004).

[14] J.C. Burton, R. Waldrep, and P. Taborek, *Scaling and instabilities in bubble pinch-off*, Phys. Rev. Lett. **94**, 184502 (2005).

[15] B.W. Zeff, B. Kleber, J. Fineberg, and D.P. Lathrop, *Singularity dynamics in curvature collapse and jet eruption on a fluid surface*, Nature **403**, 401 (2000).

[16] D. Lohse, R. Bergmann, R. Mikkelsen, C. Zeilstra, D. van der Meer, M. Versluis, K. van der Weele, M. van der Hoef, and H. Kuipers, *Impact on soft sand: Void collapse and jet formation*, Phys. Rev. Lett. **93**, 1980031 (2004).

[17] M.S. Plesset and A. Prosperetti, *Bubble dynamics and cavitation*, Ann. Rev. Fluid Mech. **9**, 145 (1977).

[18] Y. Hao and A. Prosperetti, *The effect of viscosity on the spherical stability of oscillating gas bubbles*, Phys. Fluids **11**, 1309 (1999).

[19] S. Hilgenfeldt, D. Lohse, and M.P. Brenner, *Phase diagrams for sonoluminescing bubbles*, Phys. Fluids **8**, 2808 (1996).

[20] G. Birkhoff and E.H. Zarantonello, *Jets, Wakes, and Cavities* (Academic Press, New York, 1957).

[21] S. Gaudet, *Numerical simulation of circular disks entering the free surface of a fluid*, Phys. Fluids **10**, 2489 (1998).

[22] A. Prosperetti, *Bubbles*, Phys. Fluids **16**, 1852 (2004).

[23] G.I. Barenblatt, *Scaling, self-similarity and intermediate asymptotics* (Cambridge University Press, Cambridge, UK, 1996).

Chapter 6

The controlled impact of a disk on a water surface: Cavity dynamics[‡]

In this chapter we study the transient surface cavity which is created by the controlled impact of a disk on a water surface. We performed boundary integral simulations and compared them to high speed recordings and particle image velocimetry measurements of the experiment. We found an excellent agreement between experiments and simulation for the interface and flow surrounding the transient cavity.

We also present a simple model for the radial dynamics of the cavity based on the collapse of an infinite cylinder. This model accounts for the observed asymmetry of the radial collapse between the expansion and contraction of the cavity. It reproduces the scaling of the closure depth and total depth of the cavity which are both found to scale roughly as $\propto Fr^{1/2}$ *with a weakly Froude number dependent prefactor. The model also accurately captures the dynamics of the minimal radius of the cavity.*

6.1 Introduction

A spectacular example of free surface flow is the impact of an object on a liquid: The impact creates a splash and a surface cavity which then collapses under the influence of hydrostatic pressure. At the singularity

---

[‡] This chapter will evolve into a manuscript: Raymond Bergmann, Stefan Gekle, Arjan van der Bos, Devaraj van der Meer, and Detlef Lohse, *The controlled impact of a disk on a water surface: Cavity dynamics*, to be submitted to J. Fluid Mech.

where the two walls of the cavity collide, two powerful jets develop, one downwards and the other one upwards to several meters high, making this fast event an impressive scene. Research into the physics of these transient surface cavities started at the beginning of the twentieth century when A.M. Worthington published his famous work "A study of splashes" [1]. His photographs revealed a wealth of phenomena of unanticipated complexity [2]. Although much has been contributed to the understanding of these phenomena, many of the intriguing questions posed by Worthington's photographs resonate still today [3, 4]. All investigations since Worthington's studies entailed experiments with a freely falling object impacting into the free surface.
To gain further insight into impact events, we built a setup in which we attach the impacting object to a linear motor. In this way we gain full control over the impact velocity, which now turns from a response observable into the key control parameter of the system.

The dynamics of a surface cavity are of enormous practical importance in many natural and industrial processes: Raindrops falling onto the ocean entrain air [5–7] and it is this mechanism which is one of the major sinks of carbon dioxide from the atmosphere. Droplet impact and the subsequent void collapse are also a significant source of underwater sound [8] and a thorough understanding is therefore crucial in sonar research. High speed water impacts and underwater cavity formation are moreover of relevance to military operations [9, 10]. In the context of industrial applications, drop impact and the subsequent void formation is crucial in pyrometallurgy [11, 12], in the food industry, and in the context of ink-jet printing [13–15]. A similar series of events as in water can even be observed when a steel ball impacts on very fine and soft sand [16–18].

Although in some of the literature the deceleration of the impacting body was minimized by choosing the properties of the body such that the velocity of the impactor remained roughly constant during the time the cavity dynamics were observed [19, 20], the velocity of the body nevertheless remained a response parameter set by the system. We use a linear motor to accurately control the position, velocity, and acceleration of the impacting object, which constitutes the key difference between our work (see also [21, 22]) and all previous ones.

In this article, we will use observations from experiments and boundary integral simulations to construct a model which accurately describes the radial dynamics of the cavity.

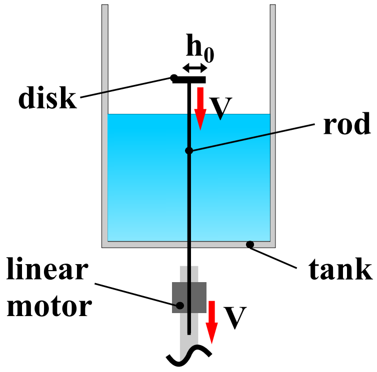

Figure 6.1: Schematic figure of the experimental setup with the linear motor controlling the rod and disk. The vertical rod runs through a seal in the bottom of the glass water tank and is pulled down by the linear motor in order to impact the disk on the water surface.

We will start in Section 6.2 by comparing our controlled experiment to the boundary integral simulations. Starting in Section 6.2.1 with the dynamics of the free surface, while in Section 6.2.2 the topology and magnitude of the flow surrounding the cavity obtained by particle image velocimetry will be compared to the simulations.
In Section 6.3 we will derive a model which captures the radial dynamics of the cavity and use it to derive the following key characteristics of the transient surface cavity: The depth at which the pinch-off will occur is discussed in Section 6.3.1. In Section 6.3.2 the influence of the flow on the asymmetry between the radial expansion and collapse of the cavity is examined. The amount of air entrained by the cavity collapse is studied in Section 6.3.3. In the last two sections the dynamics of the minimal void radius is studied (Section 6.3.4) and the cavity shape around this minimal radius ar discussed (Section 6.3.5).

6.2 Experimental and numerical results

A sketch of the setup is seen in Fig. 6.1. A disk of radius h_0 is mounted on top of a thin rod (∅ 6 mm). This rod runs through a seal in the bottom of a large tank (500 mm×500 mm×700 mm) and is connected at the lower end to a Thrusttube linear motor which is used to determine and control the velocity and acceleration of the object. The position of the motor along the vertical axis is measured with a spatial accuracy of 5 μm over a range of 1 m, the large acceleration of the motor (up to 30 g) makes it possible to perform impact experiments with constant velocities up to 5 m/s.

The effect of the small diameter of the rod on the global flow and dynamics of the cavity is assumed to be negligible. As the minimum radius for the disk used in the experiments is 10 mm, the ratio of the cross–sectional area of the rod and the surface of the disk is always smaller than 9%. Since the rod is mounted in the center of the disk, where stagnation would normally occur, the influence on the radially outward flow below the disk is small.

Using the flat plate approximation, we can also estimate the direct contribution of the boundary layer of the rod to the axial flow. The boundary layer thickness δ for a flat plate is given by Blasius' solution of $\delta = 5\sqrt{\nu t_{dev}}$, where ν is the kinematic viscosity of water and t_{dev} the time the boundary layer has to develop. We will equate the time t_{dev} to the duration of the experiment, namely to the time from the impact of the disk until the collapse of the void, which in experiments [19] was found to be equal to $t_{dev} \approx 2.3\sqrt{h_0/g}$, where g is the gravitational acceleration. In the worst case, for the largest disk size in the experiment $h_0 = 40$ mm, this boundary layer will be 1.8 mm and considerably thinner under most experimental conditions.

In our experiments we pull the disk down with a *constant* velocity V. Making this main control parameter dimensionless, we obtain the Froude number $\mathrm{Fr} = V^2/(gh_0)$. The liquid properties are expressed in terms of the Reynolds number $\mathrm{Re} = Vh_0/\nu$ and the Weber number $\mathrm{We} = \rho V^2 h_0/\sigma$, where σ denotes the surface tension and ρ the fluid density. Since the Reynolds number and the Weber number are considerable on the large scales of Fig. 6.1, the viscosity and the surface tension do not seem to play a role. In our experiment the Reynolds number ranges between 500 and $1.6 \cdot 10^4$ and the Weber number ranges between 34 and $8.8 \cdot 10^3$. However, note that under only slightly different conditions, namely replacing the disk by a cylinder emerged in water to avoid the splash, capillary waves *do* play a role, (see [22]). But, since this is not the case here, the only important dimensionless parameter is the Froude number, e.g., the ratio of kinetic to gravitational energy, which ranges from 0.6 to 200.

The numerical calculations are performed with a boundary integral method to solve the flow potential in the bulk. The potential flow assumption excludes viscous effects and vorticity, which due to the short duration of the phenomenon and the high Reynolds number seems reasonable.

6.2.1 Interface

The series of events typical for the experimental range of $1 < \mathrm{Fr} < 100$ is seen in the snapshots of Fig. 6.2a, b, and c. Upon impact a splash, an outward moving crown of water, is formed. A void is created which collapses due to the hydrostatic pressure and a singularity arises when the collapsing walls of the void collide with each other. Two jets emerge in this experiment: One upwards straight into the air, and one downwards into the entrained air bubble.

In the first two sequences for Fr=0.85 and Fr=3.4 (Figs. 6.2a and b), the cavity dynamics is found to be captured extremely well by the numerical result, represented by the overlaid lines. Note that this is a one to one comparison, without any rescaling in time or space. Due to the axisymmetry of the code it is not possible to capture the full details of the splash and therefore we chose to take out any droplets which are released from the splash. Surface tension however still expresses itself in small capillary waves in the region of the splash, these waves are most notable in Fig. 6.2a. As was mentioned before, it is these waves which are found to have a significant influence on the closure of the cavity for the emerging of a cylinder [22], however in the present regime discussed in this paper for the impacting disk, these waves do not affect the closure.

In Chapter 5 we previously presented similar results for the comparison between the experiment of the impact of a disk and the boundary integral simulations at a Froude number of 3.4. Here, we also include the results for Fr=0.85 in Fig. 6.2a, to illustrate the effect of the increased significance of gravity. In the last frame of Fig. 6.2a it can be seen that the cavity is less symmetric in axial direction around the closure point compared to the experiment performed at Fr=3.4. In Fig. 6.2c we also present impact experiments which go beyond the Froude number range described in Chapter 5.

For this third sequence at Fr=13.6 (Fig. 6.2c) significant deviations between the experiment and the numerical cavity shape are found, most notably in the enlargement of Fig. 6.3 at the depth of the cavity closure. The closure of the cavity is found to be somewhat deeper in the numerics as compared to the experiments. This deviation can be attributed to a secondary effect due to the surrounding air, called the *surface seal*. This phenomenon was first reported by Worthington [1] and is shown in detail in Fig. 6.4. Note that the impact experiment of Fig. 6.4 is performed under the same conditions as Fig. 6.2c. The surface seal is the entrainment of the initially outward moving splash by the air rushing into the expanding cavity. If the airflow is strong enough, the splash will close on the axis of symmetry and completely seal off the top of the cavity above the height of the undisturbed water surface.

The surface seal is found to become more pronounced at higher impact velocity, where the surface seal occurs earlier and more liquid is involved in this closure. Accordingly there is also a larger influence on the shape of the cavity at higher impact velocity. Since this chapter aims to treat the purely pressure driven collapse of the cavity, without the contributions of the surrounding air, our experimental range is limited by the occurrence of the surface seal. In the simulations we therefore intentionally do not include the air. This explains the discrepancy of Fig. 6.2c (enlarged in Fig. 6.3), since contrary to the experiments, no surface seal occurs in the numerics due to the absence of air. In Fig. 6.2d we go far beyond the experimentally available range by performing simulations at a Froude number of 200.

It is instructive to compare the present boundary integral simulation results with the one reported by Gaudet [20], who reported a bulging contraction of the cavity at the surface level, which he found to close for $\mathrm{Fr} \geq 200$ and interpreted as a surface seal in the absence of air. We found no evidence for such a surface seal in our simulations, even for considerably larger Froude numbers, and surmise that the effect reported by the author of [20] may be connected to using an insufficient number of nodes in the splash region caused by the limited amount of computational power available at that time.

6.2.2 Flow field

In the previous section we find the experimental shape of the impact cavity to be well described by our boundary integral simulations if no surface seal occurs. The question we will pose ourselves in this section is whether the simulations also give an accurate description of the surrounding flow field. To this end we will measure the velocity field around the transient cavity through high speed particle image velocimetry (PIV). These experiments are crucial to check the validity of the boundary integral simulations, as the presence of a solid boundary, namely the impacting object, will induce vorticity in the flow. We will then compare this flow field to the boundary integral results, and finally investigate the radial flow at the depth of closure.

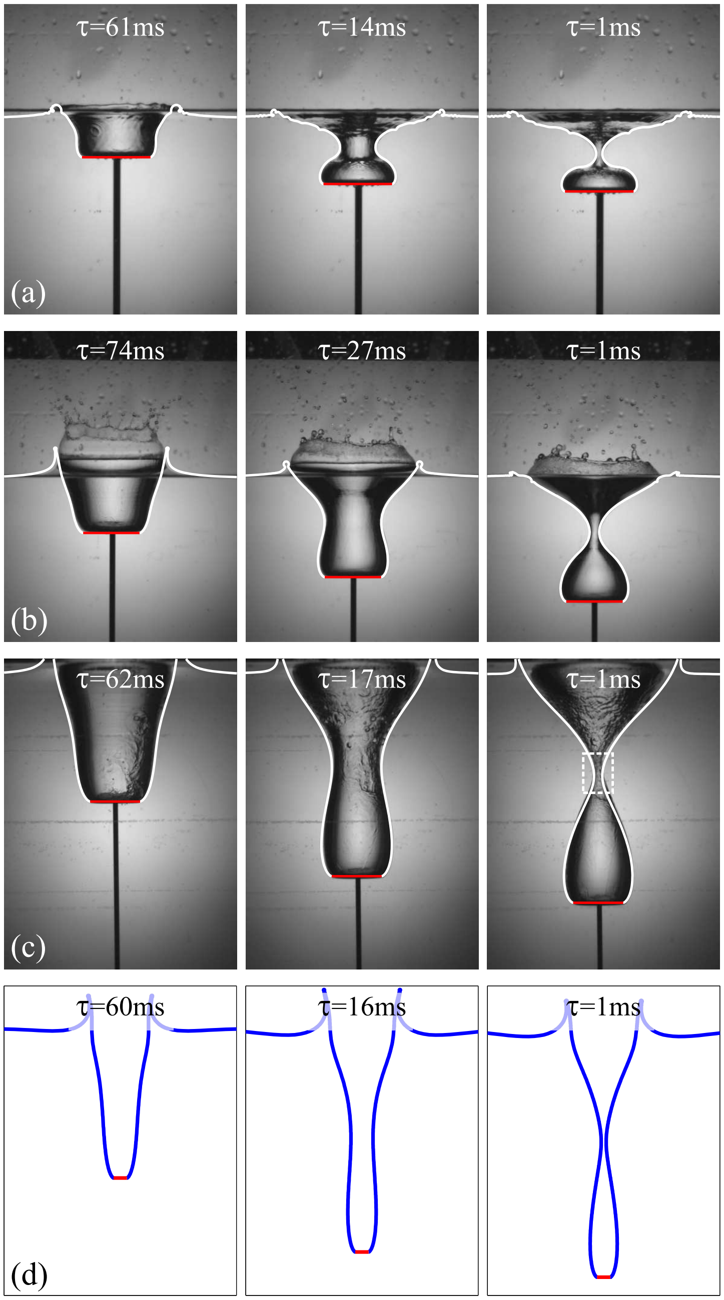

Figure 6.2: Snapshots of the formation and collapse of a surface void in the plunger experiment: A linear motor pulls down a disk of radius $h_0 = 30$ mm through the water surface at a constant velocity (a) $V = 0.5$ m/s (Fr = 0.85); (b) $V = 1.0$ m/s (Fr = 3.4); (c) $V = 2.0$ m/s (Fr = 13.6); and (d) Fr = 200. The collapse of the void is imaged at a 1000 frames per second. The lines (overlay) are the void profiles obtained from boundary integral simulations. Without the use of any free parameter an excellent agreement between the simulation and experiment is found in (a) and (b). Due to a surface seal there is a discrepancy between the simulations and the experiment in sequence (c). The region of the dashed box is shown enlarged in Fig. 6.3. The surface seal is aggravated at higher Froude number, so for (d) no experimental data can be obtained.

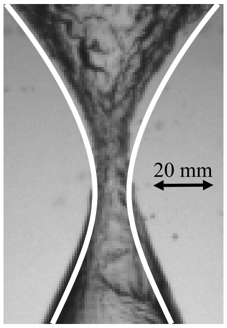

Figure 6.3: Enlargement of the region around the pinch off point at $\tau = 1$ ms from the sequence Fig. 6.2c (Fr = 13.6). A significant discrepancy can be seen for the depth of the pinch–off between the boundary integral simulation (white line) and the experimental recording.

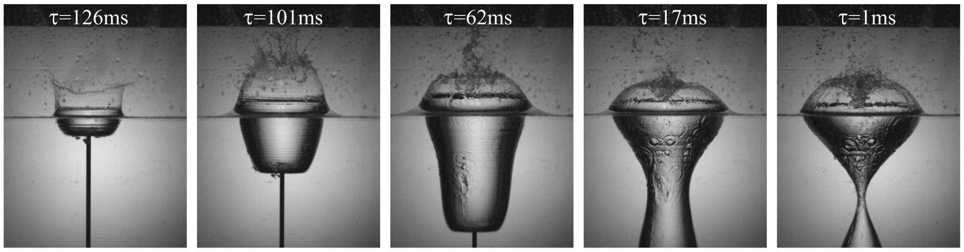

Figure 6.4: Snapshots of the surface seal which occurs for a disk of radius $h_0 = 30$ mm impacting the water surface at a constant velocity of $V = 2.0$ m/s (Fr = 13.6). The collapse of the void is imaged at a 1000 frames per second.

To perform the PIV measurements, the fluid is seeded with small DANTEC Dynamics polyamid tracer particles of radius 25 μm and density 1030 kg/m^3 which will follow the flow. A laser sheet shines from the side through the fluid, creating an illuminated plane. The light scattered by the particles is captured by a high speed camera at a frame rate of 6000 frames per second and a resolution of 1024x512 pixels. The series of recorded images is then correlated by multipass algorithms, using DaVis PIV software by LaVision, in order to determine the flow field in a plane in the liquid. The correlation was performed in two passes at sub-pixel accuracy, using 64×64 pixels and 32×32 pixels interrogation windows. The windows overlap by 50%, resulting in one velocity vector every 16×16 pixels.

In order to obtain high resolution PIV measurements of the flow around the cavity, we made use of the perfect reproducibility of the experiment. The left side of each of the images of Fig. 6.5 shows the flow around the expanding void by combining the results of four separate PIV measurements at different depths. In this fashion PIV experiments were performed at 6000 fps for a field of view of 96×56 mm at a spatial resolution of 0.9 mm. In Fig. 6.5 only 0.7% of the measured vector field is shown. This high resolution makes it possible to simultaneously compare the global flow, as well as the smaller flow structures at the pinch–off depth and the disk's edge.

To compare the experimental flow field to the flow in the simulation, the right side of each image of Fig. 6.5 shows the numerically obtained cavity profile and flow field. There appears to be a good agreement, but one would want a more quantitative comparison between the experimental and numerical flow field. This is provided in Fig. 6.6, which shows contour plots of the axial flow component (Fig. 6.6a-d) and the radial flow component (Fig. 6.6e-f) obtained from the PIV measurements (at the left side of each image) and boundary integral simulations (at the the right side of each image). From this figure it is clear that the magnitude as well as the topology of the flow are in excellent agreement. Figures 6.5 and 6.6 are a one–to–one comparison between simulation and experiment, and we stress once more, without the use of any free parameter.

The experimental pictures of Fig. 6.6 reveal that our initial assumption of Section 6.2, namely to neglect the influence of the rod on the flow, is correct. The rod is clearly visible in the experimental snapshot Fig. 6.5a and its downward movement has been detected by the PIV software in Fig. 6.6a. The flow however is unaffected outside the region occupied by the rod. The boundary layer of the rod therefore has no significant contribution to the flow around the cavity. Also, the outward flow at the edges of the disk in Fig. 6.6e is unaffected by the rod. As can be seen in this figure, the radial flow decays quickly towards the center of the disk, so the presence of the rod does not change the topology or magnitude of the flow at the edge of the disk. This is an important observation as the outward flow below the disk is responsible for the expansion of the void.

The experimental flow up to 7 disk radii in radial direction at the closure depth is compared with numerics in Fig. 6.7. Fig. 6.7 gives an indication of the magnitude of the deviations between the numerical and experimental flow field. Typically, this deviation is of the order of 0.01 m/s, but it can be slightly larger if the flow velocity is small. The larger inaccuracy at

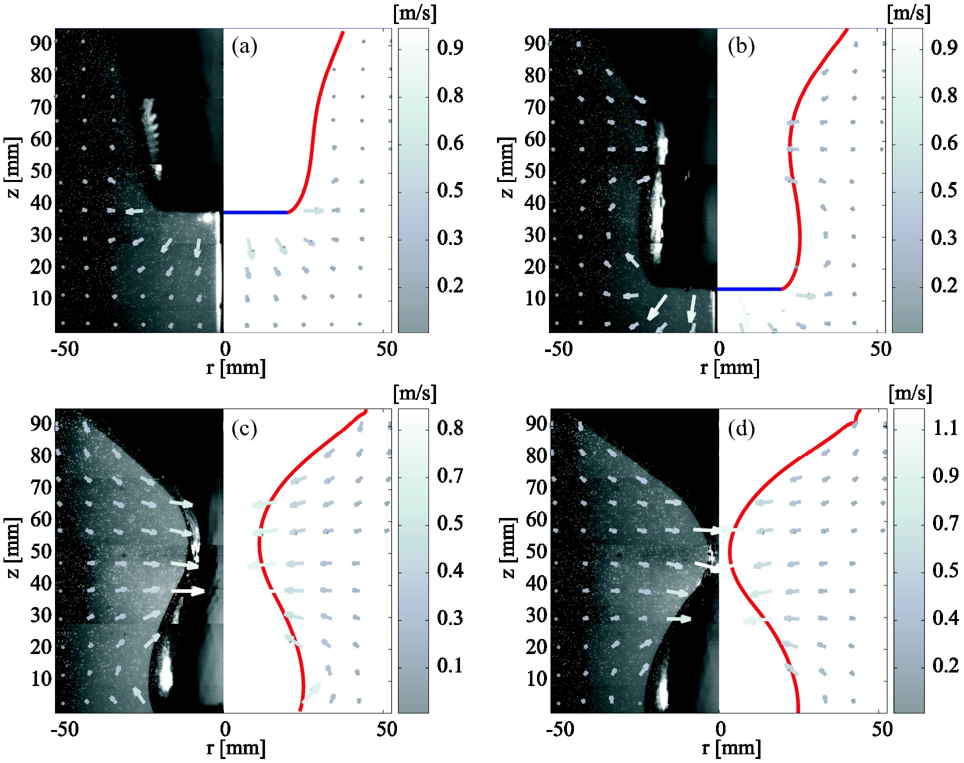

Figure 6.5: The flow field obtained from experiments and boundary integral simulations for a disk of radius $h_{disk} = 20$ mm which impacts with a velocity of $V = 1.0$ m/s (Fr = 5.1). The figures show the flow field at $\tau =$ (a) 49 ms; (b) 25 ms; (c) 7 ms; and (d) 1 ms. The left side of each image shows the flow field (overlaid vectors) obtained from the experiment by four highspeed PIV recordings at 6000 frames per second. The four different recordings were taken at different depths and combined to give the flow field in the experiment at high resolution. The recordings on the left side of each image show the degree of reproducibility of the experiment, as the match between the four recordings at different depth is perfect. For clarity only 0.7% of the vectors is shown. The right side of each of the images shows the void profile and the corresponding flow field (overlaid vectors) obtained from the boundary integral calculations.

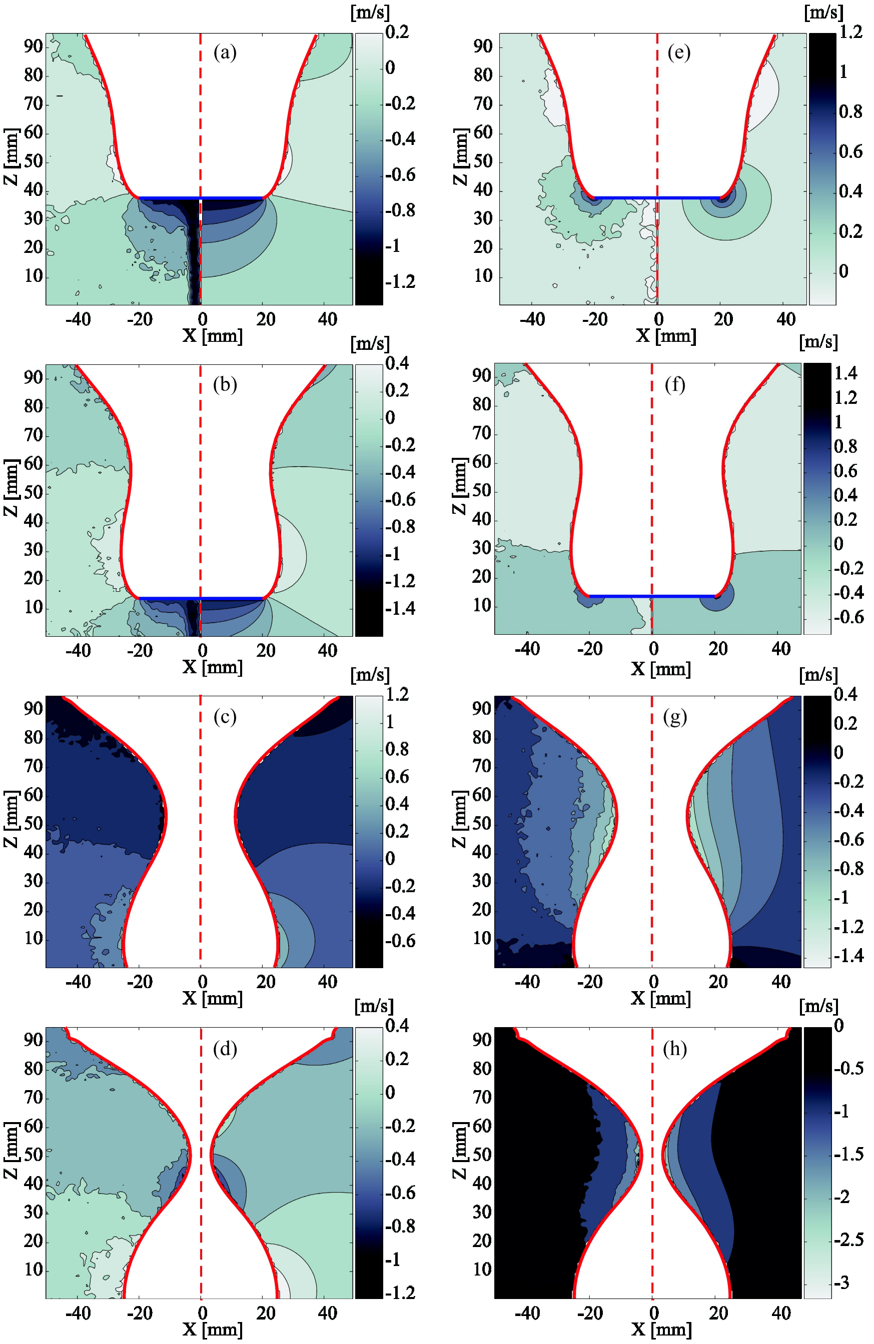

Figure 6.6: The axial (left) and radial (right) components of the flow fields of Fig. 6.5. The four images to the left (a-d) show a contour plot of the *axial* flow component from the experiment (left side of each image) and numerics (right side of each image), the four images on the right (e-h) show a similar contour plot of the *radial* flow component from the experiment (left side of each image) and numerics (right side of each image). Apart from the region where the rod is pulling down the disk in the experiment, which is absent in the simulation, both components of the flow field show excellent agreement between the experiments and numerical calculations.

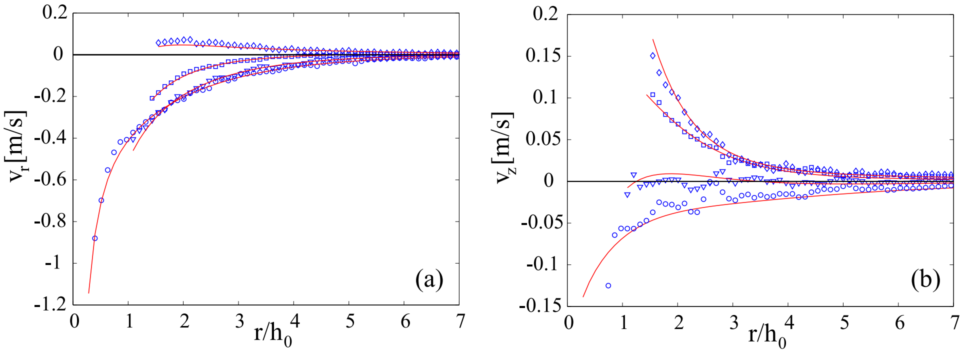

Figure 6.7: This figure shows the radial (a) and axial (b) component of the flow at the depth of the closure z_{coll} for a disk of a radius of $h_{disk} = 10$ mm which impacts at a velocity of $V = 1.0$ m/s (Fr = 10.2). The symbols show the result obtained from the PIV measurements at different times, respectively $\Diamond : \tau = 30.5$ ms; $\square : \tau = 20.5$ ms; $\nabla : \tau = 10.5$ ms; and O: $\tau = 0.5$ ms, and the solid red line is the equivalent numerical result from the BI simulation. The PIV data is an average of 6 subsequent measurements obtained from the high speed PIV recordings at 6000 frames per second. The v_r and v_z velocity components shown here are thus the average over one millisecond.

low flow velocities is generic to the PIV method and can be seen to occur for $\tau = 10.5$ ms in Fig. 6.7b, but overall an excellent agreement is found between the far field flow in the numerics and experiments.

In the numerics and simulation of Fig. 6.7a it can be seen that during the expansion of the void the outward radial flow falls off with the distance to the symmetry axis. However, when the cavity starts to collapse inward, the flow is reversed and the radial flow component is seen to cross the x-axis for $\tau = 20.5$ ms. At this time there is a plane where the radial flow vanishes. There is however no reversal of the axial flow direction at the closure depth as can be seen in Fig. 6.7b, so it should not be understood as a stagnation point of the flow.

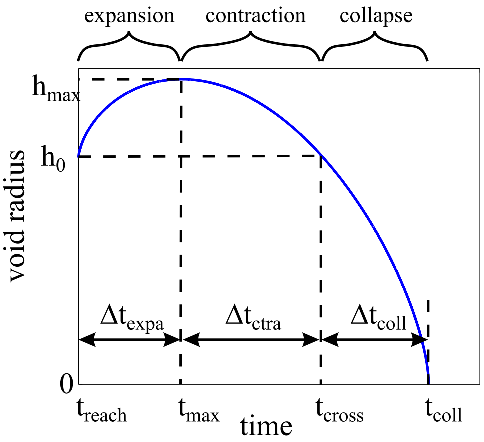

Figure 6.8: Schematic representation of the three regimes for the radial dynamics of the cavity at a constant depth z. The first two regimes during a time $\Delta t_{expa}+\Delta t_{ctra}$ are governed by the hydrostatic pressure. These regimes consist of an expansion and contraction phase for which h_∞ differs considerably. In the third regime during a time Δt_{coll}, the collapse accelerates towards the singularity and continuity takes over as the dominant factor.

6.3 Model

In the upcoming sections we will first derive a simple model for the radial dynamics of the transient cavity. This model will then be applied to investigate the following key characteristics of the transient cavity:

- The depth of the pinch-off and the depth of the disk at the moment of pinch–off (Section 6.3.1).
- The role of the flow in the asymmetry between the radial expansion and collapse of the cavity (Section 6.3.2).
- The amount of air entrained by the cavity collapse (Section 6.3.3).
- The dynamics of the minimal cavity radius (Section 6.3.4).
- The cavity shape around the minimal radius (Section 6.3.5).

6.3.1 Closure depth

Following [19], [20], and [10] we will characterize the shape of the cavity at pinch–off by the depth of closure z_{coll}, i.e., the depth at which the pinch–off takes place. To capture more information on the full shape of the void, we will also investigate how z_{coll} relates to the total depth of the cavity $z_{disk}(t_{coll}) = z_{disk,\,coll}$ at the time of collapse (or closure) t_{coll}.

A comprehensive argument for the scaling of z_{coll} can be obtained by following the same procedure as outlined in Chapter 2 for the determination of the closure depth after the impact of a steel ball on soft sand. However, now the medium is incompressible and the outward expansion of the cavity should be taken into account. The argument starts by writing the two-dimensional Rayleigh-type equation for the void radius at a fixed depth [17, 23],

$$\left[\frac{d(h\dot{h})}{dt}\right]\log\frac{h}{h_\infty}+\frac{1}{2}\dot{h}^2=-gz\,. \tag{6.1}$$

The pressure difference driving the collapse of the cavity with radius h has been equated to $-\rho g z$, where z denotes the depth below the fluid surface. The quantity h_∞ is the length scale related to the matching of the inner and outer flow regions. In the region near the neck the induced flow looks like a collapsing cylinder as described by Eq. (6.1), whereas in the region far from the neck, the flow resembles a sink (plus its image at the free surface). A complete description of the flow would require the matching of these two regions, where h_∞ would be determined in the process as the cross–over length scale. h_∞ would thus be expected to be of the order of a typical length scale of the process, such as the distance of the cavity surface to the plane where the radial flow vanishes (cf. Fig. 6.7a). Therefore, strictly speaking, h_∞ is a function of time and of the Froude number. In the model description we will set h_∞ to a constant, which resembles the time average of its dynamics. In Eq. (6.1) it is assumed that the system is composed of non-interacting horizontal layers of fluid, with a negligible vertical velocity component.

We can use Eq. (6.1) to analyze the radial dynamics from the initial impact of the disk t_0 to the time of closure of the cavity t_{coll} at arbitrary depth z. Time intervals are denoted with Δt, whereas the previously used τ denotes the absolute time left till the collapse ($\tau = t_{coll} - t$). The time interval between impact and collapse $\Delta t = t_{coll} - t_0$ consists of two main parts: First, the disk has to reach the depth z. Second, there is the time it takes for the void to form, expand, and collapse,

$$\Delta t = \Delta t_{reach} + \Delta t_{void}\,. \tag{6.2}$$

The first term can easily be given since the velocity is constant in the experiment and simulation and therefore it equals $\Delta t_{reach} = z/V$. The void expansion and collapse time Δt_{void} can in turn be decomposed into three regimes as is schematically depicted in Fig. 6.8. The first two regimes are the expansion of the void, and the process where the expansion is slowed down by hydrostatic pressure and reversed into a shrinking of the void. In both of these regimes, the hydrostatic pressure is the dominant factor, but they are dissimilar, since the surrounding flow is dissimilar. In the expansion phase the outward radial flow simply decays with the radial distance, whereas in the contraction phase the radial flow vanishes at a finite distance (see Fig. 6.7). The third regime is where the collapse accelerates towards the singularity, and continuity takes over as the dominant factor. So we can write for the collapse time as (see Fig. 6.8),

$$\Delta t = \Delta t_{reach} + \underbrace{\Delta t_{expa} + \Delta t_{ctra} + \Delta t_{coll}}_{\Delta t_{void}} \,. \tag{6.3}$$

To estimate these last three timescales, we turn to Eq. (6.1). For the regimes dominated by the hydrostatic pressure, we observe that the water is first pushed aside by the passing disk, creating an expanding void. At the maximum radius h_{max}, the expansion is halted and the void starts to contract. Since $\dot{h}(t_{max}) = 0$, we can assume that $\dot{h}(t)$ is small during the expansion and contraction phase and neglect the second term in Eq. (6.1),

$$\left[\frac{d(h\dot{h})}{dt}\right] \log\frac{h}{h_\infty} = -gz \,. \tag{6.4}$$

Since $\log(h/h_\infty)$ varies very slowly in these regimes, we equate $\log(h/h_\infty) \approx \log(h(t_{max})/h_\infty)$ and we can solve Eq. (6.4) using $h(t_{max}) = h_{max}$ and $\dot{h}(t_{max}) = 0$, leading to a parabolic approximation,

$$h^2(z,t) = h_{max}^2 - \frac{gz}{\beta}(t - t_{max})^2 \,, \tag{6.5}$$

with $\beta = \log(h_{max}/h_\infty)$. The above equation holds for both the expansion phase, the time it takes for the void to grow from h_0 to h_{max}, and the contraction phase, the time it takes to shrink back to h_0. As was mentioned before the flow around the cavity is different in both phases, resulting in different values of h_∞ for both. So during the expansion we take $\beta_{expa} = \log(h_{max}(z)/h_\infty^{expa})$ and during the contraction we take $\beta_{ctra} = \log(h_{max}(z)/h_\infty^{ctra})$. h_∞^{expa} and h_∞^{ctra} are set to a constant value, which represents the time averaged behavior of h_∞ in the respective phase.

To find h_{max}, or the time it will take to get there from the time the disk passes at $t = t_{reach}$, we need the radial velocity of the initial expansion at $t = t_{reach}$ (see Fig. 6.8). A reasonable assumption is that the disk displaces water from underneath itself to the sides at a velocity directly proportional to its travelling velocity. Therefore, we will use $\dot{h}(t_{reach}) = \alpha_{expa}V$. For the velocity at the end of the contraction phase at $t_{cross} = t_{reach}+\Delta t_{expa}+\Delta t_{ctra}$, we write in a similar fashion $\dot{h}(t_{cross}) = -\alpha_{ctra}V$. Of course, for given α_{expa}, β_{expa}, and β_{ctra}, the constant α_{ctra} is uniquely determined by the continuity of the trajectory and its derivative, which gives $\alpha_{ctra} = \alpha_{expa}\sqrt{\beta_{expa}/\beta_{ctra}}$. If we combine these two boundary conditions with the time derivative of Eq. (6.5), we obtain

$$\Delta t_{expa} + \Delta t_{ctra} = (\alpha_{expa}\beta_{expa} + \alpha_{ctra}\beta_{ctra})\frac{h_0 V}{gz}\,. \tag{6.6}$$

The third regime, where continuity becomes dominant, can also be analyzed using Eq. (6.1). Near the collapse, h approaches zero, and the logarithm diverges. The only way Eq. (6.1) can remain valid is when the prefactor of the logarithm vanishes. This means that

$$\frac{d(h\dot{h})}{dt} = \frac{1}{2}\frac{d^2\left(h^2\right)}{dt^2} = 0\,. \tag{6.7}$$

Integration gives the power law of the two dimensional Rayleigh collapse,

$$h(t) = \sqrt{C}(t_{coll} - t)^{1/2}\,. \tag{6.8}$$

The value of C follows from the fact that the trajectory in Fig. 6.8 and its derivative should be continuous. We assume the collapse regime to start at the end of the contraction phase (Fig. 6.8), where we have $h(t_{cross}) = h_0$ and $\dot{h}(t_{cross}) = -\alpha_{ctra}V$. From these conditions, the value of C can be obtained,

$$C = 2h_0\alpha_{ctra}V\,. \tag{6.9}$$

The estimate for Δt_{coll} follows from $h(t_{cross}) = h_0$ and thus we find,

$$\Delta t_{coll} = t_{coll} - t_{cross} = \frac{1}{2\alpha_{ctra}}\frac{h_0}{V}\,. \tag{6.10}$$

Collecting all the time scales, the total amount of time that passed from the impact of the disk until the collapse of the cavity at depth z is estimated by

$$\begin{aligned}\Delta t &= \Delta t_{reach} + \Delta t_{expa} + \Delta t_{ctra} + \Delta t_{coll} \\ &= \frac{z}{V} + (\alpha_{expa}\beta_{expa} + \alpha_{ctra}\beta_{ctra})\frac{h_0 V}{gz} + \frac{1}{2\alpha_{ctra}}\frac{h_0}{V}\,. \end{aligned} \tag{6.11}$$

Now, to find the closure depth z_{coll}, we need to determine where the collapse will occur first, which we can do by solving

$$\frac{d\Delta t}{dz} = 0\,. \tag{6.12}$$

This gives,

$$\frac{z_{coll}}{h_0} = \sqrt{\alpha_{expa}\beta_{expa} + \alpha_{ctra}\beta_{ctra}}\mathrm{Fr}^{1/2}\,. \tag{6.13}$$

In addition, the total depth of the disk at the time of collapse, $z_{disk}(t_{coll}) = z_{disk,\,coll}$, can be obtained by plugging Eq. (6.13) into Eq. (6.11) to solve $z_{disk,\,coll} = V\Delta t$,

$$\frac{z_{disk,\,coll}}{h_0} = 2\sqrt{\alpha_{expa}\beta_{expa} + \alpha_{ctra}\beta_{ctra}}\mathrm{Fr}^{1/2} + \frac{1}{2\alpha_{ctra}}\,. \tag{6.14}$$

From Fig. 6.9a it is clear that we find good agreement of the experiments without a surface seal (blue symbols) and the numerical calculations (black circles), with the prediction of $z_{coll}/h_0 = \theta\mathrm{Fr}^{1/2}$, with $\theta = 1.10$ obtained from a fit to the data of z_{coll}. The agreement between experiments in which a surface seal occurs (red symbols) and the simulations for a fixed disk size deteriorates with increasing Froude number, since the surface seal becomes more disruptive for higher impact velocity.
In the same figure we find, from a fit to the total depth $z_{disk,\,coll}$, that the constant factor $1/(2\alpha)$ in Eq. (6.14) has no significant contribution. The total depth of the void is found to scale as $z_{disk,\,coll}/h_0 = \eta\mathrm{Fr}^{1/2}$, with $\eta = 2.49$ close to the prediction of $\eta = 2\theta = 2.2$. The Froude scaling of the total depth indicates that the time from the initial impact of the disk to the time of closure of the cavity does not depend on the velocity of the impact, since $\Delta t = z_{disk,\,coll}/V = \eta\sqrt{h_0/g}$.

Note that the $\mathrm{Fr}^{1/2}$ scaling is independent of the individual values that the parameters α_{expa}, β_{expa}, α_{ctra}, and β_{ctra} take. From the experimental and numerical data we find

$$\alpha_{expa}\beta_{expa} + \alpha_{ctra}\beta_{ctra} \approx 1.10^2 \approx 1.21\,. \tag{6.15}$$

Together with

$$\alpha_{ctra} = \alpha_{expa}\sqrt{\beta_{expa}/\beta_{ctra}}\,, \tag{6.16}$$

this effectively reduces the number of free parameters to two, namely α_{expa} and β_{expa}. The parameters α_{expa} and h_∞^{expa} (and thus β_{expa}) could in

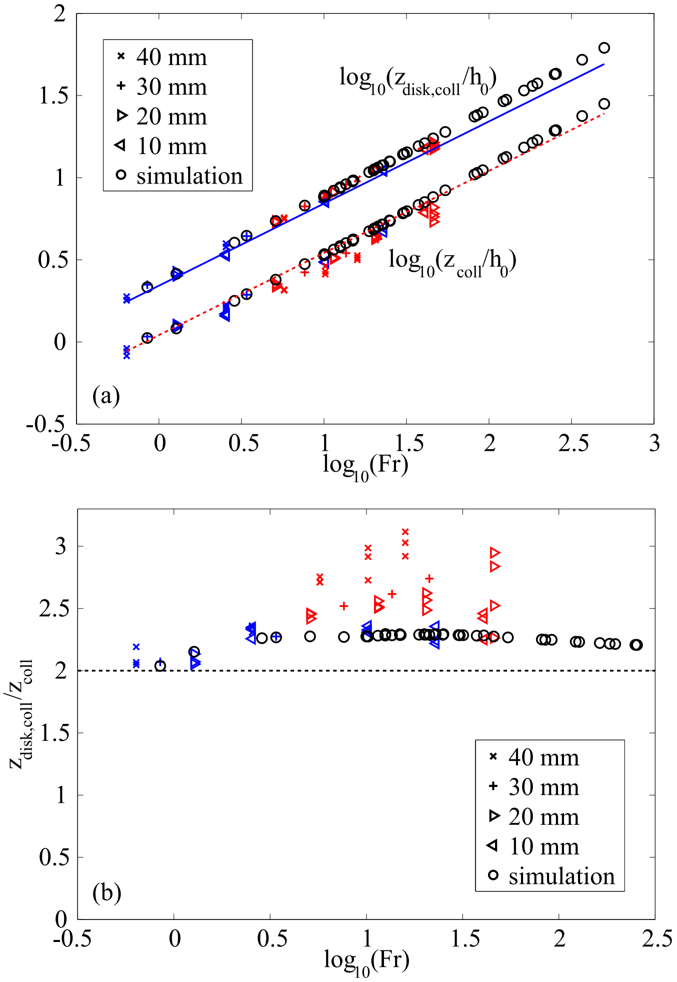

Figure 6.9: (a) The depth for the collapse of the void z_{coll} and the depth of the disk at the time of collapse $z_{disk,\,coll}$ for experiments with different disk radii as a function of the Froude number and for the boundary integral simulations (open circles). Experiments in which a surface seal occurs during the collapse are indicated by red symbols, the experiments without a surface seal by blue symbols. The experiments without a surface seal are found to agree well with the numerically obtained values (open circles) and the theoretical prediction for the scaling of $z_{coll}/h_0 = \theta Fr^{1/2}$ (red dashed line) and $z_{disk,\,coll}/h_0 = 2\theta Fr^{1/2}$ (blue solid line), with $\theta = 1.10$ obtained from a fit to the data of z_{coll}. The experiments for which a surface seal occurs are seen to slightly deviate from this prediction.
(b) The ratio of the depth of the disk at the time of pinch-off $z_{disk,\,coll}$ and the pinch-off depth z_{coll} for different disk radii as a function of the Froude number. The experiments without a surface seal (blue symbols) agree well with the numerical result (open circles). The ratio for the numerical result and experiments without a surface seal is close to the predicted value of 2 indicated by the black dashed line. The experiments in which a surface seal occurs are again indicated by the red symbols and found to deviate more with increasing Froude number for a fixed disk size.

principle weakly depend upon z, which would lead to slight modifications in the result of Eqs. (6.13) and (6.14).

To investigate the data of Fig. 6.9 (a) more closely it is convenient to take the ratio of $z_{coll}/z_{disk,\,coll}$ (see Fig. 6.9 (b)). According to Eq. (6.13) and Eq. (6.14), this ratio should scale as

$$z_{coll}/z_{disk,\,coll} = 2 + \frac{1}{2\alpha_{ctra}\sqrt{\alpha_{expa}\beta_{expa} + \alpha_{ctra}\beta_{ctra}}}\mathrm{Fr}^{-1/2} \approx 2\,. \quad (6.17)$$

In Fig. 6.9b the ratio of $z_{coll}/z_{disk,\,coll}$ in the experiments without a surface seal (blue symbols) and the numerical calculations (black circles) are indeed close to the constant value of 2 (dashed black line), but at lower Froude number it decreases slightly in contrary to the proposed scaling by the second term in Eq. (6.17). This is due to the fact, that the second term of the ratio (Eq. (6.17)) only becomes relevant when the Froude number is considerably small. In this limit however also our assumption of non-interacting fluid layers from Eq. (6.1) breaks down as gravity becomes more important and Eq. (6.17) is no longer valid. In Fig. 6.9b it is again nicely illustrated that the experiments with a surface seal (red symbols) deviate more and more from the simulations without air as the Froude number increases.

6.3.2 The influence of the flow on the cavity dynamics at closure depth

In the previous section we find that the Rayleigh type model accurately reproduces key aspects of the cavity shape at pinch–off, namely the closure and total depth of the cavity. The question we will pose ourselves in this section is whether the Rayleigh equation also gives an accurate description of the cavity during the collapse. For this we will investigate the radial dynamics of the cavity at the depth of closure. In particular we will relate these dynamics at closure depth to the structure of the surrounding flow. So we will start by investigating the surrounding flow and use these observations to match the model of the radial collapse to the dynamics observed in the simulation.

From Fig. 6.7a it was clear that during the expansion of the void the outward radial flow falls off with the distance to the symmetry axis. However, when the cavity starts to collapse inward, the flow is reversed and the radial flow component is seen to cross the x-axis for $\tau = 20.5$ ms, so at this time there is a plane where the radial flow vanishes. There is however no reversal of the axial flow direction at the closure depth as can be seen in Fig. 6.7b.

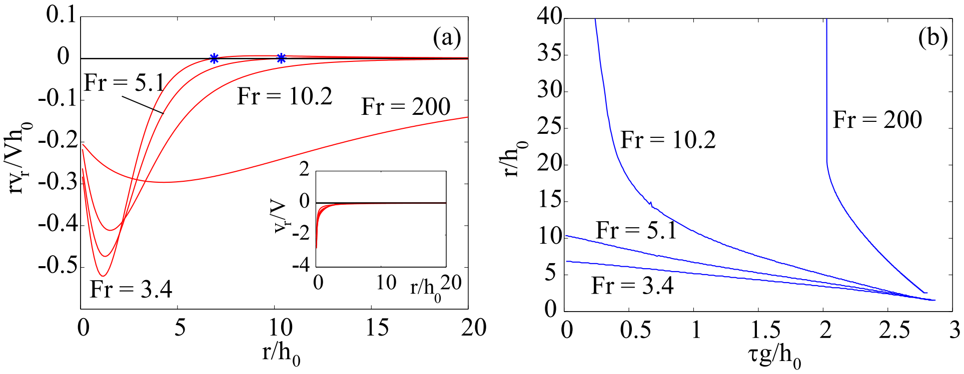

Figure 6.10: (a) The radial velocity component v_r at the moment and depth of closure multiplied by the radial distance r as a function of the same radial distance for different Froude numbers. The inset shows the original radial velocity data. The distance where the radial velocity is zero and the flow is stagnated in radial direction is indicated by the blue stars. The flow can be seen to resemble more of a radial sink flow with increasing Froude number as the minimum of $v_r r$ can be seen to decrease with increasing Froude number. (b) The distance of the point where the radial flow reverses sign to the symmetry axis, determined at the depth of closure as a function of the time remaining till closure $\tau = t_{coll} - t$. Below the curves the flow is directed inwards, above them it is directed outwards. The distances of the flow reversal point at $\tau = 0$ from this figure correspond to the blue stars of figure (a). The distance of the point of flow reversal is directly related to the length scale h_∞^{ctra} and h_∞^{expa} is expected to show similar dynamics with time.

The axial flow however does change sign at a different depth, as must be the case since a down flow in the upper region of the liquid and an up flow in the lower region is observed in Fig. 6.6. There must therefore be a stagnation point (or saddle point) in the (r,z)-plane, corresponding to a circle in three dimensions where both the axial and the radial velocity components change sign. To investigate the dynamics of this stagnation point, we turn to the simulations as they can have an arbitrary fine resolution of the flow field.

Fig. 6.10a shows the radial flow component multiplied by the radial distance to the axis of symmetry at the depth and moment of pinch-off. The radial flow component v_r is multiplied by the radial distance r for convenience. The flow at the neck will locally resemble a two dimensional sink, who's strength will fall off with $1/r$. Therefore multiplying v_r with r eliminates this geometrical contribution to the flow.

In Fig. 6.10a the lower Froude numbers of 3.4 and 5.12 have a point for which the radial flow component reverses direction at closure depth (blue stars). At the higher Froude numbers no such point is observed. This does not mean that such a flow reversal point is absent during the complete time of collapse, since in Fig. 6.10b it can be seen that this point travels away from the axis of symmetry as the collapse is approached ($\tau \to 0$). The radial flow reversal point comes into existence at the wall of the void at the moment that the cavity starts to collapse and the flow direction is reversed inward. In Fig. 6.10b it is also seen that the radial flow reversal point travels outward during the cavity collapse much faster for higher Froude number.

Fig. 6.10b leads us to three observations which are relevant for the model of the cavity collapse presented in Chapter 5 and Section 6.3.1 of this chapter; (i) Since radial flow reversal occurs when the cavity starts to collapse and the flow is reversed inwards, the topology of the flow at closure depth differs between the expansion and contraction phase of the cavity. This justifies our assumption of taking different values for h_∞^{expa} and h_∞^{ctra} during the expansion and contraction of the cavity in the regime dominated by hydrostatic pressure (see Section 6.3.1). (ii) As the distance of the radial flow reversal during the collapse moves away faster at higher Froude number, presumably a higher value for h_∞^{expa} should be assumed for larger Froude number, since the distance where the flow is quiescent should be correlated to h_∞^{expa} (see Section 6.3.1). (iii) In Chapter 5 we show in Eq. 5.4 that there are two scaling regimes for the neck radius, a first regime where the neck radius scales as a pure power law of time, and a second regime, where a logarithmic correction of time has to be taken into account. The crossover between both regimes is given by the length scale $h_{max}^2/h_\infty^{ctra}$. As we find from Fig. 6.10b that for all Froude numbers the distance of the radial flow reversal increases as the pinch-off is approached. We can presume that thus also h_∞^{ctra} increases as the pinch–off is approached. This means the cross–over length scale $h_{max}^2/h_\infty^{ctra}$ decreases with time.
Therefore the time from the start of the collapse until the pinching neck decreases to the size $h_{max}^2/h_\infty^{ctra}$ will be longer, as compared to the assumption of a constant value for h_∞^{ctra}. This effect is stronger for increasing Froude number, since the radial flow reversal point at closure depth moves away faster and further during the collapse for higher Froude number.

In Fig. 6.11 the path of the stagnation point is shown for the simulations of Fig. 6.10 at Fr = 3.4 and Fr = 10.2. For both experiments the stagnation point not only moves away from the axis of symmetry as the pinch-off is

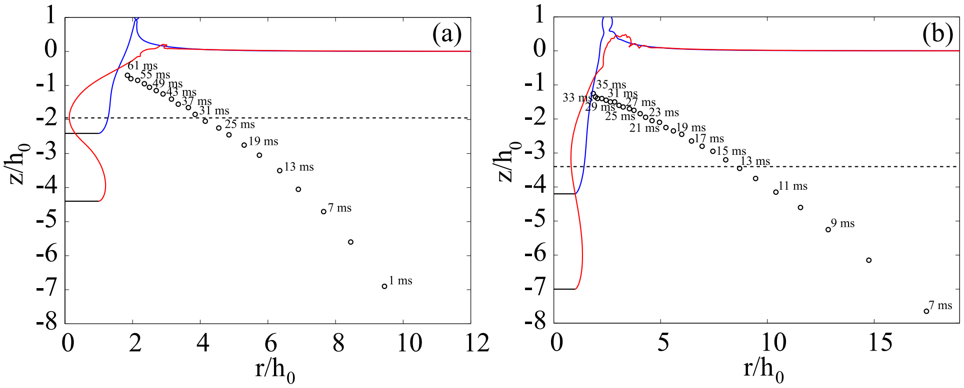

Figure 6.11: The open circles show the path of the stagnation point of the flow for Froude 3.4 (a) and 10.2 (b). For (a) the first observation of the stagnation point is made at $\tau = 61$ ms until 1 ms before closure at intervals of 3 ms. In (b) the first observation is made at $\tau = 35$ ms until 7 ms before closure at intervals of 1 ms. For clarity only the time till closure is indicated for every second observation. Further more, the void profiles at the time of the first (blue) and last (red) observation are shown. The depth of the final closure is indicated by the dotted line.

approached, but it also moves down in the axial direction and even crosses the depth of closure. A similar path of the stagnation is observed for *all* the simulations of Fig. 6.10, meaning that only at one instant during the collapse of the cavity does the radial flow reversal point truly coincide with the stagnation point.

To verify our interpretation of the dynamics of the flow reversal in relation to h_∞^{expa} and h_∞^{ctra}, we will compare the dynamics of the radius of the void at closure depth with the theoretical prediction of Eq. (6.5) and Eq. (6.8). As was explained in Section 6.3.1 we have four unknown parameters in Eq. (6.5) and Eq. (6.8), namely α_{expa}, β_{expa}, α_{ctra}, and β_{ctra}. One of these parameters is eliminated by the relation $\alpha_{ctra} = \alpha_{expa}\sqrt{\beta_{expa}/\beta_{ctra}}$ (see Section 6.3.1), leaving three parameters to match Eq. (6.5) and Eq. (6.8) to the radial dynamics from the simulations. The three parameters are the initial outward velocity $\alpha_{expa}V$ of the cavity at the beginning of the expansion phase and the logarithm of the distances related to the radial flow reversal point in the expansion phase β_{expa} $(= \log(h_{max}/h_\infty^{expa}))$ and contraction phase β_{ctra} $(= \log(h_{max}/h_\infty^{ctra}))$. At first sight, one would assume that the initial outward velocity $\alpha_{expa}V$ could easily be determined from simulation or experiment, since it is observed as the angle at which the free surface leaves the disk. However when this angle is investigated, it is found to depend on the distance from the disk's edge. As one approaches the disk's edge close enough, the separation of the free surface becomes parallel with the disk, so $\lim_{s\downarrow 0}\alpha_{expa}V \rightarrow \infty$, where s is the distance along the free surface to the edge of the disk. This means that $\alpha_{expa}V$ is a useful theoretical concept, but the outward radial flow is more easily determined by the maximal expansion of the cavity.

As was seen in Fig. 6.10b the radial stagnation, which is related to h_∞^{ctra} has non straight-forward dynamics. To simplify our theoretical approach we will set the corresponding β_{ctra} constant to a value which represents a time average of the dynamics of the stagnation point in the contraction phase. We will assume h_∞^{expa} to be a time averaged constant too.

The three parameters α_{expa}, β_{expa}, and β_{ctra} are determined by a least square fit to the dynamics of the neck obtained from the simulations. Fig. 6.12a shows the comparison between these fits of Eq. (6.5) and Eq. (6.8) (red dashed line) and the simulations (blue solid line) at two different froude numbers of 3.4 and 200. The approximation is found to be in excellent agreement throughout the collapse, faithfully reproducing the maximum expansion of the cavity and the complete time of collapse.

If in Eq. (6.5) the constants β_{expa} and β_{ctra} are set to -1 and therefore also $\alpha_{ctra} = \alpha_{expa}$, we arrive at the cavity dynamics proposed by [10] for impacting spheres and cylinders. These dynamics are shown in Fig. 6.12b with the only free parameter α_{expa} also determined by a least square fit to the data. This approximation is seen to qualitatively reproduce the trend for the maximum expansion and collapse time, but fails to capture the exact values. It is also conceptually different, as the authors of [10] propose the cavity dynamics to be symmetric around the maximum expansion, while we try to capture the asymmetry around this point found in experiments and simulations. Our solution of Eq. (6.5) is explicitly not symmetric, since it allows for different values of β at $t < t_{max}$ (β_{expa}) and $t > t_{max}$ (β_{ctra}).

In Section 6.3.1 the scaling of $z_{coll}/h_0 = \sqrt{\alpha_{expa}\beta_{expa} + \alpha_{ctra}\beta_{ctra}}Fr^{1/2}$ was derived. The quantity $\sqrt{\alpha_{expa}\beta_{expa} + \alpha_{ctra}\beta_{ctra}}$ was found to be independent of Fr and its value $\sqrt{\alpha_{expa}\beta_{expa} + \alpha_{ctra}\beta_{ctra}} \approx 1.10$ was found from a fit to the numerical and experimental closure depth z_{coll}. However from a similar procedure as for Fig. 6.12a the quantity $\sqrt{\alpha_{expa}\beta_{expa} + \alpha_{ctra}\beta_{ctra}}$ can also be obtained from the radial dynamics. If Eq. (6.5) and Eq. (6.8)

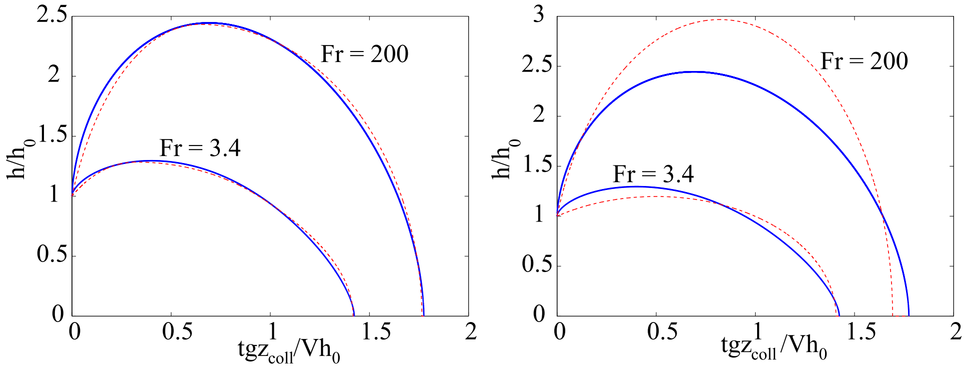

Figure 6.12: (a) The time dynamics of the radius of the cavity at closure depth for different Froude number. The solid blue line represents the simulations and a least square fit of the approximation by Eq. (6.5) and Eq. (6.8) is given by the dashed red line. (b) The radial dynamics are again given by the solid blue line. The red dashed line shows a lest square fit of the dynamics proposed by [10], which consists of Eq. (6.5) with β_{expa} and β_{ctra} set to -1.

are fitted to the radial dynamics for a range of Froude numbers, we find $\sqrt{\alpha_{expa}\beta_{expa} + \alpha_{ctra}\beta_{ctra}}$ to actually weakly depend on the Froude number (see Fig. 6.13). In light of this observation we compensate z_{coll}/h_0 with the expected behavior of $Fr^{1/2}$ and indeed find a residual Froude dependence in Fig. 6.14. The dependence of $\sqrt{\alpha_{expa}\beta_{expa} + \alpha_{ctra}\beta_{ctra}}$ on Froude is logarithmic and therefore hard to notice in a conventional logarithmic plot like Fig. 6.9.

If we compensate z_{coll} not only for $Fr^{1/2}$ but indeed take the full scaling of $z_{coll}/h_0 = \sqrt{\alpha_{expa}\beta_{expa} + \alpha_{ctra}\beta_{ctra}}Fr^{1/2}$ into account, including the Froude dependence of $\sqrt{\alpha_{expa}\beta_{expa} + \alpha_{ctra}\beta_{ctra}}$, we recover the correct scaling of z_{coll} for higher Froude numbers (see Fig. 6.14). The scaling at lower Froude number (Fr¡10) deteriorates by this operation, since z_{coll} at lower Froude numbers is close to $\propto$ Fr$^{1/2}$.

Although the approximation by [10] does not reproduce the radial dynamics of the cavity, it did produce a $\propto$ Fr$^{1/2}$ scaling for the final depth $z_{disk,\,coll}$ and closure depth z_{coll}. Here, the prefactor of the scaling law consisted of $\sqrt{8\alpha_{expa}}$, where α_{expa} was assumed to be independent of Froude. However, since different α_{expa}'s are needed for the fit Fig. 6.12b and based on Fig. 6.14, α_{expa} is found to depend on Froude.

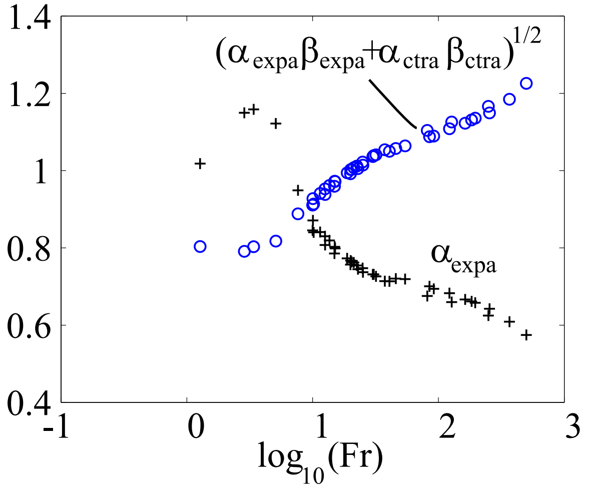

Figure 6.13: The quantity $\sqrt{\alpha_{expa}}$ and $\sqrt{\alpha_{expa}\beta_{expa}+\alpha_{ctra}\beta_{ctra}}$ obtained from a fitting routine similar to the least square fits of Fig. 6.12a. Both α_{expa} and the quantity $\sqrt{\alpha_{expa}\beta_{expa}+\alpha_{ctra}\beta_{ctra}}$ are found to weakly depend on Froude.

We now return to our previous observations on the flow and the possible consequences for the h_∞'s. (i) The flow reversal which occurs when the cavity starts to collapse indeed introduces an asymmetry in the behavior around the maximum expansion. This is clearly observed in the radial dynamics of Fig. 6.12 and a different β_{expa} and β_{ctra} have to be introduced to account for this effect. (ii) As the distance of the radial flow reversal during the collapse moves away faster at higher Froude number, we indeed have to introduce a larger h_∞^{ctra} (or larger $\mid \beta_{ctra} \mid$) for higher Froude number to account for this effect in Fig. 6.12a.

In Fig. 6.10a it is also observed that the flow is closer to purely two–dimensional radial sink flow ($v_r \propto 1/r$) for larger Froude number. This can be concluded from the decrease in the minimum of $v_r r$ with increasing Froude number. The fact that the radial flow is closer to $\propto 1/r$, means that the collapsing cavity resembles more and more the collapse of the infinite cylinder described by Eq. (6.1). This is a possible reason why the scaling $z_{coll}/h_0 = \sqrt{\alpha_{expa}\beta_{expa}+\alpha_{ctra}\beta_{ctra}}Fr^{1/2}$ seems to work best for higher Froude number in Fig. 6.14.

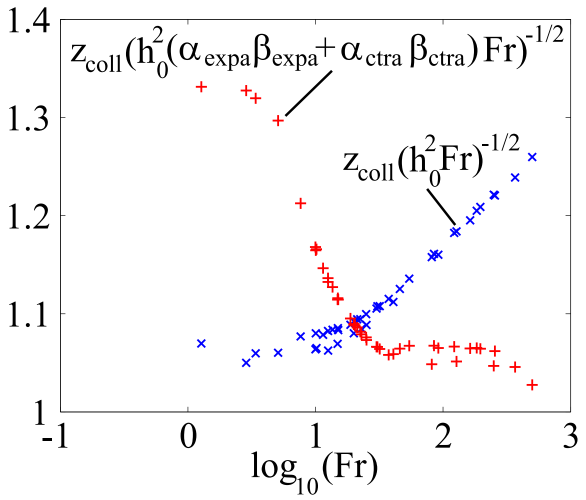

Figure 6.14: The closure depth of the cavity z_{coll}/h_0 compensated by the expected behavior of $\propto Fr^{1/2}$ from Section 6.3.1 is found to be weakly dependent on Fr. By taking into consideration the Fr dependence of $\sqrt{\alpha_{expa}\beta_{expa} + \alpha_{ctra}\beta_{ctra}}$ observed in Fig. 6.13, we can compensate z_{coll}/h_0 by $\sqrt{\alpha_{expa}\beta_{expa} + \alpha_{ctra}\beta_{ctra}}Fr^{1/2}$ to remove the Froude dependence at higher Froude numbers.

6.3.3 Air Entrainment

In this section, the proposed model for the cavity collapse (Sections 6.3.1 and 6.3.2) will be used to understand the Froude dependence of the volume of air V_{bubble} enclosed at pinch-off.

This process is clearly visible in Fig. 6.2. The volume of this bubble V_{bubble} is found to be solely dependent on the Froude number, more over, it is found to exhibit scaling law behavior with Froude. The scaling law for the volume of the bubble observed in experiment and simulation is found to be $V_{bubble} \propto \mathrm{Fr}^{\lambda}$, with $\lambda = 0.78$ (see Fig. 6.15a).
This is surprising, since for the impact of a liquid mass on a free surface the volume of air entrained in the process scales with a different exponent $V_{bubble} \propto \mathrm{Fr}^{1.0}$ [7]. In the remainder of the section we will explain the scaling of the air entrainment by the disk based on the findings of Section 6.3.1.

In Section 6.3.1 it was found that the axial length of the enclosed bubble at pinch–off scales roughly as $(z_{coll} - z_{disk,\,coll})/h_0 \approx 1.10\mathrm{Fr}^{1/2}$. The prefactor

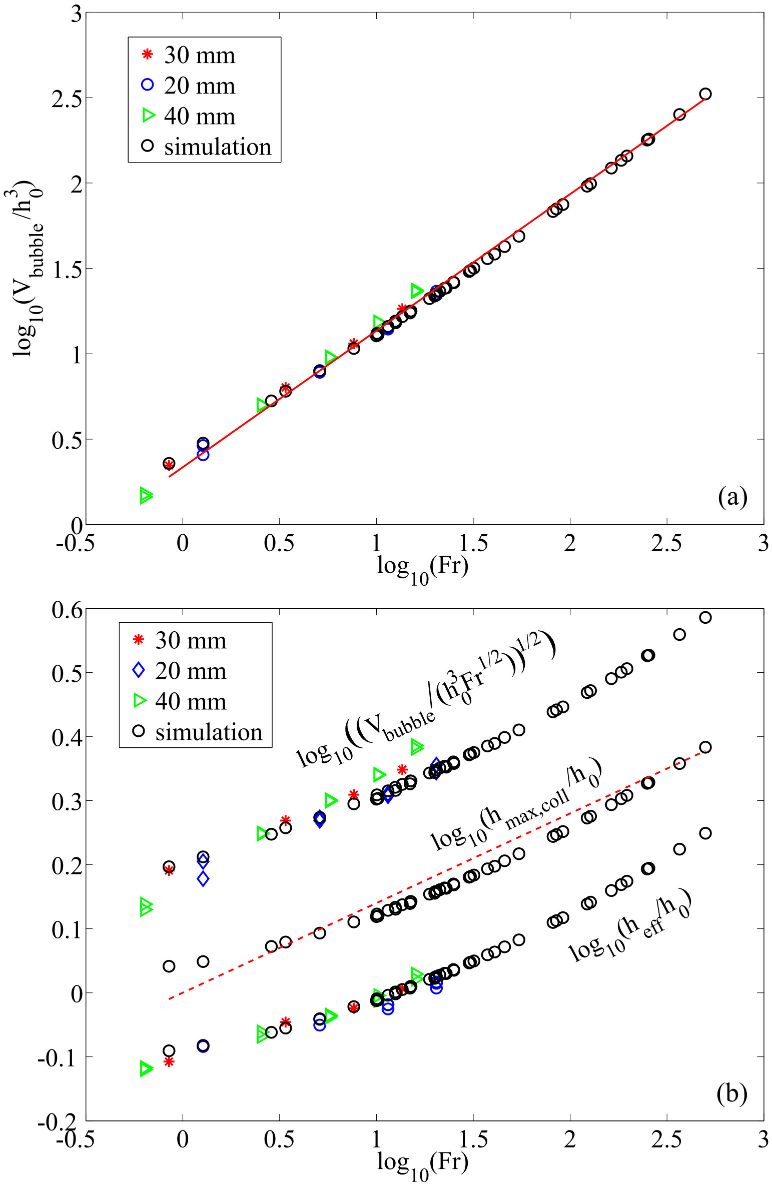

Figure 6.15: (a) The volume of the bubble V_{bubble} entrained during the collapse of the cavity from experiments (colored symbols) and simulations (black open circles) as a function of the Froude number. The red line indicates a power–law of $V_{bubble}/h_0^3 \propto \mathrm{Fr}^{0.78}$.

(b) The entrained volume V_{bubble} is normalized by $h_0^3\mathrm{Fr}^{1/2}$, since according to Section 6.3.1 the axial length scale of the bubble scales roughly as $z_{disk,\,coll} - z_{coll} \propto h_0\mathrm{Fr}^{1/2}$. In the same plot also the effective radius h_{eff} and the maximum radius $h_{max,\,coll}$ of the entrained air bubble at the moment of pinch–off are given as a function of Froude. Since the bubble volume V_{bubble} exhibits scaling close to $\propto \mathrm{Fr}^{0.78}$, all shown quantities follow a scaling close to $\propto Fr^{0.14}$ (red dashed line).

of 1.10 should be thought of as an average of the weakly Froude dependent prefactor $\sqrt{\alpha_{expa}\beta_{expa} + \alpha_{ctra}\beta_{ctra}}$. The axial length $z_{coll} - z_{disk,\,coll}$ of the enclosed bubble can obviously not solely account for the observed volumetric Froude scaling with exponent $\lambda = 0.78$. The radial length scale h_{rad} of the bubble should therefore also scale with Fr. From the following expression,

$$V_{bubble} \propto (z_{disk,\,coll} - z_{coll}) = \mathrm{Fr}^{0.78} h_{rad}^2 \propto \mathrm{Fr}^{0.78} = \mathrm{Fr}^{1/2} \cdot (\mathrm{Fr}^{0.14})^2 \,, \quad (6.18)$$

it is clear that $h_{rad} \propto \mathrm{Fr}^{0.14}$ in order to reproduce the correct scaling for V_{bubble}. The equivalent of h_{rad}, namely the effective, or average, radius h_{eff} of the bubble can be computed directly from the experimental and numerical cavity profiles without any assumption of the axial length scale by,

$$h_{eff}^2 = \frac{1}{(z_{disk,\,coll} - z_{coll})} \int_{z_{coll}}^{z_{disk,\,coll}} h^2(z) dz \,. \quad (6.19)$$

The magnitude of h_{eff} beyond h_0 will in turn be dictated by the expansion of the cavity. This expansion can be quantified by the maximal radius of the bubble $h_{max,\,coll}$ at the time of pinch–off. $h_{max,\,coll}$ can be directly observed from the cavity profile at the time of pinch–off, as the maximal radius for a depth between $z_{disk,\,coll} < z < z_{coll}$.

In Fig. 6.15b we compare the scaling of V_{bubble}, h_{eff}, and $h_{max,\,coll}$. We compensate V_{bubble} with the expected scaling behavior $z_{disk,\,coll} - z_{coll} \propto h_0 \mathrm{Fr}^{1/2}$ of its axial length scale. According to Eq. (6.18) this would leave only the square of the radial length scale h_{rad}, therefore we take the square root of the compensated volume.
The scaling of both h_{eff} and $h_{max,\,coll}$ is found to indeed closely follow the behavior of the radial length scale h_{rad} obtained by rescaling the volume of the bubble $(V_{bubble}/h_0^3 \mathrm{Fr}^{1/2})^{1/2}$ (Fig. 6.15b). All of these three length scales exhibit scaling close to the proposed $\propto \mathrm{Fr}^{0.14}$. This means that the Froude number scaling of the volume of air enclosed at the impact of a disk is set by the Froude dependence of two length scales, namely the depth of closure and the radial expansion of the cavity.

After the collapse of the void, the downward jet will pierce the enclosed bubble and create a torroidal bubble which will trail a constant distance behind the descending disk. The volumetric oscillations of the torroidal bubble can be measured by imaging it directly or recording the radiating acoustic signal with a hydrophone. Both measurement methods show that the trailing bubble volumetrically oscillates. The natural frequency f_m of the oscillations of a spherical bubble are given by the Minnaert formula,

$$f_m = \frac{1}{2\pi h_{bubble}} \sqrt{\frac{3\sigma P_0}{\rho}}\,, \tag{6.20}$$

where h_{bubble} and P_0 denote respectively the radius of the bubble and the surrounding pressure. Surprisingly, the bubble enclosed at the closure does not oscillate at the Minneart frequency for a spherical bubble comprised of the same volume. But the bubble oscillates at the Minneart frequency of a spherical bubble at atmospheric pressure with a radius equal to that of the disk $h_{bubble} = h_0$ [24]. This is illustrated for the case of a disk of $h_0 = 20$ mm impacting at a constant velocity of 0.5 m/s, even though the bubble is far from spherical it volumetrically oscillates at the frequency (175 Hz) of a spherical bubble with radius $h_{bubble} = 20$ mm.

6.3.4 Minimal Neck Radius

For the local behavior of the cavity at pinch-off, one has to discriminate between the behavior of the neck at the depth of closure $h_{coll}(t)$ and the dynamics of the minimal neck radius $h_{min}(t)$. The corresponding depth at which h_{min} is observed, $z_{min}(t)$, is not a constant and varies until in the final stage of the pinch-off it coincides with the closure depth z_{coll}. In Chapter 5 the difference between h_{coll} and h_{min} was shortly addressed, but in this section we will quantify the dynamics of h_{min}.

The way in which the depth of the minimal radius z_{min} approaches the depth of closure z_{coll} can be deduced from Eq. (6.1) in the following fashion. To approximate the cavity shape, we will assume that the shape of the cavity is mainly determined by the expansion and contraction phases (see Fig. 6.8). In Section 6.3.1 the expansion phase was found to end at

$$\hat{t}_{max} = \alpha_{expa}\beta_{expa}(h_0 V)/(gz)\,, \tag{6.21}$$

if $\hat{t} = t - t_{reach}$. Using Eq. (6.5), also the expanded cavity radius at which the expansion halts can be found,

$$h_{max} = h_0 \sqrt{1 + \frac{(\alpha_{expa} V)^2}{gz} \beta_{expa}}\,. \tag{6.22}$$

As is shown in Fig. 6.8, the time $\hat{t}_{max}$ and the radial expansion h_{max} are the initial conditions for the second phase, the contraction, which will mainly determine the shape of the cavity. Using these initial conditions with Eq. (6.5),

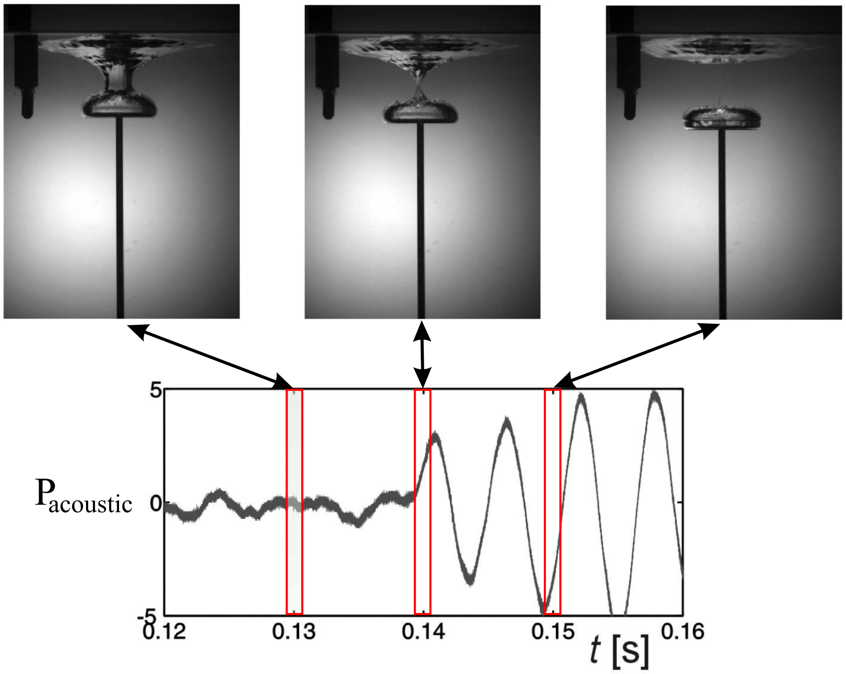

Figure 6.16: The graph shows the measured acoustic pressure $P_{acoustic}$ in arbitrary units during the impact event of a disk of radius $h_0 = 20$ mm at a velocity $V = 0.5$ m/s. The boxes in the graph show the exposure time of the respective frames (at $t = 0.13$, 0.14, and 0.15 s) indicated by the arrows. $P_{acoustic}$ is seen to oscillate at a 175 Hz after pinch-off, this frequency corresponds to the natural frequency (Minneart frequency) of a spherical bubble with a 20 mm radius. The hydrophone used to record the acoustic pressure can be seen in the upper left corner of the snapshots.

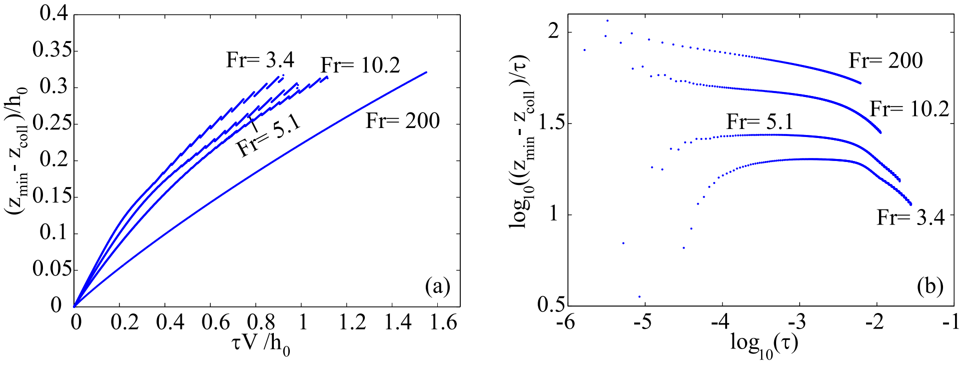

Figure 6.17: (a) The difference between the depth of the minimal radius z_{min} and the depth of closure z_{coll} of the cavity as a function of the time till collapse for different Froude numbers. The data is obtained by the boundary integral simulation from when the minimal radius equaled the disk radius h_0. (b) Shows a doubly logarithmic plot of the same data as (a), only now $z_{min} - z_{coll}$ is compensated by τ in order to reveal the theoretically predicted scaling of $z_{min} - z_{coll} \propto \tau$ as a horizontal slope. The jumps in the data are a result of the regridding routine in our boundary integral simulation and have no physical meaning.

the dynamics of $h(z, \hat{t}\,)$ in the contraction phase can be written as,

$$h(z,\hat{t}\,)^2 = -\frac{gz}{\beta_{ctra}}\hat{t}^{\,2} + 2\alpha_{expa}\frac{\beta_{expa}}{\beta_{ctra}}h_0V\hat{t} + h_0^2\left[1 + \alpha_{expa}^2\frac{\beta_{expa}}{\beta_{ctra}}\frac{\beta_{ctra} - \beta_{expa}}{gz}V^2\right] . \tag{6.23}$$

Here, $\hat{t} = 0$ corresponds to the time that the disk passes depth z. For $\beta_{expa} = \beta_{ctra} = -1$, this result is identical to the one obtained by [10]. If we take the time the disk needs to reach a certain depth into consideration, we can obtain the shape of the cavity over the whole time by substituting $\hat{t} = t - z/V$,

$$\begin{aligned} h(z,t)^2 = -\frac{gz}{\beta_{ctra}}\left(t - z/V\right)^2 + 2\alpha_{expa}\frac{\beta_{expa}}{\beta_{ctra}}h_0V\left(t - z/V\right) \\ + h_0^2\left[1 + \alpha_{expa}^2\frac{\beta_{expa}}{\beta_{ctra}}\frac{\beta_{ctra} - \beta_{expa}}{gz}V^2\right] . \end{aligned} \tag{6.24}$$

From this void shape the depth of the minimal radius z_{min} is obtained by computing $dh/dz = 0$, which gives

$$3\left(\frac{z}{V}\right)^2 - 4\left(\frac{z}{V}\right)t + t^2 + \alpha_{expa}\beta_{expa}\frac{h_0}{g}\left[2 + \alpha_{expa}\frac{(\beta_{ctra}-\beta_{expa})h_0}{g}\left(\frac{V}{z}\right)^2\right] = 0\,, \tag{6.25}$$

Under the assumption of z_{min} close to the depth of closure, $z^2 \approx z_{coll}^2 = (\alpha_{expa}\beta_{expa} + \alpha_{ctra}\beta_{ctra})\mathrm{Fr}h_0^2$, and using $\alpha_{expa}^2\beta_{expa} = \alpha_{ctra}^2\beta_{ctra}$ (cf. Section 6.3.1) we find

$$\alpha_{expa}\frac{(\beta_{ctra}-\beta_{expa})h_0}{g}\left(\frac{V}{z_{coll}}\right)^2 \approx \frac{1-\zeta}{\zeta+\sqrt{\zeta}}\,, \quad \text{with}\,\zeta = \frac{\beta_{expa}}{\beta_{ctra}}\,. \tag{6.26}$$

This quantity is found from numerical fits like those in Fig. 6.12a to be 0.36 ($\zeta = 0.54$) for a Froude number of 3.4, 0.40 ($\zeta = 0.51$) for Fr = 10.2, and 0.36 ($\zeta = 0.54$) at the considerable Froude number of 200. Therefore we neglect this second term in the brackets of Eq. (6.25) and can solve the equality to find

$$z_{min} = \frac{1}{3}tV\left(2 - \sqrt{1 - 6\frac{\alpha_{expa}\beta_{expa}}{gt^2}h_0}\right)\,. \tag{6.27}$$

From this result the linear dependence of z_{min} on time should be noted. Using this dependence of $z_{min}(t) = c\,t$ and the definition $z_{min}(t_{coll}) = z_{coll} = c\,t_{coll}$, we find $z_{coll} - z_{min}(t) = c\,(t_{coll} - t)$. This scaling is indeed immediately clear for high Froude number (Fr=200) from Fig. 6.17a. The compensated doubly logarithmic plot of Fig. 6.17b reveals that also Fr = 3.4, 5.1, and 10.2 exhibit a scaling of z_{min} close to $(z_{min}(t) - z_{coll})/(t_{coll} - t) \propto c$.

The scaling for z_{min} is observed close to pinch–off in the collapse regime (see Fig. 6.8), however the theoretical description of this scaling is deduced from Eq. (6.5) which holds for the expansion and contraction phases (see Fig. 6.8). This is not a contradiction, since Eq. (6.8) for the collapse regime is an approximation of Eq. (6.5), so even near pinch off, the solutions of both equations are remarkably close. The cross-over between the two regimes was for convenience chosen at $h = h_0$, but Eq. (6.5) captures the cavity dynamics well, far into the collapse regime.

As the pinch-off is approached, not only the depth of the minimal radius z_{min} converges to the depth of closure z_{coll}, but naturally also the minimal radius itself h_{min} approaches the radius at the depth of closure h_{coll} as can be seen in Fig. 6.18a. Therefore close to pinch–off, $h_{min} \approx h_{coll}$, which is an important observation, since the radial dynamics of h_{coll} can be described by Eq. (6.1) as was seen in Chapter 5, whereas the same description does not hold for h_{min} as it is not observed at a constant depth z. In Fig. 6.18a, the relative difference between h_{min} and h_{coll} is seen to be smaller for increasing Froude number due to the cavity taking a more cylindrical shape at higher Froude number.

The approach of h_{min} to h_{coll} can in fact be deduced from the cavity profile. The local shape of the void at the minimal neck radius was found in Chapter 5 to be parabolic. Thus we can capture the shape of the profile in axial direction by the radius of curvature R (see Fig. 6.19). Since the approach of the depth of the minimal radius z_{min} to the depth of closure z_{coll} is governed by a power law of time, the approach of h_{min} to h_{coll} can also be described by a power law of time. At the minimal radius, one can define the radius of curvature R in the axial direction as following ,

$$1/R(t) = d^2r/dz^2|_{z=z_{min}} \,, \tag{6.28}$$

and if the shape of the interface can be taken to be locally parabolic, this implies

$$r = (\delta z)^2/R(t) + h_{min}(t) \,, \quad \text{with}\, \delta z = z - z_{min}(t) \,. \tag{6.29}$$

If we take the closure depth as reference, this equation can be rewritten,

$$h_{coll} - h_{min}(t) = (z_{coll} - z_{min})^2/R(t) \,. \tag{6.30}$$

In Chapter 5 the radius of curvature R was found to be a power law of the time. In Fig. 5.2a the $R \propto \tau^{\alpha_R}$ behavior is illustrated. In the same chapter in Fig. 5.2d the exponent α_R was observed to be dependent on Froude. So combining these findings with the linear time dynamics for $z_{coll} - z_{min} \propto \tau$, we find from the geometrical considerations of Eq. (6.30) that h_{min} approaches h_{coll} as $h_{coll} - h_{min} \propto \tau^{2-\alpha_R}$.
This scaling is indeed readily observed in Fig. 6.18b for intermediate Froude numbers, however the lower and higher Froude numbers of 3.4 and 200 seem to deviate from this scaling due to small deviations of the proposed scaling of $z_{coll} - z_{min} \propto \tau$ which are observed for these Froude numbers in Fig. 6.17b.

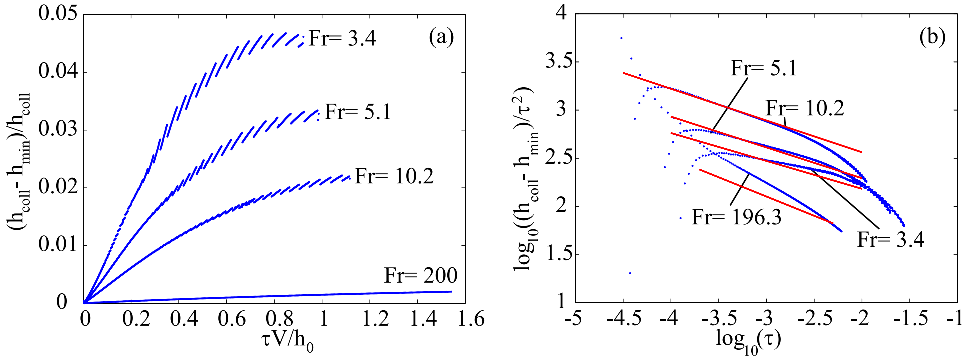

Figure 6.18: (a) The relative difference of the minimal radius h_{min} and the radius at the closure depth h_{coll} of the cavity as a function of time for different Froude numbers. This relative difference is smaller for increasing Froude number as the cavity becomes more cylindrical. (b) Shows a doubly logarithmic plot of the same data as (a), only now $h_{coll} - h_{min}$ is compensated by τ^2 to reveal the resultant scaling with $\tau^{-\alpha_R}$. The scaling exponent of the radius of curvature α_R is dependent on the froude number and indicated by the red lines for the different Froude numbers $(\alpha(\mathrm{Fr{=}3.4})_R = 0.29; \alpha(\mathrm{Fr{=}5.1})_R = 0.32; \alpha(\mathrm{Fr{=}10.2})_R = 0.33; and\alpha(\mathrm{Fr{=}200})_R = 0.40))$. The jumps in the data are a result of the regridding routine in our boundary integral simulation and of no physical meaning.

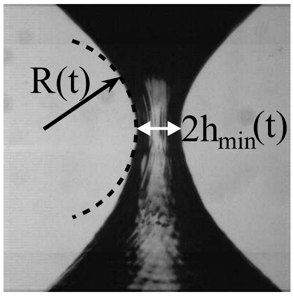

Figure 6.19: The radius of curvature $R(t)$ of the void profile determined at the depth $z_{min}(t)$ of the minimum neck radius $h_{min}(t)$.

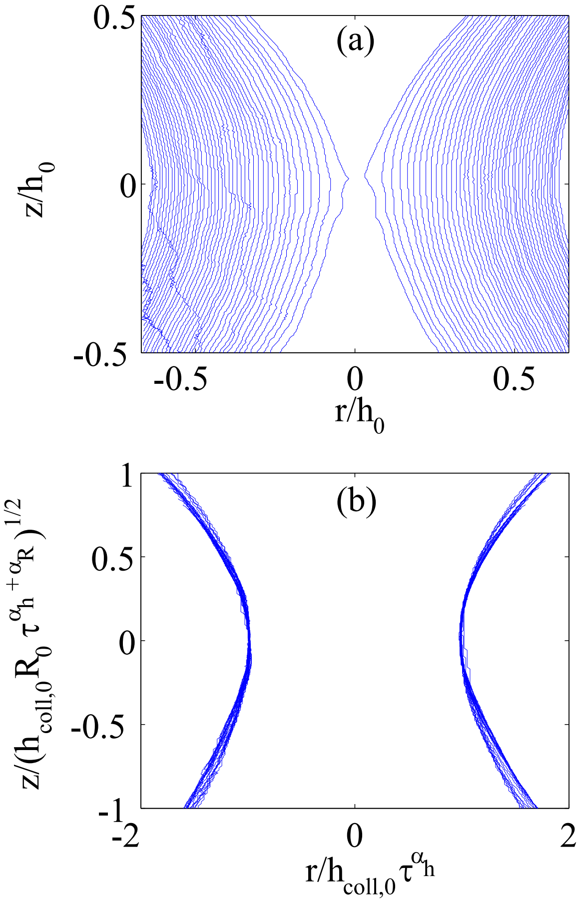

Figure 6.20: The profiles of the void obtained by experiments for $h_0 = 30$ mm and $V = 1.0$ m/s (Fr = 3.4). (a) Void profile obtained at different instances in time. (b) Void profile in which the radial and axial coordinates were rescaled with the powerlaws of $h_{coll}(t)$ and $\sqrt{h_{coll}(t)R(t)}$ respectively. Here, the numerically determined power–laws were used for the neck radius $h(\tau)$ and the radius of curvature $R(\tau)$ (see main text).

6.3.5 Cavity shape at pinch-off

We now turn to the time evolution of the free-surface profile close to pinch–off. Previously, in Chapter 5 we found a strong dependence of the pinch–off process on initial conditions, in our case represented by the Froude number. Due to the different dependence of the exponent of the power–law for h_{coll} and R the void collapse was found to be not self–similar.

In other words, it was not possible to collapse the free surface profiles at different times onto a single shape using a single time dependent and Froude–independent length-scale. In this section we will elaborate on how the cavity shape depends on the Froude number, close to pinch–off.

If the pinch–off would be self-similar, the free-surface profiles at different times (cf. Fig. 6.20a) would superpose when scaled by any characteristic length, e.g., the neck radius at closure depth $h_{coll}(t)$. As was discussed in the previous section, the depth of minimum radius z_{min} increases somewhat as the collapse progresses and it is therefore necessary to translate the profiles in the vertical direction so as to match the position of the minimum radius point before attempting this operation. Even if this is done, the result fails to collapse the void profiles onto a single shape when using a single time–dependent length-scale.

To characterize the free-surface shapes near the minimum point, one thus needs not only $h_{coll}(t)$, but also a second length-scale, the radius of curvature $R(t)$ in the vertical plane (see Fig. 6.2 and Fig. 6.19). As was discussed in the previous chapter, both the time-evolution of h_{coll} and R were found to follow a power law of time ($h_{coll} = h_{coll,0}\tau^{\alpha_h}$ and $R = R_0\tau^{\alpha_R}$, see also Fig. 5.2a). This makes it possible to rescale the experimentally obtained void profiles of Fig. 6.20a onto a single shape. When the radial dimension r is scaled by h_{coll}, it follows from Eq. (6.29) that the axial dimension z should be scaled by $\sqrt{h_{coll}R}$. If this is undertaken, the profiles do collapse onto a single curve as can be seen in Fig. 6.20b. The collapse of the profiles does not only signal that their shape is very close to parabolic, but again visualizes the statement from Chapter 5, that the collapse is self-similar of the second kind [25], since the radial and axial coordinates are rescaled by power laws of time with different exponents.

The recent findings by [26] and [27] indicate that the scaling laws presented for h_{coll} and R have an exponent which slowly varies with time. Our findings so far cannot confirm or disprove this theory, since our experiments and boundary integral simulations do not have sufficient temporal range to find such small deviations in the exponent. To escape the limitation of the experimental range set by the viscosity, surface tension, and air, the experiment should be scaled up to an unrealistic size (a container size of 40000 meters) to match the 10 decades in time presented in the numerical calculations of [27].

Of course our findings do have a clear dependence of the scaling exponents on the Froude number. Even though the scaling exponents we observe, should be viewed as time averaged in this context, it is possible to derive the constant in the exponent set by the initial condition in [27] from Fig. 5.2d.

6.4 Conclusions

In this article we investigate the purely gravitationally induced collapse of a surface cavity created by the controlled impact of a disk on a water surface. We find excellent agreement of the interface between experiments and boundary integral simulations. Besides that also the flow surrounding the cavity is faithfully reproduced in the simulations. The topology as well as the magnitude of the flow in the simulations agree perfectly with the flow obtained from experiment by particle image velocimetry.
In experiments it is found that a secondary air effect, the "surface seal", has a significant influence on the cavity shape at high Froude number. Since the surface seal phenomenon (and its influence) is more pronounced at higher impact velocities, it limits our experimental Froude number range. However, by using boundary integral simulations in which the air was intentionally excluded, we manage to remove this upper bound on our observations.

Because the velocity of the impacting disk is a constant control parameter in our experiments, a simple theoretical argument based on the collapse of an infinite, hollow cylinder describes the key aspects of the transient cavity shape.

The model accurately reproduces the dynamics of the cavity including its maximal expansion and total collapse time. It also captures the scaling for the depth of closure and the total depth of the cavity at pinch–off, and predicts their ratio to be close to 2, where 2.1 is found in experiments and simulation.
There is a close similarity of this description to the cavity dynamics proposed by Ducleaux *et al.* [10], however, by introducing the asymmetry between the radial expansion and collapse, we find a better agreement between the theory and the radial dynamics of the cavity. A difference in the flow surrounding the cavity is found to be responsible for the asymmetry. Our approach is also conceptually different, as the authors of [10] take α_{expa} to be independent of the Froude number, while we find it is weakly dependent on Froude and that it is the quantity $\sqrt{\alpha_{expa}\beta_{expa} + \alpha_{ctra}\beta_{ctra}}$ which is of interest. In addition, our description includes the regime of the collapse, which is solely driven by continuity.

We find the volume of air entrained by the impact of the disk to scale as $\propto \mathrm{Fr}^{0.78}$. This scaling is set by the Froude dependence of two length scales, namely the axial length scale, distance between the pinch-off point and the disk, and the radial expansion of the cavity.

The dynamics of the cavity radius at the depth of closure is thus well described by theory. The minimal radius of the void is different from the radius at closure depth, as the depth of the minimal radius only approaches the closure depth in the limit of pinch–off. The parabolic approximation captures this approach of the depth of the minimal radius to the eventual pinch–off depth, which in simulation and theory is found to be linear with time. The translation of the minimal radius is of interest, as this should be accounted for in an approach as proposed by [26] and [27], since the axial translation could introduce non-universal behavior for the pinch–off after the impact of a disk.

References

[1] A.M. Worthington, *A study of splashes* (Longman and Green, London, 1908).

[2] A.M. Worthington and R.S. Cole, *Impact with a liquid surface, studied by the aid of instantaneous photography*, Phil. Trans. R. Soc. Lond. A **189**, 137 (1897).

[3] M. Rein, *Phenomena of liquid drop impact on solid and liquid surfaces*, Fluid Dyn. Res. **12**, 61 (1993).

[4] A.I. Fedorchenko and A.-B. Wang, *On some common features of drop impact on liquid surfaces*, Phys. Fluids **16**, 1349 (2004).

[5] H.N. Oguz and A. Prosperetti, *Bubble entrainment by the impact of drops on liquid surfaces*, J. Fluid Mech. **219**, 143 (1990).

[6] H.N. Oguz, A. Prosperetti, and A.R. Kolaini, *Air entrapment by a falling water mass*, J. Fluid Mech. **294**, 181 (1995).

[7] A. Prosperetti and H.N. Oguz, *Air entrainment upon liquid impact*, Phil. Trans. R. Soc. Lond. A **355**, 491 (1997).

[8] A. Prosperetti, L.A. Crum, and H.C. Pumphrey, *Underwater noise of rain*, J. Geophys. Res. **94**, 3255 (1989).

[9] M. Lee, R.G. Longoria, and D.E. Wilson, *Cavity dynamics in high-speed water entry*, Phys. Fluids **9**, 540 (1997).

[10] V. Ducleaux, F. Caillé, C. Duez, C. Ybert, L. Bocquet, and C. Clanet, *Dynamics of transient cavities*, submitted to Phys. Fluids (2006).

[11] J.-L. Liow, D. Morton, A. Guerra, and N. Gray, in *Howard Worner Inr. Symp. on injection in pyrometallurgy*, edited by M. Nilmani and T. Lehner (Pennsylvania, 1996).

[12] D. Morton, J.-L. Liow, and M. Rudman, *An investigation of the flow regimes resulting from splashing drops*, Phys. Fluids **12**, 747 (2000).

[13] H.P. Le, *Progress and trends in ink-jet printing technology*, J. Imag. Sci. Tech **42**, 49 (1998).

[14] A.U. Chen and O.A. Basaran, *A new method for significantly reducing drop radius without reducing nozzle radius in drop-on-demand drop production*, Phys. Fluids **14**, L1 (2002).

[15] J. de Jong, G. de Bruin, H. Reinten, M. van den Berg, H. Wijshoff, M. Versluis, and D. Lohse, *Air entrapment in piezo-driven inkjet printheads*, J. Acoust. Soc. Am. **120**, 1257 (2006).

[16] S.T. Thoroddsen and A.Q. Shen, *Granular jets*, Phys. Fluids **13**, 4 (2001).

[17] D. Lohse, R. Bergmann, R. Mikkelsen, C. Zeilstra, D. van der Meer, M. Versluis, K. van der Weele, M. van der Hoef, and H. Kuipers, *Impact on soft sand: Void collapse and jet formation*, Phys. Rev. Lett. **93**, 1980031 (2004).

[18] J.R. Royer, E.I. Corwin, A. Flior, M.-L. Cordero, M.L. Rivers, P.J. Eng, and H.M. Jaeger, *Formation of granular jets observed by high-speed x-ray radiography*, Nat. Phys. **1**, 164 (2005).

[19] J.W. Glasheen and T.A. McMahon, *Vertical water entry of disks at low froude numbers*, Phys. Fluids **8**, 2078 (1996).

[20] S. Gaudet, *Numerical simulation of circular disks entering the free surface of a fluid*, Phys. Fluids **10**, 2489 (1998).

[21] R. Bergmann, D. van der Meer, M. Stijnman, M. Sandtke, A. Prosperetti, and D. Lohse, *Giant bubble pinch-off*, Phys. Rev. Lett. **96**, 154505 (2006).

[22] S. Gekle, A. van der Bos, R. Bergmann, D. van der Meer, and D. Lohse, *Non-continuous froude number scaling for the closure depth of a cylindrical cavity*, submitted to Phys. Rev. Lett. (2006).

[23] H.N. Oguz and A. Prosperetti, *Dynamics of bubble growth and detachment from a needle*, J. Fluid Mech. **257**, 111 (1993).

[24] T. Grumstrup and A. Belmonte, *private communication* .

[25] G.I. Barenblatt, *Scaling, self-similarity and intermediate asymptotics* (Cambridge University Press, Cambridge, UK, 1996).

[26] J.M. Gordillo and M. Pérez-Saborid, *Dynamics of bubble-growth and detachment from a needle*, J. Fluid Mech. **562**, 303 (2006).

[27] J. Eggers, M.A. Fontelos, D. Leppinen, and J.H. Snoeijer, *Theory of the collapsing axisymmetric cavity*, submitted to Phys. Rev. Lett. (2006).

Chapter 7

The tubular jet[‡]

A vertical cylindrical tube is partially immersed in a water-filled container and pressurized to lower the fluid level inside the tube. As reported by Lorenceau et al. [1], a sudden release of the pressure in the tube creates a singularity on top of the rising free surface: At the very beginning of the process a jet emerges at the center of the surface, the strength of which strongly depends on the initial shape of the meniscus. Here, the time-evolution of the complex shape of the free surface and the flow around the cylindrical tube are analyzed using high-speed imaging, particle image velocimetry, and numerical simulations. The tubular jet is found to be created by the following series of events, which eventually lead to the flow focussing at the tube's center: A circular surface wave, produced by the funnelling of flow into the pipe, is pushed inwards by the radial flow directly underneath the surface. As the wave moves inward and eventually collapses at the center of the tube, a mound of fluid grows in the center due to the converging flow in the bulk. This converging flow continues to feed the jet after the circular wave has collapsed. The singularity of the wave collapse manifests itself in the initial sharp tip of the jet. With this, all of the above events are traced back to a single origin: The convergence of the flow as it enters into the tube.

7.1 Introduction

Liquid jets emerge when a relatively large amount of kinetic energy is imparted onto a small mass of liquid near a free surface. In this paper we will concentrate on the mechanism that produces the particularly intriguing 'tubular jet'.

[‡] See also: Raymond Bergmann, Erik de Jong, Jean-Baptiste Choimet, Devaraj van der Meer, and Detlef Lohse, *The tubular jet*, to be submitted to J. Fluid Mech.

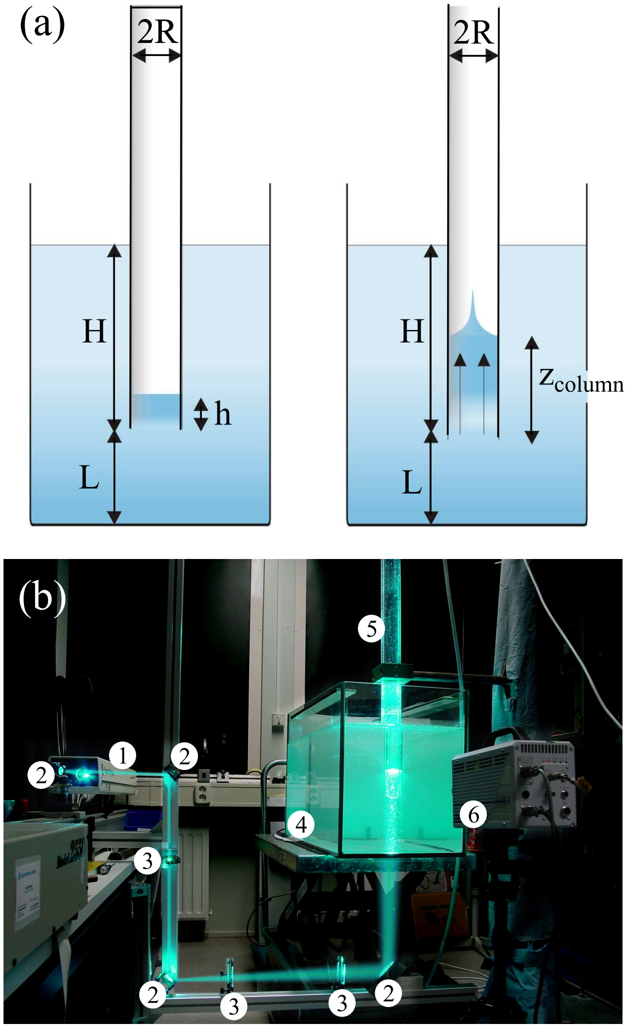

Figure 7.1: (a) Schematic drawing of the tubular jet setup, showing the main parameters of the experiment. Left: initial situation ($t < t_0$); right: during the rise of the column ($t > t_0$). (b) The experimental setup in the laboratory with its main components labelled. 1: Argon ion laser; 2: mirrors; 3: cylindrical lenses; 4: tank; 5: tube; 6: camera.

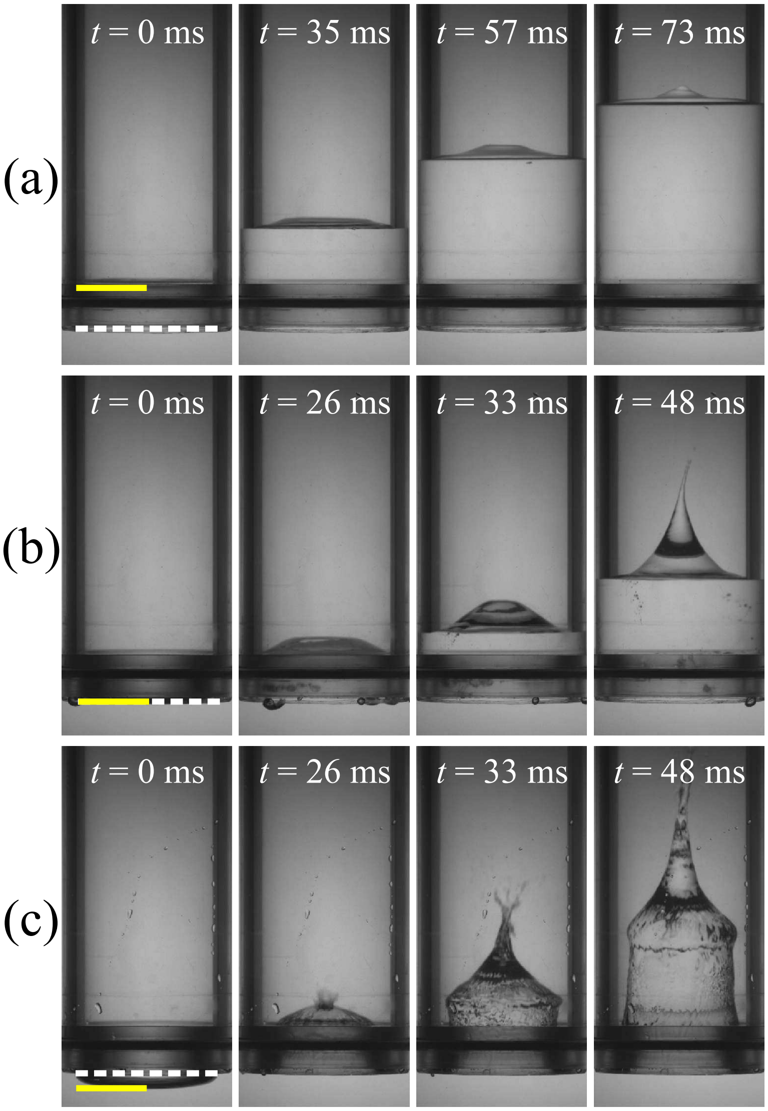

Figure 7.2: Different types of jets for meniscus heights $h = 14$ mm (a), $h = 0$ mm (b), and $h =$ -6 mm (c) in a pipe of inner radius $R = 25$ mm (see Fig. 7.1 (a)). The dotted white line indicates the bottom of the tube and the solid yellow line is the depth of the center of the initial meniscus;
$h > 0$ produces no jet, just a small mound of liquid in the center of the tube.
$h \approx 0$ produces a sharp jet.
$h < 0$ produces a detached rising water column, from which a strong jet erupts.
In all cases the distance L to the ground is much larger than R ($L \gg R$). The depth of H is 200 mm.

The tubular jet can be observed in a simple experiment in which a liquid rushes upwards to fill an initially pressurized, vertical tube partially immersed in a bath of fluid (see Fig. 7.1 (a)): As the liquid begins to rise in the tube after the pressure release, in some cases a jet can be seen to emerge from the center of the surface of the rising liquid column. Figure 7.2 (b) shows a typical example of such an experiment. This tubular jet was first reported by Lorenceau, Quéré, Ollitrault, and Clanet [1], in a paper that mainly focussed on the oscillating motion of the liquid column as a whole. Although the authors discussed some of the jet's properties, it remained unclear what the driving and focussing mechanisms for this jet are.

Mechanisms to focus momentum into a liquid jet are known to occur in great variety. Examples are the jet produced by the printhead of an inkjet printer, where a pressure wave in an open-ended channel is focussed on the free surface at the nozzle [2–4], or the jetting in a glass of champagne, where the surface tension stresses focus on the base of an unstable cavity at the surface and are released in a liquid jet [5, 6]. Also the jets produced by armor piercing weapons have been studied in detail [7]. In this case the focussing is found to be purely geometrical and the driving is provided by an explosive chemical reaction.

The jetting phenomena however that are closely related to the tubular jet are those created by what could be best described as geometrical flow focussing. An example is the collapse of a surface cavity formed by the impact of a droplet or object onto a fluid surface. Such a cavity collapses under the influence of hydrostatic pressure and a pressure singularity occurs as the sides of the cavity collide onto each other [8–11], which is subsequently released by the formation of an upward and a downward jet. A similar void collapse is even observed in granular materials [12–14], when a steel ball impacts on a bed of very fine, loose sand. After the "hydrostatic" void collapse, a jet of sand shoots up- and another one downward.

In this paper we will show that the origin of the tubular jet is similar to the geometrical flow focussing examples discussed previously, but with the considerable difference that the focussing geometry is now not provided by the topology of the free surface alone, but is in essence due to the tube wall partly obstructing the flow. Another distinct feature of the tubular jet is that we find the tubular jet to reflect the interplay of *several* flow focussing events instead of a single mechanism like was the case in all the aforementioned jetting phenomena.

In Section 7.2 we introduce the experiment and briefly discuss the relevant observations reported by Lorenceau *et al*, which serves as a starting point for the present investigation. Then in Section 7.3 we proceed to discuss our own experimental setup together with the experimental considerations. After this, in Section 7.4, we present results from particle image velocimetry experiments on the formation and closure of a surface cavity which precedes the jet eruption. In Section 7.5 we investigate the role of radial flow on the jet eruption by comparing three different experimental configurations. To further support our interpretation of the results, numerical potential flow calculations of the jet formation is presented in Section 7.6. In the concluding Section 7.7 we summarize our findings.

7.2 Dynamics of a liquid column

When the overpressure inside a circular tube of inner radius R is released and suddenly drops to the ambient level in the tank, the water column rises freely from its initial level h to the (eventual) equilibrium level at H (both measured with respect to the bottom of the tube, see Fig. 7.1 (a)). The initial height of the water column h is measured at the center of the tube and the depth of immersion H is the distance from the bottom of the tube to the ambient water level. Lorenceau *et al.* [1] derived expressions for the liquid column height $z_{column}(t)$ as a function of time by describing the rising liquid column in the tube as an oscillator with a continuously varying mass. For the initial rise in the time interval relevant for the development of the tubular jet ($t \ll 6\sqrt{H/g}$), $z_{column}(t)$ was found to be linear in time after a short period of initial acceleration (see Fig. 7.4 (a)). The constant rise velocity of the column was found to be

$$v_{column} = \frac{dz_{column}}{dt} = \sqrt{gH}\,, \tag{7.1}$$

with g the gravitational acceleration. It is stressed by the authors of [1] that all derivations hold only for $H \gg R$ due to the inclusion of entrance effects (dissipation by eddies).

As one starts with an initially empty tube, one would start off with a singularity, as the mass of the liquid column $m_{column}(t) \propto z_{column}(t)$ is 0 at t_0. This was recognized as an unphysical feature of the model, since there is always a mass of liquid underneath the tube entrance that must be accelerated. An entrance length z_0 was defined as a measure of this added mass at the tube entrance, giving $m_{column}(t) \propto z_{column}(t) + z_0$. The authors then proceeded to derive an equation to describe the initial acceleration stage of the rise and found

$$z_{column}(t) \approx h + \frac{gHt^2}{2(h+z_0)}\,, \tag{7.2}$$

which is valid for the very first instants of the rise, when $t\sqrt{gH} \ll h + z_0$ (see Fig. 7.4 (a)). The entrance length z_0 was found to be of the order of the inner radius of the tube R and not to depend on h.
calculated

It should be stressed that the above relations pertain only to the motion of the liquid column as a whole, and do not capture the motion of the jet itself. The authors did however make the following observations of the tubular jet: The maximum height reached by the jet was found to depend strongly on the initial level of the liquid in the column h; note that h will have negative values for a meniscus bulging out of the tube and positive values when the air/liquid interface is located inside the tube. The tubular jet was found not to form at all for positive values of h, in this case only a small mound of liquid has been observed at the interface, and for negative h, a strong increase in the height of the jet was found as h decreased. It was also stated that the jet forms after a short, but significant, delay of order $t = R/\sqrt{gH}$.

Mention is made of the existence of a 'liquid crater' on the surface of the rising column. In Fig. 7.3 (b) such a cavity can be clearly seen as a black ring due to the refraction of light through the curved shape of its rim. At the beginning of the rise, this circular cavity forms and closes onto itself. The propagation speed of the rim of this cavity was determined to be constant and the time needed to close the cavity was found to be equal to the time delay before jet eruption. When the tubular jet was absent, e.g. in the case of positive h, also the rim was not observed. The hypothesis of the authors of [1] was that the rim is related to a circular vortex which remains close to the entrance as the water flows into the tube. The objective of this paper is to check this hypothesis and, more generally, to shed light onto the formation and development of the jet.

7.3 Experiment

A schematic drawing and a picture of the setup we used for the investigation of the tubular jet can be found in Fig. 7.1 (a) and (b), respectively. A vertical, cylindrical perspex tube of inner radius R = 25 mm is partially

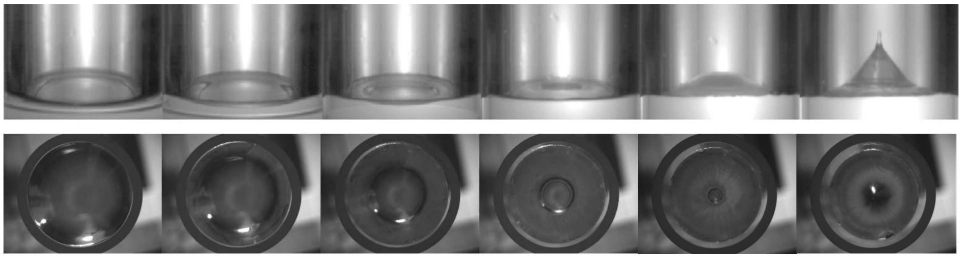

Figure 7.3: Top: Side view of the rim closure. Bottom: Rim closure seen from below. (bottom series similar to images in [1]). The time between consecutive frames is 6 ms and for both series the experimental conditions are: $R = 25$ mm, $L \gg R$, $H = 300$ mm, and $h = 0$ mm.

submerged to a depth H in a glass tank (dimensions 380 mm×780 mm×400 mm) which is filled up to a depth $H + L$ with demineralized water. L is the distance from the bottom of the tube to the bottom of the tank. Since all experiments discussed in this paper were performed with H between 0.025 and 0.35 meters, typical velocities for the rising water level are in the order of $\sqrt{gH} \approx 1$ m/s.

The top of the tube is connected to a compressed air line in order to control the initial meniscus depth h by pressurizing the air inside the tube. The top of the tube is also connected to an electromagnetic valve which, when opened, causes the pressure inside the tube to instantly drop to the ambient level: The diameter of the outlet hose and valve opening is large enough such that the air flow is hardly restricted as it leaves the tube.

The Reynolds number associated with pipe flow in the tube is

$$\mathrm{Re} = \frac{2R\sqrt{gH}}{\nu}\,, \tag{7.3}$$

where ν is the kinematic viscosity of water. Given the tube depths H of our experiments, the Reynolds number ranges between $2.5 \cdot 10^4$ and $9 \cdot 10^4$ and viscous effects in the flow can therefore be neglected for the main flow in the tube: The flow is dominated by gravity and inertia. Pipe flow is generally turbulent for $\mathrm{Re} > 4000$, so this system would be well within the turbulent domain. However, the flow is certainly not fully developed as it just enters the tube. For turbulent pipe flow, the entrance length is given by [15]

$$l_e/2R = 4.4(\mathrm{Re})^{1/6}\,, \tag{7.4}$$

from which we calculate that for our case l_e is of the order of 1 m, which provides a typical time scale for the flow development of about one second.

The turbulent flow suggested by the Reynolds number is clearly not yet developed on the time and length scales we are considering, namely those for the eruption of the tubular jet.

After the initial acceleration of the water column the Weber and Froude number associated with the pipe flow are given by We $= \rho g H R/\sigma$ and Fr $= H/R$. Here ρ denotes the density of water and σ the surface tension at the interface. For our experiments the effect of surface tension can be neglected on the large scale of the tube, since the Weber number ranges between $9 \cdot 10^2$ and $1.2 \cdot 10^4$. The Froude number ranges between 1 and 14, signaling that the pipe flow is indeed dominated by a balance of gravity and inertia.

As discussed in Section 7.2, we find that the initial depth of the center of the gas/liquid interface h, in other words the meniscus, has a profound effect on the jet. Fig. 7.4 (b) shows the strong dependence of the initial jet velocity v_{jet} on h.
This initial jet velocity is measured through highspeed imaging[*] in the first 5 ms after the jet erupts from the free surface (see Fig 7.4 (a)). Like the column velocity v_{column}, v_{jet} is found to scale with $\sqrt{gH}$, making it possible to collapse all velocity measurements for different H onto a single curve in Fig. 7.4 (b).

The influence of h can be classified into three different regimes:

- For an initial meniscus sufficiently inside the tube ($h > 0$, Fig. 7.2 (a)), the jet speed is of order $\sqrt{gH}$, in other words, $v_{jet} \approx v_{column}$. This corresponds to the horizontal asymptotic value of 1 in Fig. 7.4 (b). There is no jet, only a mound on the water surface. The rim seen in Fig. 7.3 (b) is also absent here.
- For an initial meniscus flush with the bottom of the tube ($h \approx 0$, Fig. 7.2 (b)), a rim is observed and a jet erupts shortly after the acceleration stage of the water column rise.
- For an initial meniscus bulging sufficiently out of the tube ($h < 0$, Fig. 7.2 (c)), the flow at the tube entrance cannot follow the 90 degree

---

[*] Outside of the tank a high speed camera is set up approximately level with the bottom of the tube, perpendicular to the glass sidewall of the tank. For the imaging of the experiment, a Kodak CR2000 CCD camera is used at a frame rate of 1000 frames per second and a resolution of 512x384 pixels. Backlighting of the tube is achieved by a halogen lamp with a diffusive plate placed at the opposite side of the tank to obtain typical images like those of Fig. 7.2 (a).

corner of the tube's inner edge, causing the rising column to separate from the inside wall of the tube. A very strong jet is formed at the top of this detached water column, contributing to the steep rise in the jet velocity plot Fig. 7.4 (b) for negative h. By softening the edge of the tube the separation can be partly suppressed.

In the remainder of this paper we will focus on experiments with the initial meniscus being flush with the bottom of the tube ($h = 0$), since in this case we both have a clear tubular jet and we are unhindered by the possible separation of the inflowing liquid from the inner wall of the tube as is common for $h < 0$. Looking at this regime will not limit the generality of our observations on the tubular jet, but will facilitate the comparison between the different flow configurations introduced in the later sections of this paper.

7.4 Formation and closure of the rim

Although the rim (Fig. 7.3) is observed whenever the tubular jet forms *and* the jet eruption and rim closure are always simultaneous, it is not a priori clear that this rim is a prerequisite for jet eruption. To investigate this, we will try to unravel the origin and nature of this rim by answering the following questions:

- Is the rim due to the initial capillary uprise of the meniscus detaching and travelling over the free surface?
- Does the rim propagate like a capillary or gravitational surface wave?
- Do entrance vortices cause the rim to form and propagate?

7.4.1 Is the rim due to the initial capillary uprise of the meniscus detaching and travelling over the free surface?

Due to the wetting properties of perspex, the initial air/water interface inside the tube curves *up*, when the distance to the inner wall is below the capillary length. As the gas pressure inside the tube is released and the interface starts to accelerate upwards, this initial curvature of the interface could detach and travel over the surface as the rim.

To check wether the rim closure is indeed simply an inward propagation of the capillary uprise, we applied a small amount of vaseline to the tube

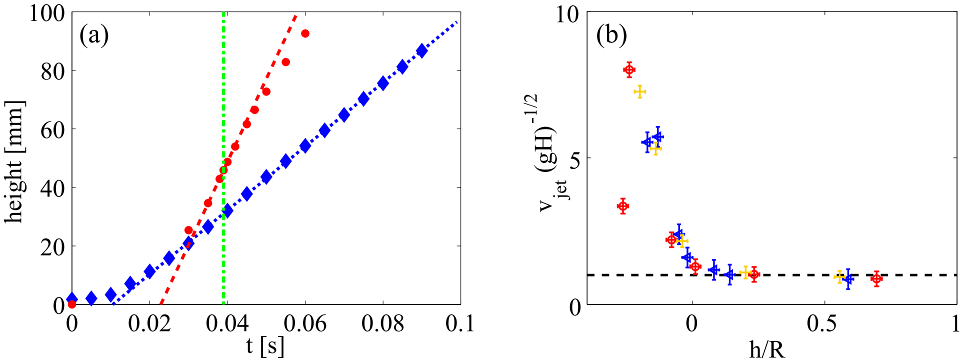

Figure 7.4: (a) The height of the water level in the tube z_{column} (blue diamonds) and the height of the jet (red dots) as a function of the time that has passed since the release of the overpressure in the tube for the conditions $R = 25$ mm, $L \gg R$, $H = 150$ mm, and $h = 0$ mm. The data we obtained by highspeed imaging at 1000 frames per second. The vertical green line indicates the moment of the jet eruption. Since the jet height is defined as the height of the center of the interface, it can exceed the column height before the actual moment of jet eruption, due to the rising rim. To determine the column and jet speed, v_{column} and v_{jet} respectively, a linear fit is made to the column data (blue line) after the instant of the jet eruption and a linear fit to the jet height (red line) during the first 5 ms of the jet's existence.

(b) The jet velocity v_{jet} non-dimensionalized by the velocity of the rising column $\sqrt{gH}$ as a function of the initial meniscus depth h normalized by the radius of the tube R for the conditions of $R = 25$ mm, $L \gg R$, and H has three different values (blue triangles: $H = 150$ mm, red circles: $H = 200$ mm, yellow crosses: $H = 250$ mm). v_{jet} was obtained using the procedure described in (a). The dashed black line indicates $v_{jet}/\sqrt{gH} = 1$.

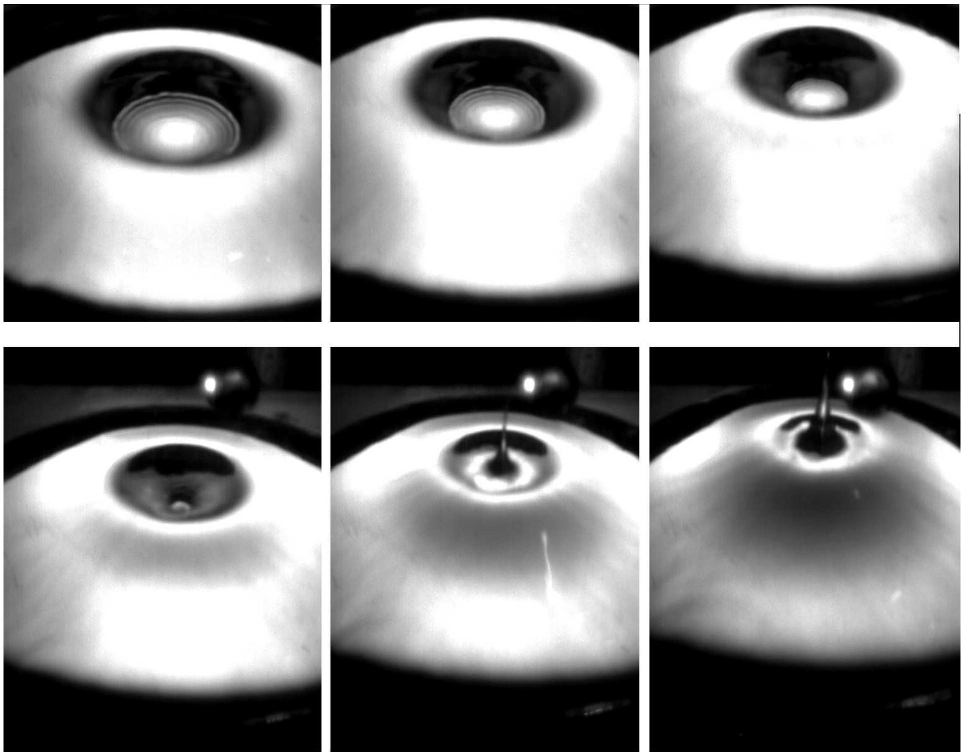

Figure 7.5: A series of images of the rim closure viewed from above at an angle for the conditions of $R = 25$ mm, $L \gg R$, $H = 200$ mm, and $h = 0$ mm. The rim moves as a wall of fluid over the undisturbed inner region of the interface, like a hydraulic jump [16]. The jet is initiated when the bottom of the fluid wall reaches the center. Time between images is 1 ms.

entrance. This alters the contact angle between the interface and the tube, and will curve the interface *down* near the inner wall of the tube. However, using such a hydrophobic tube entrance, the rim still formed and collapsed at the same constant velocity as was found for the regular case. The rim can therefore not be attributed to the detachment and propagation of the capillary uprise of the liquid at the wall.

7.4.2 Does the rim propagate like a capillary or gravitational surface wave?

The nature of the rim could possibly reveal the mechanism by which it is produced. Therefore we made direct observations of the rim with a highspeed camera, to investigate whether it can be attributed to an initial disturbance which travels as a capillary or gravitational surface wave towards the axis of the tube.

Based on Fig. 7.3 it seems plausible to presume that the wave is a capillary or gravitational surface wave, but in these recordings, the camera was positioned horizontally and the fluid interface itself obscures largely what is happening at the center of the fluid cavity. So, in order to make more revealing recordings, the high speed camera is now mounted at an angle above the setup to allow us to view what actually happens inside the cavity as it collapses. The frames of Fig. 7.5 show these tilted recordings. The first striking observation from Fig. 7.5 is that the rim moves into a flat inner region of the interface with a steep front, more reminiscent of a hydraulic jump or bore instead of the smooth front expected for a surface wave. The second observation is that in the first two frames of Fig. 7.5 the rim, roughly 1 cm or larger, is preceded by small capillary waves with wavelengths λ smaller than 3 mm. These waves are observed from the start of the column rise, but are ‘overtaken’ by the rim (third frame). This also contradicts the wave being a capillary or gravitational wave, since these smaller capillary waves should propagate faster than a 1 cm gravitational wave (see Appendix A).

Based on these two observations on the shape and propagation velocity of the rim, it can be concluded that the rim is not propelled by gravitational or surface tension forces. There must therefore be a different propulsion mechanism for the rim.

7.4.3 PIV experiments: Do entrance vortices cause the rim to form and propagate?

Since the rim does not propagate like a surface wave, could it be the vortex, located at the entrance of the tube, driving it as was proposed by the authors of [1]? As the column starts to rise, the entrance vortex could deflect the fluid above it outwards, towards the wall of the tube, forming a rim. This effect would weaken as the surface moves away from the entrance vortex, causing the rim to move inward. To investigate this possible effect of the entrance vortex, high-speed Particle Image Velocimetry (PIV) is applied.

To perform the PIV measurements, the fluid is seeded with small Dantec Dynamics polyamid tracer particles of radius 25 μm and density 1030 kg/m^3 that will follow the flow. A laser sheet shines through the fluid, creating an illuminated plane inside the flow. The light scattered by the tracer particles is captured by a high speed camera at a frame rate of 1000 frames per second and a resolution of 1280x512 pixels (see Fig. 7.1 (b)). This series of images is then correlated by multipass algorithms, using DaVis PIV software by LaVision, in order to determine the flow field in the liquid over a two dimensional area for extended periods of time. The correlation was performed in three passes at sub-pixel accuracy, using 64x64 pixels, 32x32 pixels and 16x16 pixels interrogation windows. The windows overlap by 50%, resulting in one velocity vector every 8x8 pixels.

For the illumination of the high speed PIV measurements we use a Spectra Physics Stabilite 2017 Argon Ion laser, which outputs continuously at a wavelength of 514.5 nm. Using this continuous laser, the frame rate of the recording camera determines the number of field measurements per second. Power output is an important consideration, because short exposure times are preferable, to prevent motion blurring of the particle images. Using the laser at its full 6 Watt power output allowed for an exposure time of 0.1 ms. With a typical flow velocity of 1 m/s and an image scaling of 10 pixels/mm the particle images will not move more than one pixel during the exposure, so this blurring effect is minimal. The laser beam is converted into a light sheet by means of three cylindrical lenses. In the experimental setup, the light sheet is oriented vertically, in order to illuminate the flow from below (Fig. 7.1 (b)). We found this to be preferable as compared to a horizontally oriented light sheet shining through the side of the tube, because a horizontally aligned light sheet is reflected many times inside the tube, causing a bright glare near the sides. Moreover, the main flow direction is oriented vertically, so a horizontally oriented light sheet would have to be of considerable width ($\sim$ 100 mm) to fully illuminate the area of interest.

From these high speed PIV measurements one obtains typical images of the velocity field like Fig. 7.6. In this figure the image of the original high speed recording is overlaid with the obtained PIV results. The PIV software also produces velocity vectors at the free surface and even inside the jet, but these vectors are highly inaccurate, due to the large optical

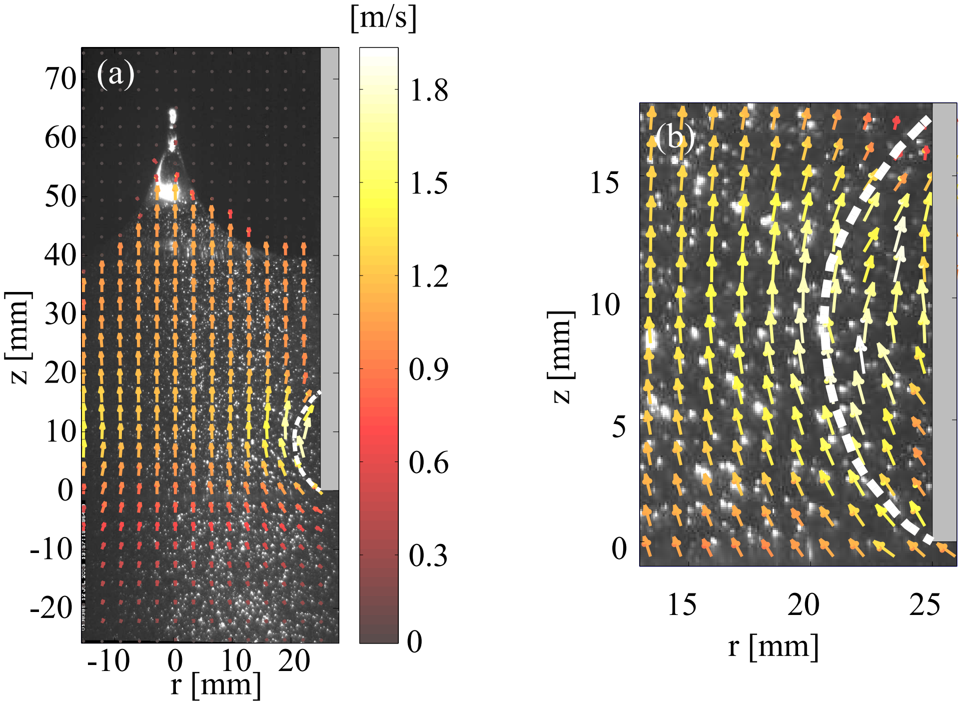

Figure 7.6: The time is $t = 50$ ms after the pressure release and at that time the column has reached a height of about 40 mm and the jet has just erupted. The experimental conditions are $H = 150$, $L \gg R$, and $h = 0$ mm. The velocity field obtained by PIV overlaid on the original high speed recording. For clarity, only one sixteenth of the measured vectors are shown in (a) and one fourth in (b). The shaded area on the right depicts the tube wall and the recirculation zone is indicated by the stream line originating at the inner edge of the wall (dashed white line). The region of the vortex is enlarged in (b).

distortions caused by the curvature of the air/water interface and are thus not shown.

A vortex is visible at the entrance of the tube in Fig. 7.6 (a) and enlarged in Fig. 7.6 (b). The velocity gradients in the interior of this vortex are large[†], but can be resolved by our experimental setup. There is however no need to do so, because only the edges of the vortex and not its internal structure are of interest, since this is a measure of whether the vortex is close enough to the free surface to produce the rim. The size of the recirculation zone is indicated by the dashed white line which is the stream line originating at the inner edge of the tube. During the rise of the water column, the entrance vortex stretches in the radial r and the axial z direction. However in the beginning, when the water column starts to rise and the rim is formed, the vortex is still absent. Later, as the vortex is fully developed like in Fig. 7.6, it lags considerably behind the column height.

Figure 7.7 (b) shows the vortex growth from a different perspective. Here the radial flow velocity component v_r at a certain distance $\triangle z$ below the rising interface Fig. 7.7 (a) is plotted as a color plot. The position at which the profiles are monitored is moving upward with the free surface at a fixed distance $\triangle z = 4$ mm. The blue colors represent negative v_r (directed towards the $r = 0$ -axis). We observe a strong inward directed radial flow near the white line, which indicates the radial position of the rim, assuming a constant velocity of closure. The white dot indicates the moment of jet eruption. The radial flow near the closing rim originates at the pipe's bottom edge and spreads into and up the pipe over time. The rim seems to be 'pushed along' by this inward flow directly beneath it. The rim propagation can therefore not be described purely as a travelling cylindrical wave; bulk flow effects dictate its movement.

A second observation is that the region of outward directed flow is positioned far away from the rim and only develops after the rim has passed. The rim can therefore not be formed by the deflection of fluid towards the pipe wall by the entrance vortex as hypothesized and dismissed before. It seems that the vortex does not play any significant role in the creation or propagation of the rim.

[†] A closer investigation of the vortex by PIV revealed velocity gradients $\Delta v/\Delta x$ as large as $6 \cdot 10^2$ s$^-1$.

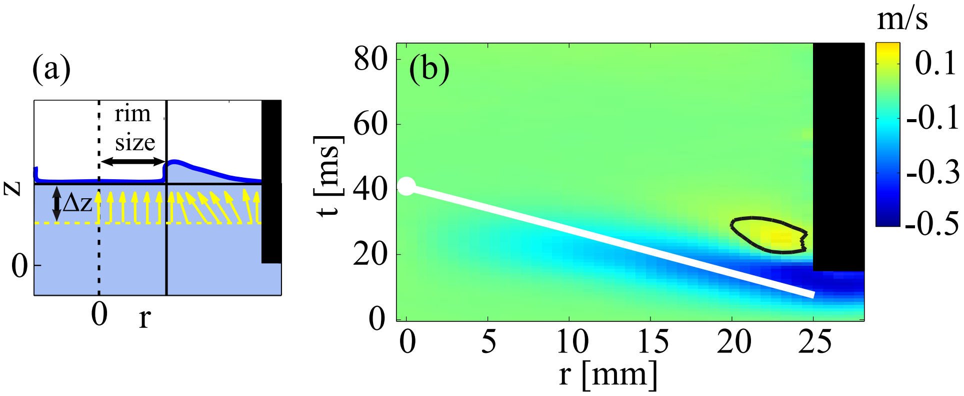

Figure 7.7: (a) schematically shows that the position at which the flow velocity is monitored in (b) is moving upward with the free surface at a fixed distance $\triangle z$. (b) shows the radial flow velocity component v_r at a distance $\triangle z = 4$ mm below the rising interface. The radial velocity components are plotted as a color plot. The blue colors represent negative v_r (directed towards the $r = 0$ -axis). We observe a strong inward directed radial flow near the white line, which indicates the radial position of the rim. The white dot indicates the moment of jet eruption. The radial flow near the closing rim originates at the pipe's bottom edge and spreads into and up the pipe over time. The rim seems to be 'pushed along' by this focussing flow flow directly beneath it. The focussed flow vanishes at the center of the tube $r = 0$ mm.
The region of outward directed flow, whose boundary is indicated by the black solid curve of $v_r = 0$, does not influence the rim closure as it is positioned far away from the closing rim. $R = 25$ mm, $L \gg R$, $H = 150$ mm, and $h = 0$ mm.

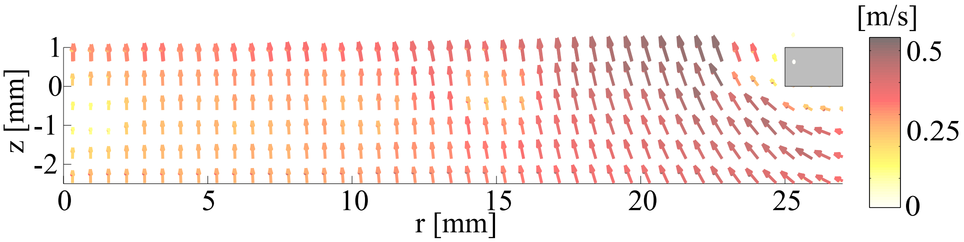

Figure 7.8: The velocity field obtained from PIV measurements at the pipe entrance for $H = 150$ mm, 10 ms after the pressure release. The gray shaded area on the right indicates the location of the pipe wall. $R = 25$ mm, $L \gg R$, and $h = 0$ mm.

7.4.4 The origin of the rim

In the previous three subsections we have seen that the rim cannot be explained by the initial curvature of the meniscus, a capillary or gravitational surface wave, nor the vortex at the entrance of the tube. So what *can* explain the rim formation?
To answer this question we look at the development of the flow at the pipe entrance in the initial instants of the column rise, since this is where the radial flow 'pushing' the rim seemed to originate.
Figure 7.8 shows the flow in the experiment at the pipe entrance 10 ms after the pressure release. The data represents an average of 4 separate PIV experiments. It is clear that there is a stronger inflow of fluid near $r = R$ on the time scale for the creation of the rim. For this depth H of 150 mm the time scale on which the rim fully develops and starts to move radially inward is 10 ms. The distance of the free surface to the entrance of the pipe at that time is only 2 mm. The enhanced axial flow will thus influence the shape of the free surface and produce the rim.

We call this purely geometrical effect of the pipe wall forcing the axial and radial flow into the pipe and necessarily speeding it up in the process *the funnelling effect*. This enhancement of flow along the inner-edge of the pipe might at first seem somewhat counter–intuitive. But even in a simplified configuration with a stationary, radial flow, such an enhancement along the pipe wall arises naturally, as will be show in Section 7.6.

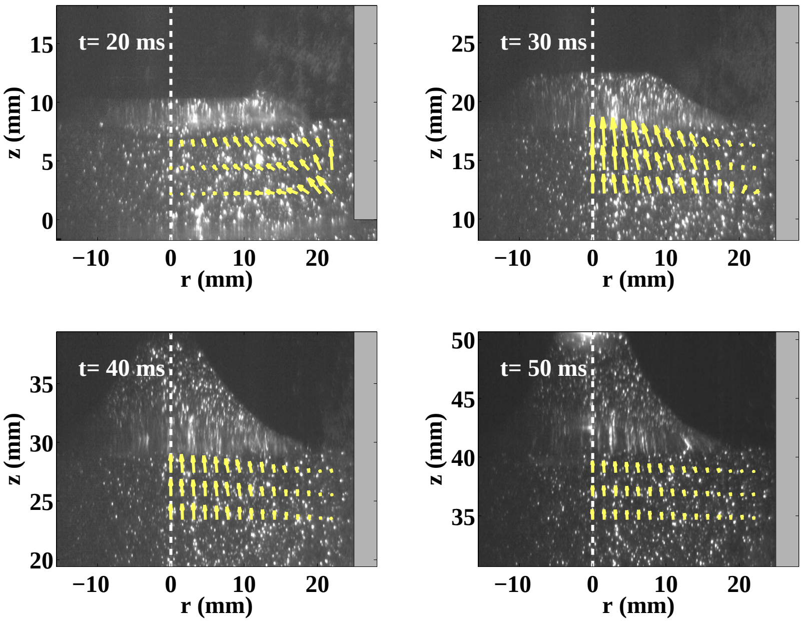

Figure 7.9: The bulk flow inside the tube. The gray shaded area on the right is the pipe wall. v_{column} has been subtracted from the velocity data obtained by PIV, so the yellow vectors indicate the flow relative to the bulk column speed. The largest vector in the top right figure has a magnitude of 0.3 m/s; the vectors are scaled linearly. $R = 25$ mm, $L \gg R$, $H = 150$ mm, and $h = 0$ mm.

7.5 Investigating the role of the radial flow

Due to symmetry, the radial component of the flow directly underneath the free surface obviously must vanish at $r = 0$. It is conceivable that due to continuity, this vanishing inward radial flow gives rise to a nonzero axial flow on top of the main axial flow component v_{column}. This induced (extra) axial flow would locally push up the interface.

To visualize this effect, the column velocity v_{column} is subtracted from the results obtained by the PIV measurements. From Fig. 7.9, showing the relative motion of the fluid to the bulk column motion, we clearly observe the flow from the bulk into the jet for various times. In Fig. 7.9 it is clear that, after the formation of the rim at $t > 30$ ms, the axial component of

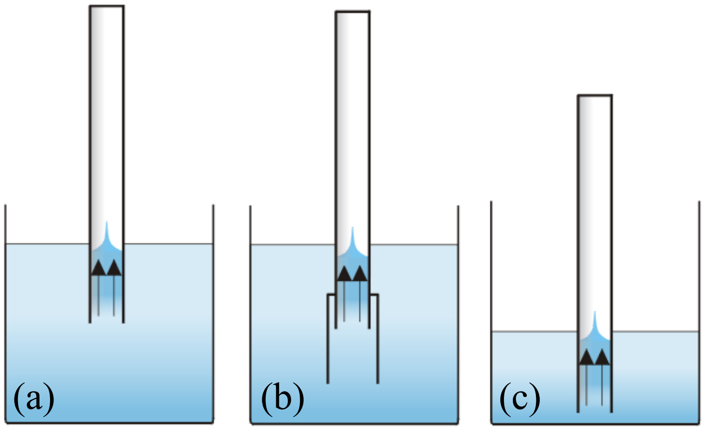

Figure 7.10: Three different types of flow situations. (a) normal flow, (b) reduced radial flow, and (c) enhanced radial flow.

the flow is increased around $r = 0$ and the interface is pushed upwards in the center of the tube. The mound we see in Figs. 7.3 and 7.5 is thus not just the increasing amplitude of the inward travelling cylindrical wave, it is also an effect of the radial flow beneath it. We also see that there is a continuous flow of fluid from the bulk into the jet. This flow is strongest before the eruption of the jet, when we see the rising mound on the interface.

To experimentally determine the influence of this effect we devised a method to enhance and reduce the relative importance of the radial inflow in the experiment. Reduced radial inflow is obtained by placing a second, larger pipe around the first, thus locally blocking the flow in the radial direction (Fig. 7.10 (b)). Enhanced radial inflow is achieved by simply positioning the tube very close to the bottom, such that the axial inflow is obstructed (Fig. 7.10 (c)). Both are discussed in more detail below.

Reduced radial inflow. By placing a second, larger pipe around the entrance of the main pipe, the radial inflow into the tube is reduced (Fig. 7.10 (b)). The second pipe (inner radius of $R_s = 35$ mm) extends twice its radius below the main pipe's entrance, so its entrance effects (e.g., entrance vortex) do not influence the flow into the main pipe. Since the liquid still starts with a meniscus at the main pipe and the fluid is flowing through a contraction at the main pipe's entrance, there will still be a certain amount of radial inflow, though strongly reduced with respect to

the 'normal' situation.
Apart from the shape of the meniscus, this situation is similar to the case of $h \gg 0$, if $R_s \approx R$, where we already observed that neither a jet, nor a rim is formed.

Enhanced radial inflow. Now the pipe entrance is placed very near to the bottom of the tank, relatively enhancing the effect of the radial inflow by blocking the inflow in the axial direction (Fig. 7.10(c)). Since the entrance depth z_0 is of order R, we must take $L < R$ to significantly increase the radial flow component.
The precise value for L suitable for this setup can be determined by experimentally investigating the influence of L on the rise velocity of the water level v_{column} and the jet velocity v_{jet}. From the highspeed camera recordings (see Section 7.3) we observe that the jet velocity is indeed significantly affected by decreasing L below R. While the jet velocity increases, the column velocity decreases for $L < R$. When L is decreased below $L = \frac{1}{5}R$ for this setup, the rising water column detaches from the inside of the pipe. Even though this detachment is generally seen for $h < 0$, for such small values of L already for $h = 0$ the enhanced radial flow does not follow the inner corner at the tube's entrance any more . This phenomenon would make quantification and comparison with other experiments difficult. Therefore $L = \frac{2}{5}R$ (10 mm) was chosen as a suitable value for the radially enhanced flow experiments, since its effect on the jet speed is still considerable and detachment of the water column did not occur.

We will first discuss how the radial flow influences the rim, after which the influence on the jet itself will be discussed. In the experiments the strength of the radial inflow influences the shape of the cavity. The cavity is deeper and the rim is steeper for the radially enhanced flow, whereas the cavity is much less prevalent (though not completely absent) in the case of the radially reduced flow (see Fig. 7.11). This is also reflected in the flow field at the entrance of the tube. A strong 'funnelling' effect, like previously observed in Fig. 7.8, can be seen to occur in the radially enhanced experiment. In the case of the radial reduced flow this effect seems to be, just like the rim, largely absent.

The propagation mechanism for the rim, the fluid flow directly under the free surface, also exhibits a strong dependance on the radial flow component. In the case of radially enhanced flow, the v_r component pushing the rim along is stronger compared to the normal flow situation (Fig. 7.7 (b)). In the case of radial obstructed flow however, this mechanism

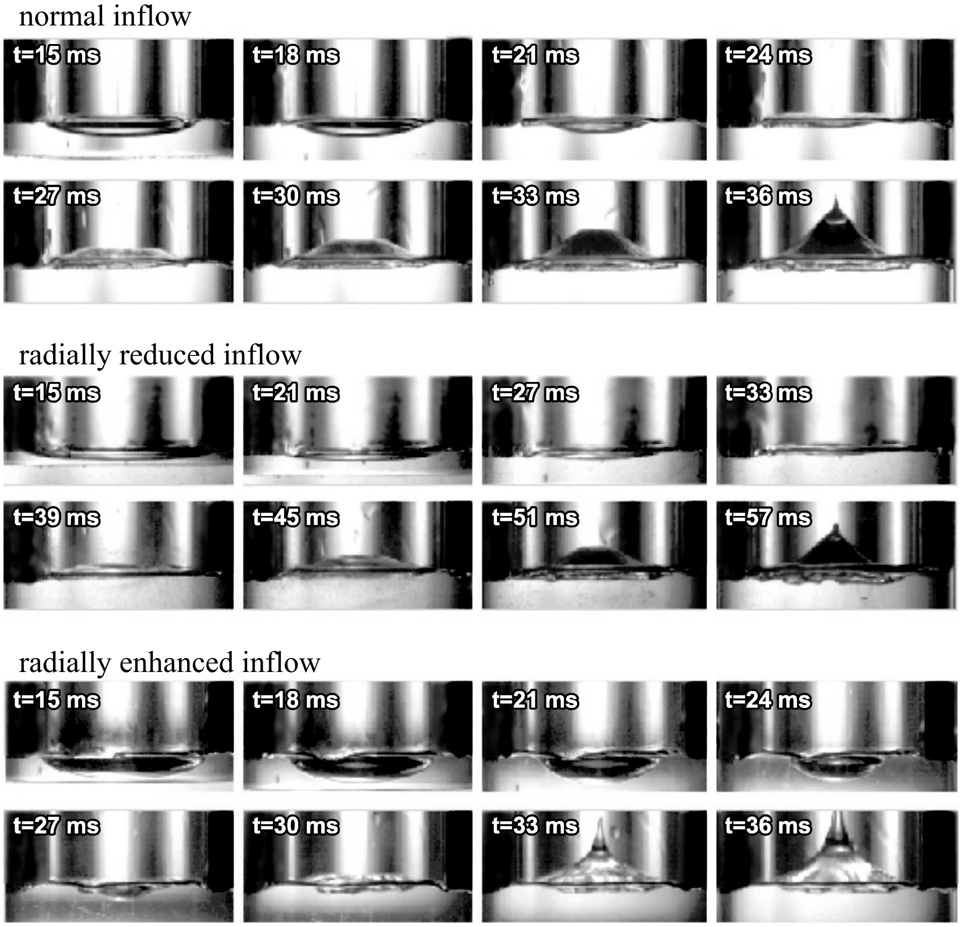

Figure 7.11: Close up view of the closing rim for normal (top), radially reduced (middle), and radially enhanced (bottom) flow, the rim is much more pronounced for stronger radial flows. See text for the exact values of the geometry. Time between images is $\Delta t = 6$ ms for the top series, $\Delta t = 3$ ms for the middle and bottom series. $R = 25$ mm, $L \gg R$, $H = 175$ mm, and $h = 0$ mm; first image of each series at $t = 15$ ms.

is observed to be considerably weakened. As a result, the rim propagates at a slower velocity and closes much later than it does for the normal and enhanced radial flow experiments, e.g., at a depth H of 175 mm, 57 ms versus 36 ms.

These experiments thus underline our earlier observations about the rim, namely as being created by the 'funnelling' effect at the entrance of the tube and being pushed along by the inward radial flow directly under the interface. Both effects become stronger by enhancing the radial flow component in the entrance flow.

Now turning to the jet creation, the radially obstructed flow produces much weaker jets. Due to the slower rim collapse, the jet also erupts later when compared to the normal and radially enhanced case. The jets produced by the radially enhanced flow are comparable in height to the normal case, even though the total flow of liquid into the pipe is restricted (the water column rises considerably slower).

In Fig. 7.12 (a) the ratio of the measured rise velocity v_{column} and the expected rise velocity $\sqrt{gH}$ is plotted against the immersion depth H/R of the column. It is seen that the expected rise velocity is only reached for the considerable depth of $H > 10R$ in the case of the normal flow configuration. The flow in the two altered setups is restricted to lower values for v_{column} compared to the unaltered case. Therefore, for a better comparison of the three different flow configurations, we normalized the jet velocities by v_{column} instead of $\sqrt{gH}$ in Fig. 7.12 (b). The radially enhanced setup consistently produces the strongest jets, even though the total fluid flux into the tube is restricted. The radially obstructed setup on the other hand, produces weak jets. The normalized jet speeds seem to level off for $H > 10R$ (250 mm) and scale with $v_{column} \propto \sqrt{gH}$ in this limit.

We conclude that enhancement of the radial flow strongly enhances the erupting jet. The enhanced radial flow setup has a stronger radial flow and collapse, and subsequently, a stronger axial flow feeding the jet after the rim collapse. This is all in good agreement with the mechanism of rim and jet formation outlined in the previous section.

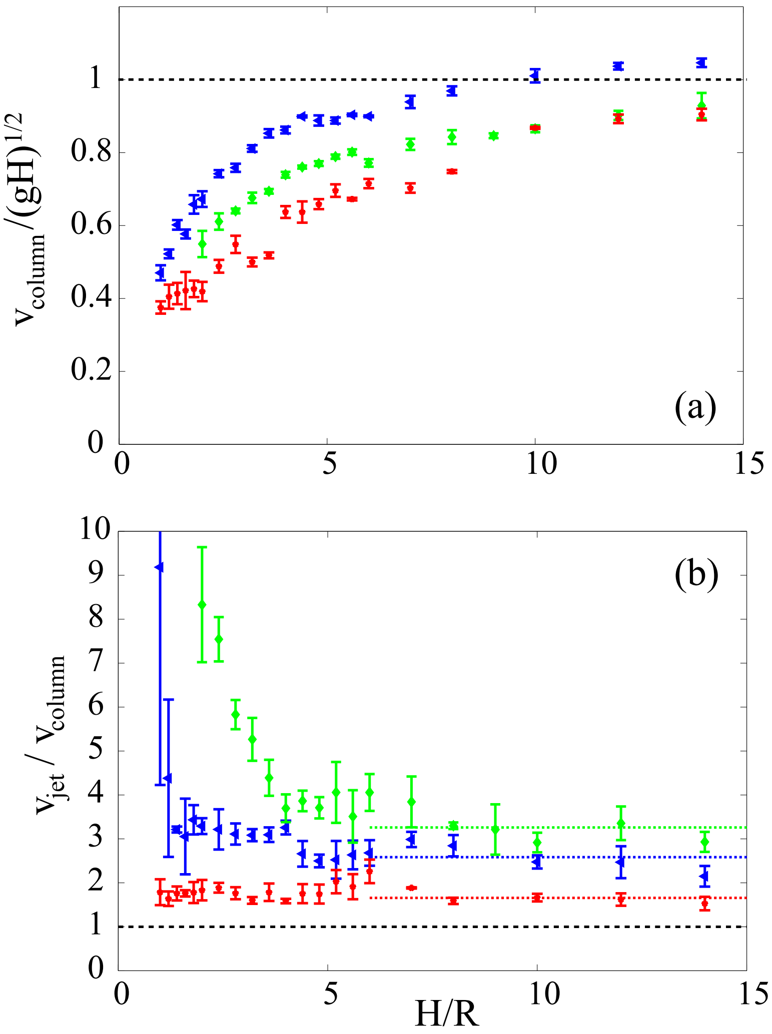

Figure 7.12: The influence of the radial flow on the jet and column velocities (see Fig. 7.10). The radially reduced flow configuration (red stars) and the radially enhanced flow configuration (green diamonds) compared to the normal flow situation (blue triangles). (a) Column speed for the different radial flows. Only as the depth H increases, v_{column} tends to $\sqrt{gH}$.
(b) v_{jet} normalized by v_{column}. As the radial flow is enhanced the jet velocity is found to be considerably larger as compared to v_{column}. For larger depth H the ratio v_{jet}/v_{column} tends to a constant. $R = 25$ mm, $L \gg R$, and $h = 0$ mm.

7.6 Potential flow analysis

To further support our findings and corroborate that (i) the funnelling effect is generic to the geometry and (ii) that vorticity indeed plays no role for the creation of the tubular jet, we have performed a potential flow analysis. In a first step we analyze the flow just after the release of the pressure in the tube (Subsection 7.6.1), in the following subsections we will present a full analysis of the problem (Subsections 7.6.2 and 7.6.3). For the second investigation the exact geometry of the problem is taken into account, including the moving free surface, making it necessary to solve the potential numerically by means of a boundary integral simulation [17].

7.6.1 The funnelling effect

To confirm that the funnelling effect is indeed generic to the geometry (Section 7.4.3), we performed a potential flow analysis of a simplified configuration with a stationary, radial flow at the pipe entrance. In the introduction the Reynolds number was said to be considerable and the funnelling effect develops rapidly compared to the time scale for the development of vorticity, so in good approximation, the initial flow can be described by potential theory. The potential of the flow φ is solved analytically in Appendix B for boundary conditions which are, albeit simplified, comparable to our experiment (cf. Fig. 7.13 (a)). Figure 7.13 (b), (c), and (d) show the flow and potential obtained for an inflow similar to the one in the experiments reaching to a depth of order R below the tube ($L = R$). In Fig. 7.13 (b) and (d), a clear enhancement of the axial flow at the pipe wall can be observed. So even for this simplified and purely radially driven example the funnelling effect arises naturally.

7.6.2 Boundary integral simulations

To verify that vorticity plays no role for the creation of the tubular jet, we performed boundary integral calculations. Since the exact geometry of the problem is now taken into account, including the moving free surface, the same potential flow formulation of Appendix B is solved numerically. The moving free surface is iteratively solved over time using the standard kinematic and dynamic boundary conditions [18–21]. In Section 7.3 we found that the initial state of the system, namely the meniscus, has a profound effect on the tubular jet. So, as a prerequisite for obtaining realistic simulation results, we first have to accurately capture this initial condition.

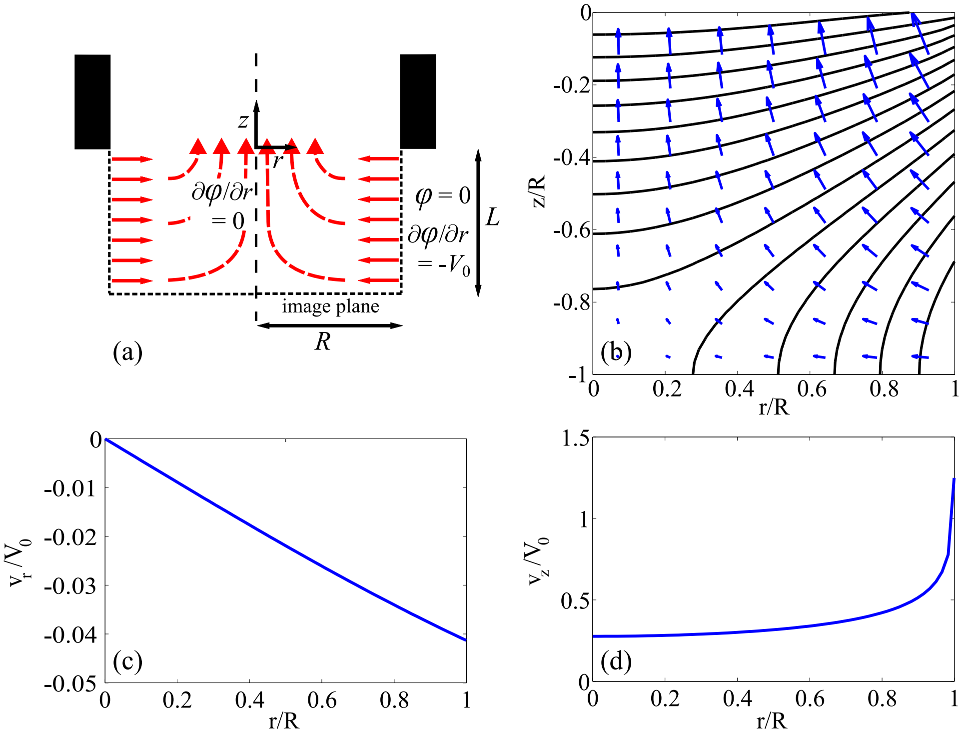

Figure 7.13: (a) The initial conditions for the flow potential φ, which mimics the radial flow of our experiment. These boundary conditions assume a constant radial inflow of strength V_0 to a depth L below the tube (solid arrows). The expected flow is drawn as dashed arrows.
(b) shows the potential and flow given by the configuration of figure (a). The potential φ is obtained by Eq. (7.10) and is indicated by the isolines. The flow direction and strength obtained by Eq. (7.11) and Eq. (7.12) are given by the arrows.
(c) and (d) show the radial and axial flow component, v_r and v_z respectively, at the entrance of the pipe ($z = 0$) obtained by Eq. (7.11) and Eq. (7.12) for the flow configuration of figure (a). Clearly, the axial flow is enhanced along the wall.

In order to obtain the shape of the meniscus for the numerical calculations, we use the Young-Laplace equation [22] to describe the shape of the liquid-gas interface in equilibrium,

$$P_{water} - P_{air} = \frac{\sigma}{R_c}, \tag{7.5}$$

where P_{water} and P_{air} are the pressures at the air–water, σ is the surface tension, and R_c is the local radius of curvature of the interface. The hydrostatic pressure in the water is defined as $P_{water} = \rho g(H - z)$ and as long as the surface is flat at $r = 0$ (this is the case for R sufficiently larger than the capillary length), the air pressure inside the tube is given by $P_{air} = \rho g(H - h)$. The air–water interface is represented as an axisymmetric surface described by a revolution of the curve $r(z)$. This curve has endpoints at $[0, R]$ at the inner wall of the pipe and $[h, 0]$ on the z-axis. The radius of curvature at any point (r, z) on such a surface is given by

$$\frac{1}{R_c} = \frac{\frac{d^2r}{dz^2}}{\left[1 + \left(\frac{dr}{dz}\right)^2\right]^{3/2}} + \frac{1}{r\left[1 + \left(\frac{dr}{dz}\right)^2\right]^{1/2}} . \tag{7.6}$$

Combining Eq. (7.5) and Eq. (7.6) one obtains an ODE which must be solved numerically using a shooting method, because the two boundary conditions are defined at two different ends,

1. $r(0) = R$; the interface must meet the pipe's inner edge,
2. $r(h) = 0$; the meniscus depth is h.

In this way a meniscus shape is obtained which is in excellent agreement with the experimentally observed meniscus shape, as can be seen in Fig. 7.14. This numerical meniscus shape will be used as the initial condition in our boundary integral simulations.

7.6.3 Comparison between boundary integral simulations and experiments

When comparing the boundary integral simulations to experiments under the same conditions, including the same initial meniscus-shape and -depth, we find the water column to rise more quickly in the numerical calculations as compared to the experiments. In both cases the rise velocities dz_{column}/dt tend to the same constant velocity, but the initial acceleration of the water column in the numerical calculations is considerably higher. This difference in acceleration could be due to a difference in the global flow structure, because in the numerical calculations only the bottom wall of the tank is taken into consideration and the side walls of the tank are neglected. These

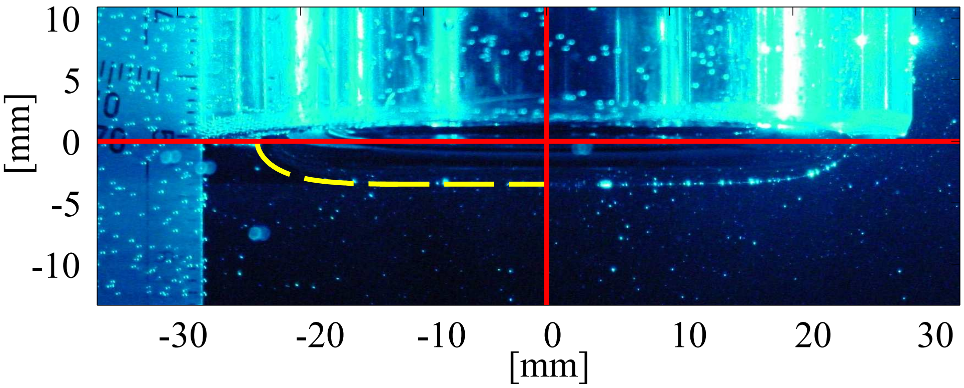

Figure 7.14: Comparison of the meniscus obtained by the shooting routine with the meniscus observed in the experiment. The numerical solution (dashed yellow line) is overlaid on the left half of a photograph of the meniscus ($h = -3.5$ mm, $R = 25$ mm). The interface in the photograph is illuminated by a laser sheet and can be seen in the right half.

side walls could be included in the calculations by introducing them as image planes, and subsequently introducing four more tubes into the numerical calculations, however this becomes numerically expensive and this three–dimensional configuration would be hard to achieve in our axisymmetric calculations.

The tubular jet however depends only on local flow structures, namely the funnelling effect at the pipe entrance and continuity at the center of the pipe. Therefore, we can simply compensate for the increased rising of the water column and still find an excellent agreement between the numerical calculations and the experiments, as is shown in Fig. 7.15. Also the time for the eruption of the jet is faithfully reproduced in the numerics.

In the numerical calculations we observe the same funnelling effect along the edge of the pipe generating the cavity, which is clearly visible in Fig. 7.15 (b) and (c). The propulsion of the rim by the radial flow is also observed, including the rising of the center mound and eruption of the jet at exactly the same time as compared to the experiment (Fig. 7.15 (d) and (e)). Since vorticity is neglected in this potential flow calculation, we again conclude that indeed vorticity does not influence any of the mechanisms leading to the eruption of the tubular jet.

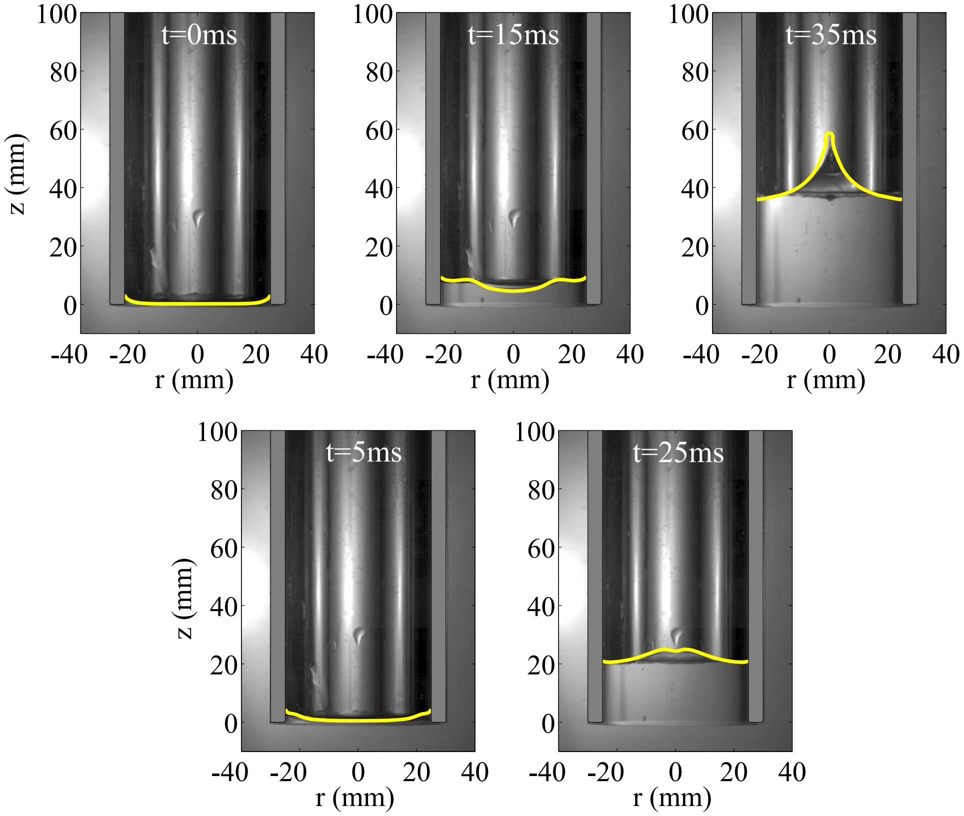

Figure 7.15: The experiments (snapshots) overlaid by the numerical result (yellow line) for the free surface at different instances in time. The tube wall used for the numerical calculation is indicated by the gray shaded area. The height of the numerically obtained free surface is adjusted to compensate for the faster rising of the liquid column in our numerical calculations. The shape and time evolution of the shape of the numerically obtained free surface is shown without any adjustment. $R = 25$ mm, $L \gg R$, $H = 300$ mm, and $h = 0$ mm

7.7 Conclusions

We investigated the origins of the tubular jet and found that the inward radial flow strongly influences the strength and formation of the jet. Several effects, all originating from the converging radial inflow, work together to create the tubular jet. The results of high speed imaging, PIV measurements, and simulations lead us to the following sequence of events:

Directly after the pressure in the tube is released, liquid is funnelled into the pipe. If the meniscus is close enough to the bottom of the tube, the axial component of the flow pushes the perimeter of the interface upwards forming a rim.

This rim, propagating more like a hydraulic jump or bore instead of a surface wave, travels inward and is being pushed along by the inward radial flow directly under the interface. The singularity that occurs when the rim reaches the center manifests itself as a sharp jet shooting upwards.

During the formation and propagation of the rim, a mound of fluid forms on the surface of the rising water column. We have shown through PIV experiments that this mound is not merely the increase in amplitude that is seen in converging cylindrical waves. Fluid flows up into the mound from below, driven by the converging flow in the bulk of the column. This flow continues to feed the singularity caused by the rim for a short time. The authors of [1] dismissed the idea that the tubular jet is caused by flow convergence on the grounds that such an effect would not manifest itself after a delay. We have shown in experiments and irrotational potential flow simulations that the flow convergence affects the flow not after a delay, but from the very beginning of the process.

By experimentally obstructing and enhancing the radial flow component, we find that the mound and rim both depend on converging flow for their formation. The two mechanisms evolve separately, and then merge together to create the tubular jet.

Thus we have shown that the origin of the tubular jet lies entirely in the focussing of flow entering the tube. Therefore, the tubular jet is similar to jets that are produced by a geometrical flow focussing of the free surface of the liquid, as discussed in the introduction of this paper. There are important differences however: First it is not the initial shape of the free surface that produces the tubular jet, but the fact that the liquid has to enter the space confined by the tube walls. Secondly, the uniqueness of the tubular jet stems from the merging of two initially separate events: the creation, propagation, and collapse of the rim together with the continuous feeding of the jet by the enhanced vertical flow at the axis of the tube.

Appendix A Gravitational and capillary waves

In Fig. 7.5 the rim overtakes the smaller capillary waves as it travels to the center. In this Appendix we will check whether a gravitational wave of the size of the rim would indeed travel faster than the observed capillary waves. The surface waves are observed during the initial acceleration of the water column, therefore the waves are subject to an acceleration besides gravity. If we take z_0 to be of order R [1] and differentiate Eq. (7.2), we find an initial column acceleration of $\ddot{z}_{column} = (H/R)g$. If we introduce the total acceleration $g(1 + H/R)$ into the dispersion relation of a surface wave in the deep water approximation [23], we find

$$c(k) = \frac{\omega}{k} = \sqrt{\frac{g}{k}\left(1 + \frac{H}{R}\right) + \frac{\sigma k}{\rho}}\ , \tag{7.7}$$

with k being the wavenumber and ρ the density of the liquid. However, if the rim shape is a surface wave, it cannot be described by a simple monochromatic wave; it should be a superposition of many waves of varying wavenumber. Its propagation speed is thus given by the group velocity c_g, defined as the derivative of temporal frequency with respect to spatial frequency,

$$c_g(k) = \frac{d\omega}{dk} = c(k) + \frac{-g/k\left(1 + \frac{H}{R}\right) + \sigma k/\rho}{2c(k)}\ . \tag{7.8}$$

From Eq. (7.8) we find that the smaller, inner waves of $2\pi/k = 3$ mm will have a typical velocity of order 0.6 m/s, while a surface wave of the size of the rim (roughly $2\pi/k = 1$ cm or larger) would travel much slower, namely at a speed of 0.3 m/s for the depth of Fig. 7.5 ($H = 200$ mm). Since the rim shape is seen to 'overtake' the capillary waves in Fig. 7.5, it thus cannot be a gravitational surface wave and must be propelled by the liquid flowing in the tube.

Although Eq. (7.7) is commonly found in the context of two dimensional waves [23], the authors of [24] shows that the dispersion relation holds also for axisymmetric waves in the capillary regime.

Appendix B Boundary integral method

The axisymmetric form of Green's identity can be employed to write the Laplace equation $\nabla^2\varphi = 0$ for the flow potential $\varphi(r,z)$ in terms of a boundary integral [17], namely

$$\varphi = \frac{1}{2}\int_S \hat{r}\left(H\frac{\partial\varphi}{\partial\mathbf{n}} - \varphi\frac{\partial H}{\partial\mathbf{n}}\right) dS\,, \tag{7.9}$$

where $\mathbf{n}$ is the normal to the surface S, and

$$H = \frac{2}{\pi}\int_0^{\pi/2}\left((r+\hat{r})^2 + (z-\hat{z})^2 - 4r\hat{r}\cos^2\theta\right)^{-1/2} d\theta\,.$$

In this way, integrating over all points $(\hat{r},\hat{z})$ on the boundary S, the potential φ at any point (r,z) in the bulk can be obtained.

For the boundary conditions depicted by Fig. 7.13 (a), a constant radial inflow of strength V_0 is assumed to reach to depth L below the tube. At this depth L, the boundary conditions at the bottom are satisfied by taking it to be an image plane of the flow. The axis of symmetry has no contribution to the integral of Eq. 7.9. Using these boundary conditions, Eq. 7.9 can be written as

$$\varphi = -\frac{V_0 R}{\pi}\int_{-L}^{L}\int_0^{\pi/2} a^{-1/2} d\theta d\hat{z}\,, \tag{7.10}$$

with

$$a = (r+R)^2 + (z-\hat{z})^2 - 4rR\cos^2\theta\,.$$

Integrating Eq. 7.10 with respect to $\hat{z}$ and differentiating with respect to either r and z, yields the radial v_r and axial v_z flow velocities at point (r,z), namely

$$v_r = \frac{\partial\varphi}{\partial r} = -\frac{V_0}{\pi}\left[G(r,z) + G(r,-z)\right]\,, \tag{7.11}$$

with

$$G(r,z) = R\,\frac{z-L}{2r\sqrt{b}}\left[\frac{r-R}{r+R}\,\Pi\left(\frac{4rR}{(r+R)^2}, \sqrt{\frac{4rR}{b}}\right) + K\left(\sqrt{\frac{4rR}{b}}\right)\right]\,,$$

and

$$v_z = \frac{\partial\varphi}{\partial z} = \frac{V_0}{\pi}\left[F(r,z) - F(r,-z)\right]\,, \tag{7.12}$$

with

$$F(r,z) = \frac{R}{\sqrt{b}}\,K\left(\sqrt{\frac{4rR}{b}}\right)\,.$$

Here $\Pi(n,k) = \int_0^{\pi/2} \left((1-n\cos^2\theta)\sqrt{1-k^2\cos^2\theta}\right)^{-1} d\theta$ is the complete elliptic integral of the third kind, $K(k) = \int_0^{\pi/2} \left(\sqrt{1-k^2\cos^2\theta}\right)^{-1} d\theta$ is the complete elliptic integral of the first kind, and $b = (r+R)^2 + (z-L)^2$.

References

[1] E. Lorenceau, D. Quere, J.-Y. Ollitrault, and C. Clanet, *Gravitational oscillations of a liquid column in a pipe*, Phys. Fluids **14**, 1985 (2002).

[2] H.P. Le, *Progress and trends in ink-jet printing technology*, J. Imag. Sci. Tech **42**, 49 (1998).

[3] A.U. Chen and O.A. Basaran, *A new method for significantly reducing drop radius without reducing nozzle radius in drop-on-demand drop production*, Phys. Fluids **14**, L1 (2002).

[4] J. de Jong, G. de Bruin, H. Reinten, M. van den Berg, H. Wijshoff, M. Versluis, and D. Lohse, *Air entrapment in piezo-driven inkjet printheads*, J. Acoust. Soc. Am. **120**, 1257 (2006).

[5] G. Liger-Belair, H. Lemaresquier, B. Robillard, B. Duteurtre, and P. Jeandet, *The secrets of fizz in champagne wines: A phenomenological study*, Am. J. Enology and Viticulture **52**, 88 (2001).

[6] J.M. Boulton-Stone and J.R. Blake, *Gas bubbles bursting at a free surface*, J. Fluid Mech. **254**, 437 (1993).

[7] G. Birkhoff, D.P. MacDougall, E.M. Pugh, and G. Taylor, *Explosives with lined cavities*, J. Appl. Phys. **19**, 563 (1948).

[8] A.M. Worthington, *A study of splashes* (Longman and Green, London, 1908).

[9] B.W. Zeff, B. Kleber, J. Fineberg, and D.P. Lathrop, *Singularity dynamics in curvature collapse and jet eruption on a fluid surface*, Nature **403**, 401 (2000).

[10] R. Bergmann, D. van der Meer, M. Stijnman, M. Sandtke, A. Prosperetti, and D. Lohse, *Giant bubble pinch-off*, Phys. Rev. Lett. **96**, 154505 (2006).

[11] V. Ducleaux, F. Caillé, C. Duez, C. Ybert, L. Bocquet, and C. Clanet, *Dynamics of transient cavities*, submitted to Phys. Fluids (2006).

[12] S.T. Thoroddsen and A.Q. Shen, *Granular jets*, Phys. Fluids **13**, 4 (2001).

[13] D. Lohse, R. Bergmann, R. Mikkelsen, C. Zeilstra, D. van der Meer, M. Versluis, K. van der Weele, M. van der Hoef, and H. Kuipers, *Impact on soft sand: Void collapse and jet formation*, Phys. Rev. Lett. **93**, 1980031 (2004).

[14] J.R. Royer, E.I. Corwin, A. Flior, M.-L. Cordero, M.L. Rivers, P.J. Eng, and H.M. Jaeger, *Formation of granular jets observed by high-speed x-ray radiography*, Nat. Phys. **1**, 164 (2005).

[15] B.R. Munson, D.F. Young, and Okiishim T.H., *Fundamentals of Fluid Mechanics* (John Wiley & Sons, 1998).

[16] T. Bohr, P. Dimon, and V. Putkaradze, *Shallow-water approach to the circular hydraulic jumps*, J. Fluid Mech. **254**, 635 (1993).

[17] C. Pozrikidis, *Introduction to Theoretical and Computational Fluid Dynamics* (Oxford University Press, 1997).

[18] H.N. Oguz and A. Prosperetti, *Bubble entrainment by the impact of drops on liquid surfaces*, J. Fluid Mech. **219**, 143 (1990).

[19] H.N. Oguz and A. Prosperetti, *Dynamics of bubble growth and detachment from a needle*, J. Fluid Mech. **257**, 111 (1993).

[20] Yonggang Zhu, H.N. Oguz, and A. Prosperetti, *On the mechanism of air entrainment by liquid jets at a free surface*, J. Fluid Mech. **404**, 151 (2000).

[21] A. Prosperetti, *Drop surface interactions* (Springer, 2002), CISM courses and lectures Nr. 456.

[22] S. Middleman, *Modeling Axisymmetric Flows* (Academic Press, 1995).

[23] L. D. Landau and E. M. Lifshitz, *Fluid Mechanics* (Pergamon Press, Oxford, 1987).

[24] J.R. Saylor, A.J. Szeri, and G.P. Foulks, *Measurement of surfactant properties using a circular capillary wave field*, Exp. Fluids **29**, 509 (2000).

Chapter 8

Conclusions and outlook

We have explored the controlled impact of a solid body on sand and water and found them exemplary in the following ways:

- The impact of a solid body on water is a spectacular example of free surface flow. Although the event is dominated by gravity, its features express the full scope of hydrodynamics, as surface tension, viscosity, liquid inertia, and nearly all combinations of these account for the many different phenomena observed during the impact. Subsequently, next to the inertially driven collapse of the surface void a broad variety of the classical hydrodynamic instabilities can be observed during the impact, e.g., the Kelvin-Helmholtz instability due to the air flow in the narrowing neck or the Rayleigh-Plateau instability in the breaking up of the jet.

- The impact onto loose and fine sand is a prime example of the pluriform nature of granular matter which can exhibit behavior similar to the solid, liquid, and gas phase. On densely compacted sand the impacting object simply arrests close to the surface –as it would when impacting on a solid– but in loosely packed sand, the same spectacular impact phenomena that are observed for liquids are recovered. This transition can also be viewed in the context of terms common to granular matter, such as jamming, force chains, and hysteresis.

- There are surprisingly many similarities between the impact on water and on sand. The latter is therefore a rare example where a granular system can be described by a continuum model, i.e., a description in which the finite size of the grains plays no role.

- Finally, we found both water and sand impacts to be accessible using all of the three tools available to a physicist, namely experiments, theory, and numerical simulations: We performed high speed recording and high speed particle image velocimetry laboratory experiments, compared them to molecular dynamics and boundary integral simulations, and theoretically analyzed them using a two dimensional version of the Rayleigh equation.

The prime objective of this thesis was to study the dynamics of the free surface in liquids and sand after the impact of a solid body. With respect to this objective we can summarize our findings in the following qualitative way:

After the impact of a solid body on a free surface a splash and a void are created. Due to the hydrostatic pressure from the sides the void will start to collapse. Close to the surface the object passes early, but the pressure is low, therefore the collapse will be slow. Deeper, the body will pass later, but the hydrostatic pressure is higher. The competition between these two time intervals will cause the collapse to eventually occur near the middle of the void. As the walls of the void hit each other at the axis of symmetry, two jets are created. One shooting upwards and one shooting down into the enclosed bubble.

All conclusions drawn in this thesis contribute to a lesser or larger extent to the quantitative understanding of the series of events described above.

The first observation is the series of events after the impact of ball on fine and soft sand in the experiment and corresponding discrete particle simulations. We find that also in sand these events are precisely as stated above, including the emergence of a *granular jet* which driven straight into the air. There is a remarkable similarity to the events after the impact of a solid body on water (Chapter 2).

The second main observation is that due to the compressibility of the sand, the shape of the cavity is more or less cylindrical, while for a similar impact in water the cavity expands radially. This difference in cavity shape expresses itself in a different scaling for the closure depth and time with the Froude number, as we are able to understand in terms of our Rayleigh collapse model (Chapters 2 and 6).

The third finding is about the path of the object penetrating the sand. We measured the trajectory of a ball inside the sand and found its path to be captured extremely well by a simple Coulomb friction model, when released from the free surface (Chapter 3).

We found that the drag in the sand is greatly reduced by a lubricating effect of the airflow around the ball: As the pressure is reduced this effect becomes smaller and therefore the drag increases. For constant impact velocity this leads -at lower pressure- to altered trajectories with smaller penetration depths. From this we could explain the existence of two regimes: Lowering the pressure from atmospheric to several hundreds of millibars we first observe no effect on the jet height. This is because the drag increase mainly affects that part of the trajectory below the point at which the cavity closes. This changes into a second regime when the pressure is decreased below 400 millibar and the closure point starts to shift upwards, leading to a decrease of the jet height. We showed that the above phenomena are well captured by the Rayleigh-type hydrostatic collapse model described previously (Chapter 4).

The fourth main observation focuses on the pinch–off of the transient cavity in water, which we find to be *not* self-similar in a strict sense. For finite Froude number, we find the power–law scaling of the neck radius with time to have a non–universal exponent which depends on Froude. This Froude dependence is introduced due to the deviation of the cavity from a cylindrical shape and a second length-scale, the curvature of the void, comes into play. The radius of curvature is found to also exhibit power-law scaling in time, but with a different Froude dependent exponent. The difference in Froude dependence of the exponents signals the non-universality of the bubble pinch-off. Only in the limiting case of large Froude number, or extremely close to pinch–off, the cylindrical shape of the cavity is recovered and the neck radius follows the purely inertial scaling (Chapter 5).

Furthermore, as the fifth point we list the perfect agreement between boundary integral simulations and the impact of a disk in experiment. Not only the dynamics of the free surface is faithfully reproduced, but also the topology and magnitude of the flow surrounding the transient cavity is very accurately captured in a one to one comparison without any free parameters. Again, we find a simple model based on the Rayleigh equation to be sufficient to describe the key characteristics of the transient cavity (Chapter 6).

The sixth finding is that a jet can also be produced by flow focussing in a partly immersed pipe after a pressure release. Even though the jet produced after the impact on a free surface and the three dimensional equivalent of a jet produced by a bubble collapsing near a solid boundary are also induced by flow focussing. The tubular jet is unique, since in contrast to the two other cases, it has a twofold origin: the formation of a mound at the free surface and the collapse of a circular rim (Chapter 7).

There are many interesting aspects of impacts on liquid and on sand that remain to be investigated. Also a number of compelling modifications and alterations of the experimental setup are conceivable:

Surprisingly, although the surface seal mechanism discussed in Chapters 4 and 6 was already reported for liquids by Worthington as early as 1908 [1], a systematic study of its dependence on impact parameters and the ambient pressure is lacking. In Chapter 6 we shed some light on the onset of this phenomenon, but a full quantitative study remains to be done.

Another appealing extension of the water impacts presented in this thesis is to change the shape of the impactor. In a recent study [2] we submerged a cylinder and found an unexpected and lasting influence of capillary effects on the closure of the surface cavity. One could also think of breaking the axial symmetry of the object. We expect that this will lead to completely new cavity dynamics. E.g., if an ellipsoidal shape would impact on the water surface, the collapse would first occur along its minor axis, thereby leading to interacting transient cavities. This clearly is a new, very intriguing and interesting situation.

Recently there has also been increased interest in studying the dynamics of the bubble which is enclosed during the impact and which continues to follow the disk as it descents. Similar to our observation in Chapter 6 it is found to exhibit oscillations related to a Minneart frequency comparable to the frontal surface of the impactor [3]. This is an interesting observation in the context of under water noise production and asks for a more thorough investigation.

A number of recent papers [4–6] and Chapter 5 have provided considerable insight in the last stages of the purely inertial driven pinch–off. Although the theoretical analysis and simulations of [5] and [6] seem to indicate a universal approach towards the inertial pinch-off, this is not yet supported by experiments. Due to the long temporal range needed, very accurate experiments are called for, which may be feasible in a setup similar to the one presented in this thesis when the influence of air would be suppressed, e.g. by evacuating the setup. Furthermore, in a theoretical description of the pinch-off after the impact of a solid body, one should also account for the axial translation of the minimal neck radius discussed in Chapter 6. This feature is also observed in experiments of bubbles detaching from a needle [7], but is absent for the break–up of a sheared bubble presented in [5] and [6]. It would therefore be instructive to match the asymptotic description of the pinch–off proposed by [5, 6] to the global cavity dynamics put forward by Ducleaux *et al* [8] and the Chapters 2 and 6 of this thesis. In this way the axial translation of the minimal radius might be reproduced, as well as a full description of the collapsing cavity is obtained which captures all global and local characteristics of the collapsing void after an impact.

In this thesis we made recordings of the externally observable phenomena after the impact of a solid sphere on fine loose sand. Although this procedure yielded a good understanding of what is going on inside the sand (Chapters 2 and 4), in situ measurements of the closure depth in particular could improve this understanding. Therefore measurement methods of the cavity dynamics in the sand are called for. As an example of a feasible method one could think of a laser sheet shining into the collapsing void under an angle, thereby making it possible to determine the shape of the cavity from the reflection on the cavity wall.

Then there is the thick jet, reported first by Royer *et al.* [9], and observed in our own experiments for larger ball sizes. This, and liquid experiments in radially confined systems, leads us to hypothesize that this thick jet may be due to boundary effects. A more extensive study into these finite container size effects may well provide the definitive answer to this question.

In this thesis we successfully studied the jet creation by flow focussing. The observations on this mechanism will shed light on many of the jet phenomena created by the same mechanism introduced in Chapter 1. These findings will also contribute to the insight in the common nature of jetting.

References

[1] A.M. Worthington, *A study of splashes* (Longman and Green, London, 1908).

[2] S. Gekle, A. van der Bos, R. Bergmann, D. van der Meer, and D. Lohse, *Non-continuous froude number scaling for the closure depth of a cylindrical cavity*, submitted to Phys. Rev. Lett. (2006).

[3] T. Grumstrup and A. Belmonte, *private communication* .

[4] J.M. Gordillo, A. Sevilla, J. Rodriguez-Rodriguez, and C. Martinez-Bazan, *Axisymmetric bubble pinch-off at high Reynolds numbers*, Phys. Rev. Lett. **95**, 194501 (2005).

[5] J.M. Gordillo and M. Pérez-Saborid, *Dynamics of bubble-growth and detachment from a needle*, J. Fluid Mech. **562**, 303 (2006).

[6] J. Eggers, M.A. Fontelos, D. Leppinen, and J.H. Snoeijer, *Theory of the collapsing axisymmetric cavity*, submitted to Phys. Rev. Lett. (2006).

[7] N.C. Keim, P. Mller, W.W. Zhang, and S.R. Nagel, *Breakup of air bubbles in water: Memory and breakdown of cylindrical symmetry*, Phys. Rev. Lett **97**, 144503 (2006).

[8] V. Ducleaux, F. Caillé, C. Duez, C. Ybert, L. Bocquet, and C. Clanet, *Dynamics of transient cavities*, submitted to Phys. Fluids (2006).

[9] J.R. Royer, E.I. Corwin, A. Flior, M.-L. Cordero, M.L. Rivers, P.J. Eng, and H.M. Jaeger, *Formation of granular jets observed by high-speed x-ray radiography*, Nat. Phys. **1**, 164 (2005).

Summary

In this thesis we investigate the impact of a body on sand and water. When a body impacts a free surface in the inertial regime the series of events is the following: On impact material is blown away in all directions and an impact cavity forms. Due to the hydrostatic pressure from the sides the cavity will start to collapse. Close to the surface the body passes early, but the pressure is low, therefore the collapse will be slow. Deeper, the body will pass later, but the hydrostatic pressure is higher. The competition between these two time intervals will cause the collapse to eventually occur near the middle of the void. As the walls of the void hit each other at the axis of symmetry, two jets are created: One is driven straight into the air and a second jet shoots down into the enclosed bubble (Chapter 1).

Surprisingly, this series of events does not only unfold for an impact on water, but a similar void collapse can also be observed in aerated sand, when a steel ball impacts a very loose and fine bed of sand. In Chapter 2 we find that in experiments and discrete particle simulations a jet of sand shoots up- and downward after the “hydrostatic” void collapse. In addition to the experiments and the discrete particle simulations we present a Rayleigh type continuum theory to account for the void collapse.

Due to the compressibility of the sand, the shape of the cavity is more or less cylindrical, while for a similar impact in water the cavity expands radially. This difference in cavity shape expresses itself in a different scaling for the closure depth and time with the Froude number, as we are able to understand in terms of our Rayleigh collapse model in Chapter 2 for sand and Chapter 6 for water.

Normally, sand can support a weight through internal force chains, a highly inhomogeneous force network between the grains. However, by allowing air to flow through the fine sand prior to the experiment this force-chain structure can be weakened considerably. When the air is turned off and the bed has settled (Chapter 3) we find that the sand can no longer

support weight. Depending on its mass a ball released from the surface sinks into the sand up to a depth of about five diameters. The final depth the ball reaches is found to scale linearly with its mass and its trajectory is found to be captured extremely well by a simple Coulomb friction model.

In Chapter 4 we find that the drag in the sand is greatly reduced by a lubricating effect of the airflow around the ball: As the pressure is reduced this effect becomes smaller and therefore the drag increases. At lower pressure this leads -for constant impact velocity- to altered trajectories with smaller penetration depths. From this we can explain the existence of two regimes: Lowering the pressure from atmospheric to several hundreds of millibar we first observe no effect on the jet height. This is due to the drag increase mainly affecting the trajectory below the point at which the cavity closes. This changes into a second regime when the pressure is decreased below 400 millibar and the closure point starts to shift upwards, leading to a decrease of the jet height. Also these above phenomena are well captured by the Rayleigh-type hydrostatic collapse model described previously.

As for an impact in sand, during the impact onto a water surface one has to deal not only with the body acting on the water, but also with the fluid acting on this body. To circumvent this coupling, an experimental setup is presented in which we have *full control* over the motion of the impacting object by attaching it to an external motor. In this way, the response velocity of the impacting body inside the liquid is effectively eliminated, as it now becomes a control parameter of the system (Chapter 1).

In Chapter 5 this experimental setup is used together with boundary integral simulations to study the pinch–off of the transient cavity in water, which we find to be *not* self-similar in a strict sense. For finite Froude number, we find the power–law scaling of the neck radius with time to have a non–universal exponent which depends on Froude. This Froude dependence is introduced due to the deviation of the cavity from a cylindrical shape and a second length-scale, the curvature of the void, comes into play. The radius of curvature is found to also exhibit power-law scaling in time, but with a different Froude-dependent exponent. Only in the limiting case of large Froude number, or extremely close to pinch–off, the cylindrical shape of the cavity is recovered and the neck radius follows the purely inertial scaling.

The perfect agreement between the boundary integral simulations and the controlled impact of a disk in experiment holds not only for the full dynamics of the free surface, but also the topology and magnitude of the flow surrounding the transient cavity is faithfully reproduced in a one to one comparison without any free parameters. And, we find the simple model based on the Rayleigh equation to be sufficient to describe the key characteristics of the transient cavity (Chapter 6).

Finally, in Chapter 7 we investigate a jet produced by flow focussing in a partly immersed pipe after a pressure release. The "tubular jet" is induced by flow focussing like the jet produced after the impact on a free surface and, the three dimensional equivalent, of a jet produced by a bubble collapsing near a solid boundary. The tubular jet is nevertheless unique, since in contrast to the two other cases, it has a twofold origin: the formation of a mound at the free surface and the collapse of a circular rim.

Samenvating

In dit proefschrift onderzoeken wij de inslag van een object op zand en water. Wanneer een object inslaat op een vloeistof oppervlak dan gebeurt er het volgende: Op het moment van de inslag spat materiaal alle richtingen uit en vormt zich een holte aan het oppervlak. Deze holte stort vervolgens ineen door de hydrostatische druk die op de wanden werkt. Het object zal een diepte vlak onder het oppervlak al snel bereiken, maar aangezien de hydrostatische druk hier laag is voltrekt de sluiting zich hier relatief langzaam. Voor grotere dieptes is het net andersom: het object heeft veel tijd nodig om deze diepte te bereiken, maar de holte zal hier relatief snel sluiten. De competitie hiertussen zorgt ervoor dat de sluiting zich uiteindelijk nabij het midden van de holte voltrekt. Zodra de wanden van de holte elkaar op de symmetrie-as raken ontstaan er twee stralen van materiaal: Een straal schiet omhoog de lucht in, terwijl de tweede omlaag de ingesloten bel inschiet (Hoofdstuk 1).

Verrassend genoeg voltrekken deze gebeurtenissen zich niet alleen bij een inslag op water; ook wanneer we een stalen kogel op gefluidiseerd zand laat vallen zien we dezelfde verschijnselen. In Hoofdstuk 2 vinden we zowel in experimenten als in “molecular dynamics” simulaties een straal van zand die omhoog en omlaag schiet na de sluiting van de holte onder invloed van de “hydrostatische” druk in het zand. Naast experimenten en simulaties presenteren we een continuüm theorie gebaseerd op de Rayleigh vergelijking als beschrijving voor de sluiting van deze holte.
Dankzij de samendrukbaarheid van zand is de vorm van de holte in het zand cilindrisch, terwijl tijdens eenzelfde inslag in water de holte ook in radiele richting uitzet, zodat een zich naar boven toe verbredende holte ontstaat. Dit verschil in vorm beïnvloedt de wijze waarop de sluitingsdiepte en sluitingstijd in water en zand afhangen van het Froude getal. Het verschil in de schaling tussen beide kan verklaard worden met de Rayleigh theorie (Hoofdstuk 2 voor zand en Hoofdstuk 6 voor water).

Normaliter kan zand gewicht dragen door een interne structuur van “force chains”, een hoogst inhomogeen netwerk van krachten tussen de zandkorrels. Echter, wanneer fijn zand voorafgaand aan een meting gefluidiseerd wordt en daarna weer tot rust komt, dan zijn deze force chains sterk verzwakt. In Hoofdstuk 3 vinden we dat de zo behandelde zandlaag dan niet langer in staat is om enig gewicht te dragen. Een kogel die wordt losgelaten aan het oppervlak dringt tot wel vijf keer zijn diameter in het zand door. De uiteindelijke diepte die de kogel bereikt is recht evenredig met zijn massa en de baan van de kogel wordt bijzonder goed beschreven door een op Coulomb wrijving gebaseerd model.

In Hoofdstuk 4 vinden we dat de wrijving die de kogel in het zand ondervindt sterk verkleind wordt door de invloed van de luchtstroom rond de kogel. Bij lagere luchtdrukken leidt dit -voor een constante inslag snelheid- tot een verandering van de baan van de kogel en daardoor tot een kleinere doordring diepte. Hierdoor ontstaan twee regimes: Als we de luchtdruk verlagen van atmosferisch naar enkele honderden millibar zien we geen effect in de uiteindelijke hoogte van de zandstraal. Dit komt doordat de toegenomen wrijving de baan van de kogel voornamelijk beïnvloed nadat de kogel de diepte van de sluiting gepasseerd is. Dit verandert in het tweede regime (beneden de 400 millibar) waar de sluitingdiepte omhoog verschuift, hetgeen leidt tot een afname van de hoogte van de zandstraal. Ook dit verschijnsel wordt beschreven door het Rayleigh model gebaseerd op een hydrostatische sluiting.

Net als bij een inslag in zand, moet men gedurende een inslag in water niet alleen rekening houden met de invloed van het object op het water, maar ook met het effect dat de vloeistof op het object heeft. Om deze koppeling te voorkomen hebben wij een experimentele opstelling ontwikkeld waarmee we door het gebruik van een externe lineaire motor *volledige controle* over de beweging van het object verkrijgen. Op deze manier is de snelheid van het object niet langer een respons van het systeem, maar een controle parameter (Hoofdstuk 1).

In Hoofdstuk 5 gebruiken we deze opstelling samen met zogenaamde “boundary integral” simulaties om het allerlaatste stadium voor de sluiting van de holte te bestuderen, ook wel insnoering gemoemd. In andere systemen, zoals de insnoering die plaats vindt vlak voordat een druppel van een waterkraan valt, blijkt de vorm van de insnoering vaak onafhankelijk te zijn van de schaal waarop men het verschijnsel bekijkt. Wij hebben ontdekt dat deze eigenschap, die bekend staat als ‘self-similarity’, niet voor ons systeem opgaat. Dit uit zich in het feit dat de exponent van de “power-law” schaling van de straal van de insoering met de tijd niet universeel is: deze exponent hangt van het Froude getal af. Dit komt doordat de holte niet puur cilindrische van vorm is, waardoor een tweede lengte schaal, de kromming van de holte, belangrijk wordt. Ook deze kromming vertoont “power-law” schaling met de tijd, echter met een andere exponent, die eveneens van het Froude getal afhankelijk is. Slechts voor zeer grote inslagsnelheden, of extreem dicht bij de pinch-off, is de holte lokaal cilindrisch en schaalt de straal van de insnoering zoals door de Rayleigh vergelijking voorspeld is.

De perfecte overeenkomst tussen de “boundary integral” simulaties en experimenten met de gecontroleerde impact van een schijf geldt niet alleen voor de vorm van de holte. Een directe vergelijking van de stroming rondom de holte, zonder gebruik te maken van vrije parameters, geeft een identiek beeld: zowel de topologie als de grootte van de stroming is in beide gevallen volledig gelijk. Alle belangrijke aspecten van de vorm van de zich sluitende holte worden daarnaast perfect gereproduceerd door het analytische Rayleigh model (Hoofdstuk 6).

Tenslotte bekijken we in Hoofdstuk 7 de oorsprong van de waterstraaljet die ontstaat na het openen van een deels in water ondergedompelde pijp. Deze “tubular jet” wordt net als bij de inslag van een object geproduceerd door een mechanisme waarbij de stroming in de vloeistof alle energie focust op de symmetrie as van het systeem. Toch is de tubular jet uniek, aangezien in tegenstelling tot het vorige geval de tubular jet een tweevoudige oorsprong heeft: Ten eerste ontstaat er een cirkelvormige golf op het opervlak die vervolgens sluit. Dit zou slechts een kleine jet opleveren, ware het niet dat de radiele instroom van de vloeistof, de jet blijft voeden. Het samenspel tussen deze verschijnselen creëert de waargenomen krachtige tubular jet.

Acknowledgements

The research described in this thesis is part of the research program of the "Stichting voor Fundamenteel Onderzoek der Materie" (FOM), which is financially supported by the "Nederlandse Organisatie voor Wetenschappelijk Onderzoek" (NWO). It was carried out at the Physics of Fluids research group of the faculty of Science and Technology of the University of Twente. I gratefully acknowledge the support of these institutions.

While writing these acknowledgements, I reflect over the past four years. In doing so, I realize that this thesis is not the accomplishment of one person but rather the effort of a large group of people. Each of them contributed a larger or smaller part, but all of them were instrumental to the work presented here. In this acknowledgement I will try to express my appreciation to all the people involved for sharing with me the ups *and* downs which led to the creation of this thesis.

First I would like to express my gratitude to my promotor Prof. Detlef Lohse and assistant promotor Dr. Devaraj van der Meer. For Devaraj and Detlef I have the deepest respect as physicists and men. They taught me many if not all aspects of performing research. They taught me to be critical and honest, how to convey my ideas on paper and in speech, but above all, they taught me to have fun doing it. They instilled in me a taste of problems and an attitude on how to approach them, which I hope I can continue to uphold. Working with both was an extremely enriching experience on a scientific level, but maybe even more on a personal level, and I thoroughly enjoyed it. I hope that our paths will continue to cross in the future, in personal and professional atmospheres.

During the years of my PhD I also worked closely with the following students who performed their Master thesis or internship on one of the topics of this thesis. In chronological order these students are Jean-Baptiste Choimet, Remco Rauhé, Erik de Jong, Ruben Snijdewind, and Arjan van der Bos (now a fellow PhD student). These collaborations were not only very fruitful, as they make up a large part of this thesis and led to beautiful publications, but above all they were most enjoyable. I look back fondly on our shared scientific victories (and mishaps) and wish all of you the very best in the future. I would also like to thank Johanna Bos and Roderick Knuiman for their experimental input on the tubular jet.

Finishing a PhD consists not only of four years of work, but also of a considerable number of lunch breaks. Therefore I would sincerely like to thank Peter Eshuis, Jos de Jong, and Christian Veldhuis for the time spent during these breaks discussing a great variety of subjects, ranging from the topics of this thesis to the latest offers at Intratuin. Besides the breaks you guys were always available to help with advice or action in many fields and for this I am very grateful.

I would also like to mention my other roommates Gabriel Caballero and Stefan Gekle. Not only did I enjoy having you as roommates, but in a relatively short time we managed to collaborate and obtain some great scientific results.

The realization of the experimental setups presented in this thesis would not have been possible without the untiring enthusiasm, creativity, and technical skills of Gert-Wim Bruggert, Martin Bos, Bas Benschop and the late Henni Scholten. I especially remember the long days of tweaking the linear motor together with Henny and Gert-Wim. I would also like to express my gratitude to Joanita Lenferink for her support and patience. At the same time I would like to extend my apologies to her as I was often the very last to turn in any required form and/or administrative assignment.

I would also like to acknowledge all my (former) scientific colleagues at the Physics of Fluids group. A great team consisting of: Professors Leen van Wijngaarden and Andrea Prosperetti, staff-members Gerrit de Bruin, Sascha Hilgenfeldt, Claus Dieter Ohl, and Michel Versluis, all of which have always been available for a wise word or a refreshing point of view. I would also like to thank all the (former) post-docs Stefan Luther, Adrian Staicu, Nicolas Bremond, Enrico Calzavarini, Benjamin Dollet, Aurore Naso, Paolo Oresta, Christophe Pirat, Mauro Sbragaglia, and Kazuyasu Sugiyama.
And last but not least, I would like to mention all my (former) fellow PhD students, Rüdiger Tögel, Anna von der Heydt, Judith Rensen, Mark Stijnman, Manish Arora, Ramon van de Berg, Hanneke Bluemink, Bram Borkent, Edip Can, Rory Dijkink, Francisco Fontenele Araujo Jr., Henk

Jan van Gerner, Wim van Hoeve, Roger Jeurissen, Sander van der Meer, Marlies Overvelde, Jeroen Sijl, ShangJiong Yang, with all of whom it was a pleasure to work.
Out of this group I especially would like to mention Prof. Andrea Prosperetti and Drs. Mark Stijnman, since they are responsible for the creation of the wonderfull boundary integral code which is used on several occasions in this thesis.

I also want to thank Christiaan Zeilstra, Martin van der Hoef, both in the Fundamentals of Chemical Reaction Engineering group headed by Prof. Hans Kuipers. Their great numerical work on the granular jet has been included in this thesis.

Special thanks goes to my family, Jeroen Bergmann, Rita Hendricusdottir, my parents Raymond Bergmann sr. and Franka Bergmann-Schoonen for all their unwavering support and understanding during all those years of education and the final four years as a PhD student. I would like to thank my parents for all the opportunities they have given me and state that for this reason this thesis is as much their effort as it is mine.

Finally, I thank Kirsten Philipsen for her love, patience, and the layout of my appendices.

About the Author

Raymond Bergmann was born on January 15, 1979, in Amsterdam, the Netherlands. He attended high-school “de Godelinde” in Naarden-Bussum, from which he graduated with honors in 1997 and being awarded “the best physics student” award from the Dutch Physics Society. He then went on to study Applied Physics at the Technical University of Twente, during which he spent half a year as a research scientist at the Department of Engineering and Applied Sciences at Harvard University in the USA working with Prof. Michael Brenner. In 2003 he obtained his Masters degree with honors in Applied Physics working with Dr. Stefan Luther and Prof. Detlef Lohse on bubble interactions in an acoustic field. He then remained at the Physics of Fluids group headed by prof. Detlef Lohse to work on his PhD thesis with Dr. Devaraj van der Meer and Prof. Detlef Lohse.